Biomaterial Platforms to Study Cancer Dormancy and Develop Therapeutic Strategies for Breast and Ovarian Cancers

A DISSERTATION
SUBMITTED TO THE FACULTY OF THE
UNIVERSITY OF MINNESOTA
BY

Hak Rae Lee

IN PARTIAL FULFILLMENT OF THE REQUIREMENTS
FOR THE DEGREE OF
DOCTOR OF PHILOSOPHY

Advisor
Samira M. Azarin

March 2020

Acknowledgement

First and foremost, I wish to express my sincere gratitude to my advisor, Professor Samira Azarin for her tremendous support from the first day I joined her group. She has been a major contributor to my dissertation and my research ideas would have never come out as great publications without her insight, advice, and patience. She has provided me an unrestrained research environment where my research ideas expand freely and as I have failed and learned from my mistakes under her guidance and mentorship I have become a structured thinker.

Life in my graduate school would have not been sunny without my lab mates. I want to thank all members of the Azarin group: Jen, Hannah, Jenny, Pedram, Tiffany, Harish, Kristen, Paulina, Joe, Victoria, Pranati, Janani. Special thanks to Tiffany, Kristen, and Jenny for taking the time to help me refine and improve this dissertation. I would also like to thank Frankie, Azarin group alumnus, for teaching me many experiments which made my work possible.

I also thank my close friends in CEMS. Thank you, Blake, for being a friend and roommate since my very first day in the US. I have been not alone in Minnesota since we have been through a lot together. Thank you, Pavlos for invigorating me when I got stuck. Thanks, GK, for helping me go through difficulties as an international student. I would also like to thank Korean fellows - Dr. Dae Woo Kim, Dr. Hanim Kim, Dr. Kiwon Eum, Dr. WooSeok Jeong, Dr. Bongjoon Lee, Dr. Mihee Kim, Dr. Kyungtae Kim, Hwanhui Yun for being a ‘home away from home’ and mentoring me as more experienced senior researchers.

Most of all, I wish to express my deepest gratitude to my family for their unconditional love and unwavering support. My parents, Soonok Kim and Ilkyu Lee, my brother, Hak Joo Lee, and my parents-in-law, Se Mee Jang and Oh Young Kwon have sacrificed much in enduring lengthy separations so that I could enjoy the privilege of a good education in the US. I also take this opportunity to thank my two grandfathers who passed away during my Ph.D. I will strive for success in my life to repay such a profound debt. Most importantly, all my work must be dedicated to my lovely wife, Yeon Hye Kwon, who has stood by me through my voyage all the way from Korea to US. Thank you for giving me support, confidence, and hope in every single decision I have made.

Finally, my thanks and appreciations also go to my colleague and people who have willingly helped me in my work here at the University of Minnesota.

Abstract

In breast and ovarian cancer, the primary source of mortality is metastasis. Even in patients who are thought to be cancer-free after initial treatment, metastatic recurrence after months or years of asymptomatic latency period in patients is common in both cancers. Cancer cells that stay dormant and evade chemotherapy have been thought to underpin the metastatic recurrence, but the underlying mechanisms are unclear thus far. Despite advances in cancer treatment, recurrent metastatic cancer is rarely curable. Thus, preventing metastatic recurrence by preemptively eliminating dormant cancer cells is a key to reduce the mortality in breast and ovarian cancers. To effectively target and destroy dormant cancer cells evading chemotherapy, well-established experimental platforms for a better understanding of their unique biological characteristics as well as development of novel therapeutic strategies are required.

The work presented in this dissertation aims to provide facile *in vitro* and *in vivo* experimental platforms that enable the investigation of cancer dormancy in breast and ovarian cancers as well as to develop a novel therapeutic alternative to chemotherapy to destroy ovarian cancer cells, as current therapeutic options for ovarian cancer are much more limited than for breast cancer. In the first study, an *in vitro* platform that stably induced dormant state in breast and ovarian cancer cells was developed using cobalt chloride ($CoCl_2$), a hypoxia mimetic agent. Hypoxia has been identified as a microenvironmental niche that harbors dormant cancer cells in many types of cancer, but its role in cancer dormancy has been poorly understood due to the lack of models that stably induce and maintain hypoxia and dormancy. $CoCl_2$ created a robust hypoxia-mimicking microenvironment where breast and ovarian cancer cells could remain in a dormant state for molecular characterization. This platform enables investigation of poorly-understood molecular mechanisms underlying cancer dormancy under hypoxia in both cancers. To investigate hypoxic regulation of cancer dormancy in a more physiologically relevant context, an *in vivo* platform combining $CoCl_2$ with biomaterial scaffolds composed of poly(lactide-co-glycolide; PLG) was also developed. The PLG scaffolds that release $CoCl_2$ established an *in vivo* hypoxic niche that can recruit disseminating cancer cells,

enabling investigation of how a hypoxic niche harbors dormant cancer cells at metastatic sites. Though the *in vivo* platform was tested with a previously established breast cancer metastasis model, this platform could be also used to study ovarian cancer dormancy within a hypoxic niche in the body.

Lastly, we present a novel biomaterial-based therapeutic strategy to destroy metastatic ovarian cancer cells via sonodynamic therapy. Conventional chemotherapy, which mainly targets rapidly proliferating cancer cells, has been ineffective for non- or slow-proliferating dormant cancer cells. To address this issue, an alternative therapeutic strategy was developed using graphene nanoribbons (GNR) functionalized with a sonosensitizer, chlorin e6 (Ce6). This biomaterial-based approach effectively destroyed ovarian cancer cells through sonodynamic ablation and could be used to reduce the metastatic recurrence resulting from the cancer cells evading chemotherapy. Altogether, the experimental platforms and therapeutic strategy established in this dissertation may provide us a better understanding of dormancy in breast and ovarian cancers as well as a new treatment option that can prevent metastatic recurrence.

Table of Contents

List of Tables

List of Figures

Chapter 1 – Introduction

1.1. Metastatic recurrence in breast and ovarian cancer

Each year, more than 40,000 women die from breast cancer and about 14,000 women die from ovarian cancer in the US. Notably, more than 90% of cancer-related deaths in breast and ovarian cancer are due to metastases that impair the function of vital organs [1–3]. In breast cancer, the 5-year survival rate for patients with metastasis is only 27% while that for patients without metastasis is 99% (Fig. 1-1), meaning that metastasis has a substantial influence on the length of survival. Though only 6% of new breast cancer cases have overt metastasis at the time of diagnosis, it has been estimated that 20-45% of all breast cancer patients will ultimately develop metastatic disease [4]. This pattern highlights that many patients with early-stage breast cancer have undetectable micrometastases present at the time of diagnosis, putting them at risk for later development of metastatic disease.

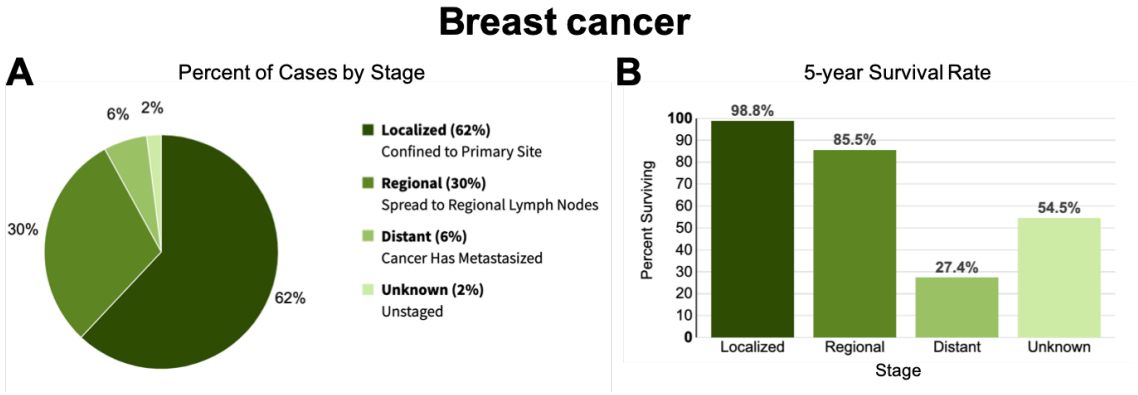

Figure 1-1. Metastasis has a substantial influence on patient survival in breast cancer. (A) Percentage of patients in each cancer stage at the time of diagnosis. (B) 5-year relative survival rate by stage at diagnosis for females with breast cancer in the US [5].

In contrast to breast cancer, about 60% of ovarian cancer patients already have widespread metastasis at the time of diagnosis, with a 5-year survival rate of 29% compared with 92% for patients without metastasis (Fig. 1-2). For most ovarian cancer patients with widespread metastasis, debulking surgery to remove as many of the metastatic nodules as possible followed by adjuvant chemotherapy using platinum/taxane-based drugs has been the standard treatment [6]. Despite positive initial responses to chemotherapy in more than 75% of patients, metastatic relapse occurring after the completion of initial treatment is very common in ovarian cancer, as the residual tumors frequently evade or develop resistance to chemotherapy, causing treatment failure and death in over 90% of patients [7]. Approximately 70% of all ovarian cancer patients will have tumor recurrence, and this number rises to 90-95% for patients diagnosed in advanced stages (stage III or stage IV) [8].

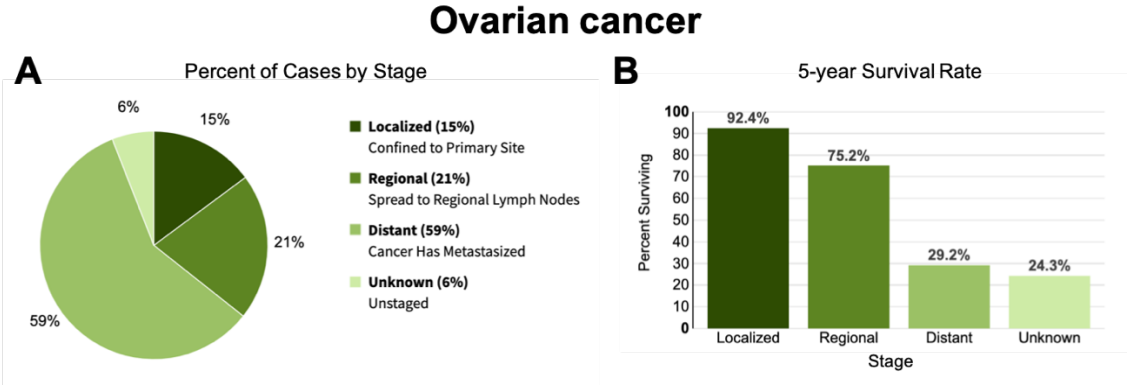

Figure 1-2. Metastasis has a substantial influence on patient survival in ovarian cancer. (A) Percentage of patients in each cancer stage at the time of diagnosis. (B) 5-year relative survival rate by stage at diagnosis for ovarian cancer in the US [9].

Over the past few decades, researchers have demonstrated the presence of residual tumor cells disseminated from the primary tumor within patients after the completion of initial therapy [4]. Some disseminated tumor cells (DTCs) were found to enter a dormant

state, during which DTCs do not proliferate or divide, thereby evading chemotherapy, which mainly targets rapidly proliferating cancer cells. The dormancy period can range from a few months to as long as decades, depending on the subtype of cancer, molecular characteristics, receptor expression, systemic inflammation, and many other factors [10]. Upon being stimulated by specific microenvironmental factors, these dormant cells can become reawakened and activated, eventually forming secondary metastases often with increased chemoresistance, leading to poor patient survival. Hence, preemptively targeting dormant DTCs by understanding the molecular mechanisms of cancer dormancy and developing novel therapeutic strategies that do not rely on targeting actively dividing cells offers a potential window of opportunity for the prevention of metastatic recurrence in breast and ovarian cancer patients.

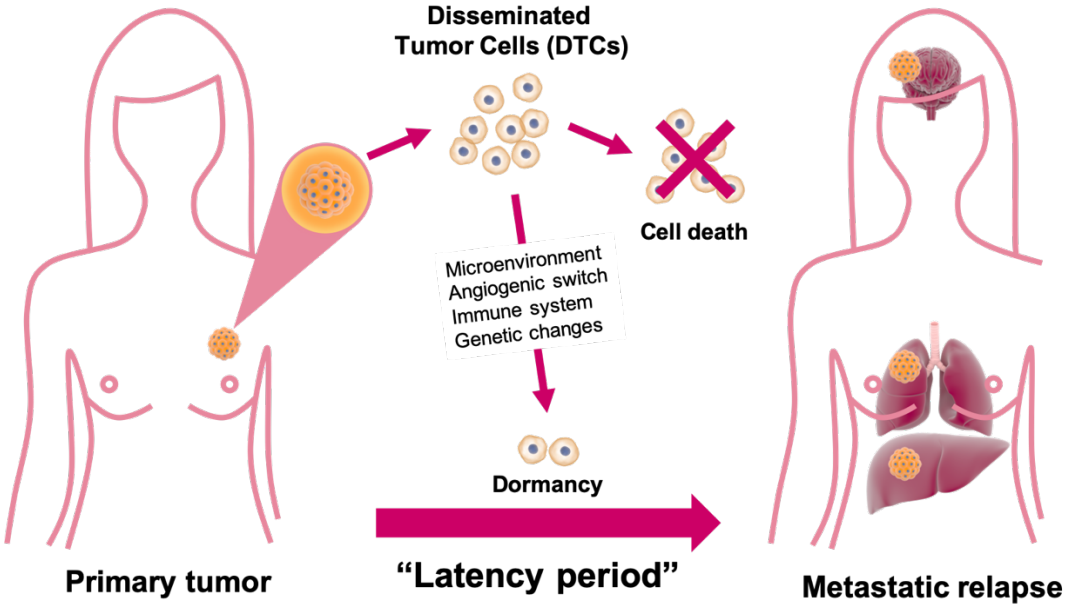

Figure 1-3. Possible fates of DTCs from primary tumor in breast cancer. Dormant DTCs give rise to the latency period before metastatic relapse in many breast cancer patients. Factors that lead to dormancy include microenvironmental cues, the balance of pro- and anti-angiogenic signals, immune response, and genetic changes [11].

1.2. Dormancy precedes metastatic recurrence in breast cancer.

In breast cancer patients, the presence of DTCs in bone marrow is a common phenomenon observed in more than 40% of patients at diagnosis [11]. Most of DTCs are already dead or eliminated by the shear stresses in blood stream during the dissemination, but a small fraction of DTCs may survive (Fig. 1-3) [11]. Compared with other types of cancer, breast cancer has been known to have particularly long periods of dormancy, which can be up to 25 years without any symptoms of disease, followed by a metastatic recurrence [11]. Approximately 60-70% of deaths from breast cancer occur beyond the 5-year survival window due to late metastatic recurrence after years or decades of disease-free latency [12]. Thus, understanding this stage of tumor progression is key to establish better therapeutic plans to prevent tumor recurrence in breast cancer patients. If a patient's risk of recurrence can be predicted based on a better understanding of dormancy-associated biology, alternative targetred therapies could be explored to avoid overtreatment with chemotherapy that will be ineffective at killing the residual DTCs. However, this opportunity has not been realized because our understanding of the underlying mechanisms of cancer dormancy is limited due to the lack of well-established experimental models.

1.2.1. Microenvironmental regulation of DTC dormancy

Accumulating evidence has proposed that the residual DTCs can remain dormant either by entering a quiescent state, a reversible growth arrest in the G0/G1 phase of the cell cycle (cellular dormancy), or existing as micrometastases where the proliferation of the tumor mass is counterbalanced by cell death from the anti-tumoral activity of the immune system or the lack of vascularization to support tumor growth [4,11,13,14]. While

these two types of dormancy are not mutually exclusive and might even coexist in the entire population of DTCs of the same patient [11,15], this dissertation will focus on cellular dormancy.

Previous studies using various tumor model systems highlight the important role of microenvironmental factors in regulating cellular dormancy. A recent study by Ghajar et al. found that the perivascular niche strongly impacts DTC dormancy [16]. This work identified that the resting endothelium produces thrombospondin-1 (TSP-1), which induces dormancy in DTCs. In contrast, endothelial tip cells in sprouting neovasculature promote proliferation of DTCs by secreting transforming growth factor beta 1 (TGFβ1) and periostin (POSTN). In addition to the perivascular niche, Lawson et al. found that the endosteal niche induces dormancy in bone marrow [17]. They found that dormant myeloma DTCs in bone marrow were engaging with osteoblasts in the endosteum, whereas proliferating DTCs were not. Remarkably, proliferating cells introduced to an experimental endosteal niche were able to enter a dormant state. In addition, dormant DTCs released from the endosteal niche could be reactivated through enhanced osteoclast activity induced by soluble receptor activator of nuclear factor kappa-B ligand (sRANKL), suggesting that dormancy is a reversible state regulated by the microenvironment. Furthermore, Shiozawa et al. showed that osteoblast-derived growth arrest-specific 6 (GAS6) protein signaling through its receptor Axl induces dormancy in prostate cancer DTCs [18,19]. Interestingly, under hypoxic conditions a negative feedback loop of GAS6/Axl is inhibited, leading to increased Axl expression and possibly maintenance of dormancy in hypoxic microenvironments [20].

1.2.2. Hypoxic regulation of cancer dormancy

As stated above, DTCs are frequently found in the bone marrow of cancer patients, even in patients with no evidence of metastases. The bone marrow microenvironment therefore seems to be inhibitory for cell growth and thus causes most DTCs enter dormancy. Bone marrow is a hypoxic tissue where the oxygen level is relatively low compared to other organs [13,14,21,22]. Recent evidence from experimental and clinical studies increasingly points to a fundamental role for hypoxia in cancer dormancy observed in the bone marrow. Johnson et al. suggested that tumor cells may enter dormant state through interactions with the hypoxic bone microenvironment. They found breast cancer cells stay dormant within hypoxic regions of bone marrow [22]. Recently, proteomic analysis of DTCs in bone marrow obtained from patients with breast cancer showed that these DTCs activate markers of the unfolded protein response (UPR) or the endoplasmic reticulum (ER) stress response as a cellular adaptation strategy to survive the hypoxic microenvironment in the bone marrow [28]. These findings suggest that the hypoxic microenvironment in secondary metastatic sites such as bone marrow may prime the DTCs to enter a dormant state.

Hypoxia is also a prominent feature of the microenvironment of primary tumors [23,24]. In primary breast tumors, hypoxia was found to give rise to the heterogeneity of DTCs and spawn dormant tumor cells [25]. One of the early cellular responses to hypoxia is to decrease the proliferation rate in order to reduce oxygen consumption, hence hypoxic cells divide far more slowly and to remain viable over a prolonged period [26]. Li et al. observed that while tumor cells in the non-hypoxic periphery of primary tumors were proliferating, tumor cells in the hypoxic core of these tumors were not, suggesting that dormant tumors may be hypoxic and hypoxia may be related to low proliferation rates and

thus tumor dormancy [27]. Previous studies have also shown that cells exposed to hypoxia have a disproportionately long G1 phase or arrest in the G0/G1 phase of cell cycle, which is a key feature of dormancy [26]. It was also experimentally demonstrated that a vast majority of hypoxic tumor cells are negative for proliferation markers (e.g. Ki67, PCNA, BrdU) [11,26]. Taken together, these findings highlight that dormant DTCs may also result from cells that entered dormancy in hypoxic environments within the primary tumor.

1.3. *In vitro* and *in vivo* models to study hypoxic regulation of cancer dormancy

1.3.1. *In vivo* models

One of the challenges in studying dormancy is that it is undetectable using conventional whole-body imaging tools due to the low frequency of dormant tumor cells. In addition, cancer dormancy is a difficult stage of tumor progression to track as it takes place over long periods. Thus, most research on cancer dormancy relies on rapidly growing cancer cell lines and aggressively growing metastasis/transgenic oncogene models. For instance, by using patient-derived xenografts and the transgenic MMTV polyoma middle T mouse model, Fluegen et al. found that naturally-occurring hypoxia in the primary tumor upregulates key dormancy markers including NR2F1, DEC2, and p27 in MDA-MB-231 breast cancer cells [29]. Johnson et al. found that the leukemia inhibitory factor receptor (LIFR) signaling pathway confers a dormant phenotype in breast cancer cells disseminated to bone [22]. They also identified that hypoxia in the bone marrow reduces LIFR signaling in breast cancer cells and promotes proliferation with downregulation of dormancy-associated genes. However, *in vivo* mouse models provide limited control of the organ

environment for controlled investigations. Moreover, high costs, heterogeneity, and the challenges of locating and imaging dormant cells in internal tissues make the use of *in vivo* models challenging [30]. Thus, *in vitro* models have gained attention since they can recapitulate hypoxia in a simple and relatively reproducible way, as well as enable the facile control of environmental factors and measurement of cellular responses.

1.3.2. *In vitro* models using hypoxic chambers or chemical inducers

There have been few *in vitro* models to induce dormancy in tumor cells thus far, and these models rely on using a hypoxic chamber or gas-controlled incubator. Conventional methods of studying hypoxia *in vitro* include (i) using a hypoxic chamber or gas-controlled incubator with an air-tight seal and introducing specific gas concentrations or (ii) inducing a hypoxia-mimicking response using chemical inducers (e.g. $CoCl_2$, deferoxamine; DFO). These two methods provide unique benefits, as well as limitations, for investigating cells under hypoxia to characterize dormant tumor cells. The hypoxic chambers employed in most previous studies have the advantage of not using chemicals that may change cell behavior independently of the hypoxic response. Endo et al. reported that AsPC-1, a pancreatic cell line, can survive 2-3 weeks of chronic hypoxia (1% O_2) maintained within a hypoxic chamber by entering a dormant state with no proliferation, no death, and metabolic suppression [31]. In another study by Prati et al., it was found that exposing MDA-MB-231 cells to three or more cycles of hypoxia (1% O_2) and reoxygenation using a gas-controlled incubator can establish a hypoxia-tolerating MDA-MB-231 cell line that can stably survive under 1% O_2 condition by entering a dormant state, as characterized by arrest in G0/G1 phase and low metabolism [32]. However, not all types

of experiments can be performed with hypoxic chambers as opening the chamber for manipulation (e.g. media change) is not allowed to maintain hypoxia. HIF1α, a master regulator protein of the cellular response to hypoxia, is highly unstable and rapidly destroyed upon exposure to oxygen, with an extremely short half-life of less than 5 minutes under normoxic conditions [33]. Thus, oxygen that reenters the chamber at each opening quickly establishes normoxia and reoxygenates the hypoxic cells, reducing the reliability of the system. Since repeated cycles of hypoxia and reoxygenation can trigger drastic changes of gene expression in some cell types [34,35], cell responses under fluctuations of hypoxia and reoxygenation in hypoxic chambers are likely different from actual *in vivo* hypoxic responses.

As opposed to the hypoxic chamber method, biochemical induction can stably provide hypoxic microenvironments regardless of oxygen level. Despite its well-characterized hypoxia-mimicking effects in many studies [36], the biochemical induction method has not been previously used to investigate cancer dormancy. In this dissertation, a well-known chemical inducer $CoCl_2$ was employed for stable biochemical induction of *in vitro* and *in vivo* hypoxia. Epstein et al. identified that cobalt ions can inhibit enzymatic degradation of HIF1α in the presence of oxygen by inactivating prolyl hydroxylases involved in proteasomal degradation of HIF1α [37]. The underlying mechanisms are not fully understood, but it has been suggested that cobalt replaces iron at the core of prolyl hydroxylase, which is essential for enzymatic activity. Additional evidence proposed by Yuan et al. suggested that cobalt inhibits the interaction between HIF1α and von Hippel-Lindau tumor suppressor protein (VHL) by direct binding to the VHL-binding domain of HIF1α, thereby preventing the degradation of HIF1α [38]. Since biochemical induction using $CoCl_2$ can stably mimic hypoxia without being affected by the presence of oxygen,

this method could enable facile molecular characterization of cancer dormancy that could not be performed in hypoxic chambers.

1.3.3. Biomaterials to study hypoxic regulation of cancer dormancy

Different *in vitro* and *in vivo* models of hypoxia-induced tumor dormancy can be also achieved by using biomaterials. In recent years, there has been a growing interest in utilizing components typically employed in tissue engineering (e.g., biomaterial scaffolds, hydrogels) to study the tumor microenvironment and its role in governing tumor dormancy. Fang et al. discovered that culturing cells in 3D hydrogel systems that limit the access of oxygen and nutrients can lead to reduced cell proliferation and quiescence [39]. When cancer cells were encapsulated in a transglutaminase-crosslinked gelatin gel (Col-gel) for a few days, gradually decreasing diffusion of nutrients and oxygen toward the center of the Col-gel induced quiescence or necrosis of encapsulated cells at the center, while higher proliferation of cells in the peripheral region of the gel was observed. Another study by Fluegen et al. used an implantable nano-intravital device that can deliver a sustained dose of DFO in defined microenvironments of solid tumors to mimic local hypoxia *in vivo* [29]. Delivery of DFO using the device implanted near the primary tumor was able to upregulate both hypoxia markers HIF1α and GLUT1 as well as dormancy markers DEC2, NR2F1, and p27 in a reversible manner.

While previous biomaterial-based systems have focused on recapitulating dormancy in primary tumor hypoxia, hypoxia also affects DTCs at metastatic sites, playing a critical role in dormancy of DTCs upon arrival. However, hypoxic regions within metastatic sites in the body are difficult to access with current imaging techniques. In

addition, there has been no experimental platform that allows investigation of how hypoxia induces and maintains dormancy at metastatic sites. As a consequence, many questions including why a hypoxic metastatic niche harbors dormant tumor cells and what causes cells to reawaken remain unsolved. To address this issue, poly(lactide-co-glycolide; PLG) scaffolds were used in combination with $CoCl_2$ in this dissertation. PLG scaffolds were previously shown to recruit metastatic cancer cells when implanted in mice by recapitulating the immune microenvironment of the metastatic niche, which is a key to tumor cell homing to secondary metastatic sites [40]. In addition, PLG scaffolds have been used for local delivery of various molecules *in vivo* [41]. Thus, PLG scaffolds that release $CoCl_2$ could establish an *in vivo* hypoxic niche that recruits metastatic cancer cells, enabling us to investigate mechanisms underlying hypoxic regulation of cancer dormancy at metastatic sites.

1.4. Dormancy is linked to chemoresistance in ovarian cancer metastasis

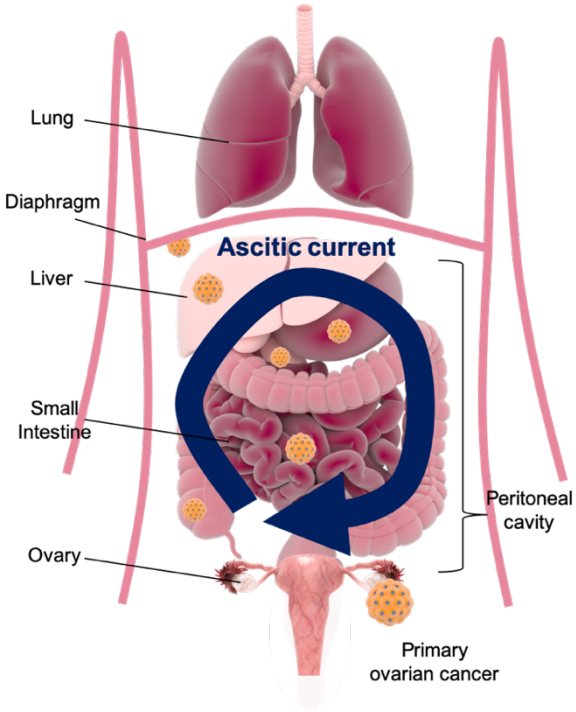

Figure 1-4. Dissemination of ovarian cancer spheroids from the primary tumor in ovarian cancer metastasis.

At the cellular level, ovarian cancer metastasis begins when tumor cells are shed into the peritoneal cavity, where they exist in suspension as multicellular spheroids [6]. The dissemination of ovarian cancer spheroids leads to the accumulation of large quantities of ascites, a malignant body fluid commonly developed in advanced ovarian cancer patients, in the peritoneal cavity [42]. Once suspended in ascites,

the disseminated ovarian cancer spheroids flow throughout the peritoneal cavity and seed the formation of secondary metastatic lesions (Fig. 1-4) [6,42].

As mentioned above, ovarian cancer has spread beyond the ovaries by the time of diagnosis in the majority of cases. Treatment options for ovarian cancer are much more limited than for breast cancer, with cytoreductive surgery platinum/taxane-based chemotherapy being the only treatment option for most patients. However, 20-30% of patients exhibit recurrence within 6 months of completing treatment, indicating that the cancer was chemoresistant [43], and frequent recurrence in patients with advanced disease remains a therapeutic challenge. For recurrent ovarian cancer, treatment options become even more limited as chemotherapy becomes ineffective. Thus, developing a novel therapeutic strategy that provides an alternative to destroy chemoresist cells as well as understanding the biology of chemoresistance have been urgent needs in ovarian cancer treatment.

Although mechanisms underlying the development of chemoresistance are still unclear, accumulating evidence has linked chemoresistance to dormancy in ovarian cancer. It has been suggested that a small subpopulation of dormant ovarian cancer spheroids persist during and after treatment of metastatic ovarian cancer, remain undetectable to current screening technologies, and evade chemotherapy [44,45]. These dormant spheroids can be reactivated when growth conditions become favorable, eventually seeding the formation of secondary metastatic lesions. Correa et al. discovered that tumor spheroids of ovarian cancer cell lines or spheroids isolated directly from patients' ascites were able to enter a dormant state to evade chemotherapy [45]. The dormant spheroids arrested in the G0/G1 phase exhibited reduced AKT (protein kinase B) activity as well as increased expression of retinoblastoma-like protein 2 (RBL2) and p27 CDK inhibitor, both of which

increase in expression during G0/G1 arrest. Importantly, dormant spheroids suspended in ascites were able to reactivate upon adhesion to surfaces and reinitiate proliferation in an AKT-dependent manner, suggesting that dormant spheroids present in patient ascites retain their ability to seed and grow as secondary metastatic lesions. In fact, the presence of ovarian cancer spheroids in ascites has been a negative prognosis factor for patient outcome in ovarian cancer. Thus, therapeutic strategies to eliminate ovarian cancer spheroids evading chemotherapy could reduce metastatic recurrence in ovarian cancer.

1.5. Therapeutic strategies to target ovarian cancer spheroids

1.5.1. Integrin inhibitors

Due to the unique metastatic pathway of ovarian cancer, in which the cells or spheroids detach from the primary ovarian tumor and disseminate throughout the peritoneal cavity by the flow of ascites, ovarian cancer rarely metastasizes beyond the peritoneal cavity. As the peritoneal cavity is lined by a continuous single layer of mesothelial cells, the mesothelial cell layer is the first layer which ovarian cancer spheroids adhere to. Thus, an increasing number of studies have been highlighting the importance of mesothelial adhesion of spheroids in ovarian cancer metastasis and therapeutic focus has been placed on disrupting the mesothelial adhesion to prevent reactivation of dormant cancer spheroids and formation of metastatic nodules.

The adhesion of ovarian cancer spheroids to the mesothelial layer is mediated through interactions between surface adhesion receptors of spheroids such as integrins and ECM proteins on the mesothelial layer such as fibronectin and collagens [46]. Several integrins have been identified as important mediators of ovarian cancer metastasis to the

mesothelial layer [6], suggesting that use of integrin inhibitors could be a therapeutic strategy to prevent the adhesion of spheroids to the peritoneal cavity. For instance, Casey et al. demonstrated that blocking α5β1 integrin completely inhibited spheroid adhesion to ECM proteins including fibronectin, laminin, and type IV collagen, suggesting that the α5β1 integrin-fibronectin interaction is essential for the spheroid adhesion at sites of secondary tumor growth [47]. In addition, Iwanicki et al. reported that interfering with the interactions between α5β1 integrin and fibronectin can significantly decrease spheroid-induced mesothelial clearance [48].

Some integrin inhibitors have progressed to clinical studies. For instance, Volociximab, an anti-α5β1 integrin antibody showed increased overall survival with reduced metastases and tumor burden in a mouse xenograft model of ovarian cancer [49]. However, in a phase II clinical trial with platinum-resistant, advanced stage ovarian cancer patients, Volociximab was not efficacious and led to adverse events in most patients (NCT00516841) [50]. Despite great progress towards targeting integrins and the promising effectiveness of integrin inhibitors in preclinical studies, none of the approaches using integrin inhibitors has demonstrated evident clinical benefit thus far [49–51]. These findings suggest that multiple receptors and ligands support adhesion of ovarian cancer spheroids to the mesothelial layer and that targeting a single molecule (i.e. integrin) will be insufficient to disrupt the complex interactions between ovarian cancer spheroids and mesothelial cells.

1.5.2. Potential use of biomaterials to eliminate ovarian cancer spheroids

The primary use of biomaterials in ovarian cancer therapy has been as a drug carrier to improve targeted delivery of platinum-based drugs by preventing premature activation before reaching the site of action or to deliver other sensitizer molecules that exert cytotoxic effects upon external triggers such as light for tumor-specific treatment [52]. Though therapeutic strategies using biomaterials have not been employed to specifically target ovarian cancer spheroids, a wide variety of biomaterials including polymer micelles, liposomes, and graphene-based materials have been exploited for ovarian cancer therapy. Among these biomaterial carriers, graphene-based materials have become a potential candidate for ovarian cancer therapy owing to their exceptional physiochemical properties [52,53].

Graphene is a one atom-thick densely packed network of 2D planar carbon atoms arranged in a hexagonal crystal lattice. Graphene-based materials exhibit different structural features, physicochemical properties, and biological responses based on the synthesis method [39]. Some examples of graphene-based materials include graphene nanoribbon (GNR), a ribbon-shaped graphene stack synthesized by unzipping multiwalled carbon nanotubes, and graphene oxide (GO), an irregularly or disk-shaped multilayered graphene nanoparticle synthesized from graphite. The hydrophobic planar structure of graphene with functional groups (e.g. epoxyl, carboxyl, hydroxyl groups) present on the planar surface and its edges allowing for covalent and noncovalent tethering of various amphiphilic functionalities to improve aqueous stability, biocompatibility, and even tumor targeting ability. In addition, the high surface area-to-mass ratio and the network of abundant hydrophobic pi bonds allow covalent and noncovalent functionalization strategies to increase loading of hydrophobic or aromatic anticancer drugs. Due to these

properties, functionalized forms of graphene-based materials are promising potential platforms for ovarian cancer therapy.

A recent study by Tiwari et al. reported that polyvinylpyrrolidone (PVP)-functionalized GO (GO-PVP) can be used as a carrier for anticancer drug cocktails composed of quercetin and gefitinib for ovarian cancer treatment [54]. The study revealed that the combined drug system loaded on the GO-PVP was significantly more effective than free drugs toward PA-1 ovarian cancer cells. Another study by Choi et el. reported that reduced GO–silver nanoparticle nanocomposites (rGO–Ag) can be used to selectively kill highly tumorigenic $ALDH^{+}CD133^{+}$ ovarian cancer stem cells by inducing the generation of toxic reactive oxygen species (ROS) as well as mitochondrial dysfunction [55]. Moreover, when combined with Salinomycin, a drug targeting cancer stem cells, rGO-Ag induced synergistic effects with up to 5-fold higher levels of apoptosis than Salinomycin alone, suggesting that rGO-Ag can be used in combination with chemotherapy. While these approaches have shown promising outcomes in ovarian cancer treatment, off-target damage in healthy tissues due to enhanced toxic effects are still a challenge to be addressed.

Recently, considerable research has been directed toward developing tumor-specific treatment with external triggers by which the therapeutic toxicity is generated only at the tumor site while the normal tissue or organ experiences minimal damage. Graphene-based materials have been widely used for photodynamic therapy (PDT) which uses photosensitizers that absorb incident light to generate toxic ROS. Multiple groups have reported that the chlorin e6 (Ce6) photosensitizer loaded onto GO functionalized with folic acid or polyethylene glycol (PEG) could be used for tumor targeting therapy [56,57]. Their results showed that Ce6 loaded onto GO can be activated by photo irradiation and kill

MGC803 human gastric cancer and nasopharyngeal epidermal carcinoma KB cells with negligible toxicity without light irradiation. Sonodynamic therapy (SDT) using ultrasound and sonosensitizers that generate toxic ROS upon ultrasound irradiation has also emerged as an alternative method to PDT since the low tissue-penetrating depth of light in PDT hinders the treatment of deep-seated tumors. In a recent report by Dai et al., reduced GO (rGO) loaded with a TiO_2 sonosensitizer enhanced SDT efficacy against cancer by taking advantage of the ultrathin planar nanostructure and abundant surface chemistry of rGO nanosheets [58]. Repeated SDT using rGO-TiO_2 could completely eradicate 4T1 breast tumor in nude mice without obvious recurrence over 2 weeks, while PDT or sensitizer alone exhibited rapid growth of tumor volume. While using treatment with external triggers has not been reported for ovarian cancer, these results from previous *in vitro* and *in vivo* investigations provide evidence that graphene-based materials can be utilized for photodynamic- and sonodynamic-based cancer therapy.

1.6. Overview of work completed in this dissertation

The scope of this dissertation is to establish *in vitro* and *in vivo* experimental platforms that enable investigation of cancer dormancy under hypoxic microenvironments in the primary tumor and metastatic target organs as well as to develop an alternative therapeutic strategy to destroy cancer cells evading chemotherapy to prevent metastatic recurrence. Chapter 2 will focus on an *in vitro* experimental platform using $CoCl_2$ to study breast and ovarian cancer dormancy under hypoxia. In Chapter 3, an *in vivo* experimental platform using PLG scaffolds with $CoCl_2$ to study hypoxic regulation of cancer dormancy at metastatic sites will be discussed. Chapter 4 presents a novel therapeutic strategy to

target ovarian cancer spheroids that are known to evade chemotherapy by using graphene-based materials for sonodynamic therapy. Future directions that warrant further study will be discussed in Chapter 5.

Chapter 2 – *In vitro* platform to study cancer dormancy under hypoxia using $CoCl_2$

Adapted with permission from "Lee, HR., Leslie, F., and Azarin, S.M. A facile *in vitro* platform to study cancer cell dormancy under hypoxic microenvironments using $CoCl_2$. Journal of Biological Engineering. 2018; 12: 12." Copyright 2018, Springer Nature

2.1 Introduction

During tumor progression, some disseminated tumor cells (DTCs) are capable of surviving in a prolonged quiescent state [59]. These dormant cells can reside at secondary sites without any clinical evidence for months to years before reawakening and causing metastatic recurrence [60,61], as evidenced by the large fraction of cancer patients who exhibit an asymptomatic period before metastatic relapse [59,62]. Developing strategies to destroy these dormant DTCs will require a better understanding of their unique biological characteristics, as they are able to evade current chemotherapeutic approaches that target rapidly dividing cells. It has been postulated that DTC dormancy could be induced by microenvironmental stresses encountered by the cells either within the primary tumor prior to dissemination or upon arrival at a secondary site [59,63]. Over the past few decades, significant effort has been directed toward understanding how microenvironmental cues regulate cancer dormancy [61,64,65]. However, the lack of suitable platforms to induce and maintain dormancy has limited the ability to probe the switch between dormant and active states in cancer cells.

Accumulating evidence in multiple types of cancer has revealed that dormant DTCs are detected in the bone marrow at a particularly high rate, suggesting that DTCs favor bone marrow despite its hostile microenvironmental conditions such as hypoxia and hypoglycemia [61,66]. Previous analysis of breast cancer cells has identified several genes

involved in dormancy that are regulated by hypoxia [67,68]. In addition, a recent study found that hypoxic microenvironments in the primary tumor give rise to a subpopulation of DTCs programmed to become dormant [25]. However, the precise role of hypoxia in regulating dormancy remains poorly understood due to a lack of well-established *in vivo* and *in vitro* models. Hypoxia studies are typically performed using incubation chambers that maintain an oxygen depleted environment through regulation of gas composition in the chamber [36,69]. These chambers limit the range of conditions that can be evaluated in an individual study, and the cells quickly establish normoxia each time they are removed for manipulation. *In vivo* models have the advantage of recapitulating the complex microenvironment of the tumor or metastatic site, but dormant cells are rare and thus it is difficult to identify and isolate them *in vivo.* In addition, regulation of hypoxia *in vivo* requires placement of mice in hypoxia chambers, which limits study size and also tunability of the hypoxic environment. *In vitro* models also present challenges, as the cells must be maintained in both hypoxic and dormant states, both of which are relatively unstable, during characterization. Thus, we sought to develop a robust *in vitro* model capable of stably inducing and maintaining dormancy of cancer cells under hypoxic microenvironments.

In this work, $CoCl_2$, a well-known hypoxia-mimetic agent, was used to establish hypoxia-mimicking microenvironments *in vitro*. The response to hypoxia is generally characterized by expression of the heterodimeric hypoxia induction factor 1 (HIF1) protein that consists of two subunits: HIF1α and HIF1β. HIF1β is constitutively expressed in the nucleus, whereas HIF1α is regulated by oxygen tension. It has been shown that the HIF-specific prolyl hydroxylases that facilitate HIF1α degradation have an iron-binding core, and the iron at this core is thought to be essential for their enzymatic activities [70]. This

iron can be replaced by cobalt, resulting in the inhibition of HIF1α degradation [70]. In addition, cobalt inhibits the interaction between HIF1α and von Hippel Lindau (VHL) protein, another protein involved in HIFα degradation, thereby preventing the degradation of HIF1α [38]. Since $CoCl_2$ mimics hypoxia by stabilizing HIF1α expression regardless of oxygen levels, this method has the advantage of being more stable than conventional hypoxic chambers. In addition, it has been demonstrated that $CoCl_2$ and true hypoxia result in similar regulation of hypoxia-related downstream targets such as erythropoietin and glucose transporter 1 (GLUT1) [71–73]. It has been documented that $CoCl_2$ can be used to mimic hypoxia in multiple cancer cell lines including breast and ovarian cancer cells [74,75]. While the ability of $CoCl_2$ to mimic hypoxic conditions in cancer cells has been established, it has not yet been demonstrated that the induction of dormancy in cancer cells lines in response to hypoxia can be recapitulated by $CoCl_2$.

In this manuscript, we evaluate whether $CoCl_2$-induced hypoxia-mimicking microenvironments can trigger and maintain dormancy *in vitro* in breast and ovarian cancer cell lines, with cancer dormancy defined as reversible quiescence throughout this report. Moreover, we show that $CoCl_2$ affects tumor dormancy directly through HIF1α stabilization by investigating effects of $CoCl_2$ on MCF-7 cells containing knockdown of HIF1α expression. In addition, we investigate whether the cellular response to $CoCl_2$ recapitulates the differential response to true hypoxia in estrogen receptor (ER)-positive and ER-negative breast cancer cells, which exhibit different dormancy signatures *in vivo* [67], to further validate our model. This $CoCl_2$-based model offers a facile tool for detailed investigation of cancer dormancy under hypoxic conditions, which could serve as an enabling platform to further understanding of how the dormant state is regulated in cancer cells.

2.2. Materials and Methods

Cell culture and growth analysis. The human breast cancer cell lines, MCF-7 and MDA-MB-231 (ATCC), were maintained in Dulbecco's Modified Eagle's Media (DMEM, 4500 mg/L glucose, Sigma Aldrich) supplemented with 10% (v/v) fetal bovine serum (FBS; Thermo Fisher Scientific) and 1% (v/v) penicillin-streptomycin (PS; Thermo Fisher Scientific). The human ovarian cancer cell line, OVCAR-3 (ATCC), was cultured in Roswell Park Memorial Institute 1640 (RPMI 1640) media supplemented with 10% (v/v) FBS, 1% (v/v) PS (Thermo Fisher Scientific), and 0.001% (w/v) bovine insulin (Sigma Aldrich). For cell growth analysis, cells were seeded at a density of 1×10^5 cells per well in 6-well plates or 35mm dishes. Prior to counting, cells were singularized using 0.25% trypsin-EDTA (Thermo Fisher Scientific) and treated with a 1:1 ratio of Trypan blue (Thermo Fisher Scientific), after which the live cell number was determined using a Countess II FL automated cell counter (Thermo Fisher Scientific).

Generation of cell aggregates and encapsulation of cells for three-dimensional (3D) models. Cell aggregates were generated using non-adhesive poly(2-hydroxyethyl methacrylate; pHEMA, Sigma Aldrich)-coated plates. pHEMA was dissolved in 95% ethanol to a final concentration of 3 mg/ml and sterile-filtered. The pHEMA solution was added to cell culture plates, which were left to dry overnight at room temperature. Cells were seeded in the pHEMA-coated plates at a density of 5×10^4 cells/cm^2 for aggregate generation. Collagen gels were prepared by diluting collagen type I (rat tail, Corning) with cell culture media to a final concentration of 2.5 mg/ml and neutralizing with 1N sodium hydroxide (Sigma Aldrich). Cells were mixed with the diluted collagen solution at a density

of 5×10^6 cells/ml, and 100 µl of the solution was plated in 35mm dishes and gelled at 37°C for 30 minutes. In order to harvest cells for characterization, cell aggregates were singularized by StemPro Accutase (Gibco) for 15 minutes with gentle pipetting, and collagen gels were dissociated by collagenase type 1 (Sigma Aldrich) for 15 minutes at 37°C.

$CoCl_2$ treatment and exposure to true hypoxia. For 2D cultures, treatment with $CoCl_2$ or true hypoxia was initiated when cells reached 50% confluence. For 3D cultures, treatment with $CoCl_2$ or true hypoxia was initiated immediately after cells were seeded in pHEMA-coated plates or embedded in collagen gels. For $CoCl_2$ treatment, $CoCl_2$ (Sigma Aldrich) was dissolved in distilled water and sterile-filtered. The resulting aqueous $CoCl_2$ solution was directly added to the cell culture media. Hypoxic culture was performed by incubating cells with 0.1% O_2 and 5% CO_2 in the EVOS FL Auto on-stage incubator (Thermo Fisher Scientific).

Cell cycle analysis. Cells cultured for the indicated time periods were singularized using 0.25% trypsin-EDTA (Thermo Fisher Scientific) and fixed with 70% ethanol for 1 hour at -20 °C. Then, cells were stained with 50 µg/mL propidium iodide (PI; Thermo Fisher Scientific) for 30 minutes in the dark at room temperature. Flow cytometric analysis of PI staining intensity was performed using a LSR II flow cytometer (BD Biosciences), and data were analyzed using Modfit LT software (Verity Software House) to determine cell cycle distribution.

Immunofluorescence assays. Cells grown on glass-bottom dishes or well plates were fixed with 4% paraformaldehyde for 10 minutes at room temperature. Cells embedded in collagen gels or cell aggregates grown in pHEMA-coated plates were fixed for 20 minutes at room temperature. Blocking and permeabilization were performed in blocking buffer, phosphate buffered saline (PBS) containing 10% Normal Goat Serum (Thermo Fisher Scientific) and 0.3% Triton X-100 (Sigma Aldrich), for 1 hour. Then, the cells were stained with rabbit anti-human Ki67 (D3B5; 1:400 dilution, Cell Signaling Technology), mouse anti-human HIF1α (54/HIF1α, 1:200, BD Biosciences), or mouse anti-human GLUT1 (SPM498, 1:200, Thermo Fisher Scientific) in antibody dilution buffer, PBS containing 1% bovine serum albumin (Sigma Aldrich) and 0.3% Triton X-100, overnight at 4 °C. Next, cells were labeled for 1 hour at room temperature with corresponding secondary antibodies: goat anti-rabbit Alexa Fluor 594 (1:1000, Thermo Fisher Scientific) for Ki67, goat anti-mouse Alexa Fluor 647 (1:1000, Thermo Fisher Scientific) for HIF1α, and goat anti-mouse Alexa Fluor 488 (1:1000, Thermo Fisher Scientific) for GLUT1. Nuclei were labeled with DAPI (300 nM, Thermo Fisher Scientific). Samples were imaged using an EVOS FL Auto fluorescence microscope, with the same light intensity and exposure time applied across all samples. Quantification was performed with ImageJ software (National Institutes of Health).

Western blotting. For protein extraction, cells were washed twice with ice-cold PBS and lysed using RIPA buffer (Thermo Fisher Scientific). Whole cell lysates were separated on a SDS-PAGE gradient gel (4-15%) and transferred to a polyvinylidene difluoride (PVDF) membrane (Bio-Rad). HIF1α, p21, p27, p38 mitogen-activated protein kinase (MAPK), phospho-p38 (pp38) MAPK, extracellular signal-regulated kinase (ERK(1/2)), and

phospho-ERK(1/2) (pERK(1/2)) were detected in 30 μg of whole cell lysates. β-actin was detected in 10 μg of whole cell lysates. The membranes were blocked in 5% non-fat dry milk (Bio-Rad) or bovine serum albumin (Sigma Aldrich) in Tris-buffered saline containing 0.05% Tween-20 (TBS-T; Sigma Aldrich) at room temperature for 1 hour. Next, the membranes were incubated with mouse anti-human HIF1α primary antibody (54/HIF1α, 1:1000, BD Biosciences) for 2 hours or HRP (horseradish peroxidase)-conjugated β-actin (13E5, 1:2000, Cell Signaling Technology) for 1 hour at room temperature. For p21, p27, p38 MAPK, pp38 MAPK, ERK(1/2), and pERK(1/2), the membranes were incubated with rabbit anti-human p21 primary antibody (12D1), rabbit anti-human p27 primary antibody (D69C12), rabbit anti-human p38 MAPK primary antibody, rabbit anti-human pp38 MAPK primary antibody, rabbit anti-human ERK(1/2) primary antibody and rabbit anti-human pERK(1/2) primary antibody (1:1000, Cell Signaling Technology) overnight at 4 °C. For HIF1α blots, the membrane was incubated with goat anti-mouse polyclonal HRP-conjugated secondary antibody (1:10000, Thermo Fisher Scientific) at room temperature for 45 minutes. For p21, p27, p38 MAPK, pp38 MAPK, ERK(1/2), and pERK(1/2), goat anti-rabbit polyclonal HRP-conjugated secondary antibody (1:2000, Cell Signaling Technology) was used. Protein expression was detected using SuperSignal West Pico Chemiluminescent substrate (Thermo Fisher Scientific) and a ChemiDoc Imager (Bio-Rad). Western blot quantification was performed by ImageLab (Bio-Rad). The p38 to ERK activity ratio was calculated as previously reported [76]. Briefly, quantified values for pp38 MAPK were divided by the values for total p38 MAPK and the same was done for pERK(1/2) and ERK(1/2). Then, the pp38 MAPK/p38 MAPK ratio value was divided by pERK(1/2)/ERK(1/2) ratio value.

Cell viability assays. The cell viability under $CoCl_2$ treatment was measured using a Live/Dead Viability/Cytotoxicity Kit (Thermo Fisher Scientific). For this assay, 1×10^5 cells per well were seeded in 6-well plates. After the indicated periods of $CoCl_2$ treatment, cells were washed with PBS twice and incubated with 2 μM calcein AM and 4 μM ethidium homodimer-1 for 30 minutes at room temperature. Imaging was performed using an EVOS FL Auto fluorescence microscope.

HIF1α knockdown in MCF-7 cells. For HIF1α suppression in MCF-7 cells, a HIF1α-specific shRNA construct in a lentiviral GFP vector was used (5' ACAAGAACCTACTGCTAATGCCACCACTA 3', OriGene, TL320380D). A non-effective scrambled shRNA cassette (5' GCACTACCAGAGCTAACTCAGATAGTACT 3', OriGene, TR30021) was used as a negative control. To produce lentiviral particles, human embryonic kidney 293T cells (HEK293T; kindly provided by Dr. Benjamin Hackel) were transfected with HIF1α-specific shRNA constructs and the Lenti-Vpak packaging kit (OriGene, TR30037) in Opti-MEM I (Thermo Fisher Scientific). Lentiviral particles were collected 24 hours after transfection and filtered through a 0.45 μm syringe filter (Merck Millipore). For transduction, MCF-7 cells were transduced with the lentiviral particles for 24 hours in DMEM containing 10% FBS and polybrene (8 μg/mL, Sigma Aldrich). Selection of successfully transduced cells was achieved by exposing the cells to DMEM containing 10% FBS and 0.5 μg/mL puromycin (Life Technologies) for one week, with media changes performed every 2-3 days.

Quantitative Real-time PCR (qRT-PCR). qRT-PCR was performed using a CFX Connect Real-Time PCR Detection System (Bio-Rad). Total RNA was extracted from cells

using a RNeasy Mini kit (Qiagen) followed by cDNA synthesis through the reverse transcription of 1 μg of total RNA using an Omniscript RT kit (Qiagen) according to the manufacturer's protocol. Quantitative PCR reactions were performed using iTaq Universal SYBR Green Supermix (Bio-Rad) and PrimePCR SYBR Green Assays (Bio-Rad) with primers specific to each of the target mRNAs: CDKN1A (qHsaCID0014498), CDKN1B (qHsaCID0012509), CDK2 (qHsaCED0043984), CDK4 (qHsaCED0003626), CCNA2 (qHsaCID0017452), CCND1 (qHsaCID0013833), CCNE1 (qHsaCID0015131), and MYC (qHsaCID0012921). TBP (TATA-box binding protein, qHsaCID0007122) was used as reference gene.

Senescence-Associated β-galactosidase assay. β-galactosidase activity was measured using the Senescence β-Galactosidase Staining Kit (Cell Signaling Technology). Briefly, cells were washed with PBS and fixed with 1x fixative solution for 15 minutes. Then, β-galactosidase staining solution with a final pH between 5.9 and 6.1 was prepared and added to fixed cells. Samples were sealed with parafilm to prevent evaporation and placed in a dry 37 °C incubator overnight. Imaging was performed using an EVOS FL Auto fluorescence microscope. For the positive control, cells were treated with 12.5 μM etoposide (Cell Signaling Technology) for 6 days and allowed to recover for 2 days in normal growth media.

Statistical Analysis. All data are represented as mean ± SD of three biological replicates from one of three representative independent experiments. P values were determined using an unpaired Student's t-test, with $P<0.05$ considered to be statistically significant. Statistical analysis was performed using GraphPad Prism.

2.3. Results

2.3.1. $CoCl_2$ treatment inhibits proliferation of MCF-7 cells

To explore the growth dynamics of MCF-7 cells under hypoxia-mimicking conditions induced by $CoCl_2$ treatment, MCF-7 cells were exposed to various concentrations of $CoCl_2$ (50-500 μM). Hypoxia-mimicking effects of $CoCl_2$ were verified under tested concentrations through comparison to true hypoxic conditions (0.1% O_2) by immunofluorescence analysis of HIFα and GLUT1 (Fig. 2-1A). Inhibition of MCF-7 proliferation without significant cell death was observed in a dose-dependent manner up to 300 μM and maintained for approximately 20 days under $CoCl_2$ treatment (Fig. 2-1B, C). At doses of 1 mM or higher, toxicity led to significant cell death, whereas doses lower than 50 μM did not result in distinguishable changes in cell growth (data not shown). Importantly, Ki67 (a cellular marker for actively cycling cells) was markedly attenuated in MCF-7 cells showing restrained growth under $CoCl_2$ treatment (Fig. 2-1B), implying that growth inhibition is in part attributed to emergence of a quiescent population of MCF-7 cells. In addition, the attenuated Ki67 expression and restrained growth of MCF-7 became more noticeable at 300 μM $CoCl_2$ than 100 μM $CoCl_2$, indicating the dose-dependent cellular response of MCF-7 to $CoCl_2$ treatment. Consistent with the restrained growth and attenuated Ki67 expression, during $CoCl_2$ treatment a significant increase in the cell population arrested in G0/G1 phase, a hallmark of the quiescent state, was observed through flow cytometric analysis of propidium iodide (PI) staining. In MCF-7 cells treated with 300 μM $CoCl_2$ for 6 days, 82.2 ± 0.1% of the cells were in G0/G1 phase, as compared to 55.0 ± 1.7% prior to $CoCl_2$ treatment (Fig. 2-1C). In addition, the population in S phase decreased from 32.6 ± 0.9% to 7.1 ± 0.3% after 6 days of $CoCl_2$ treatment (Fig. 2-1C). Taken together, the restrained growth in conjunction with downregulation of Ki67, actively

present in G1, S, G2 and M phases of the cell cycle but absent in G0 phase [77,78], and accumulation of cells in the G0/G1 phase by PI analysis demonstrate that at doses which increase HIF1α expression, $CoCl_2$-induced hypoxia-mimicking conditions can trigger dormancy in MCF-7 cells.

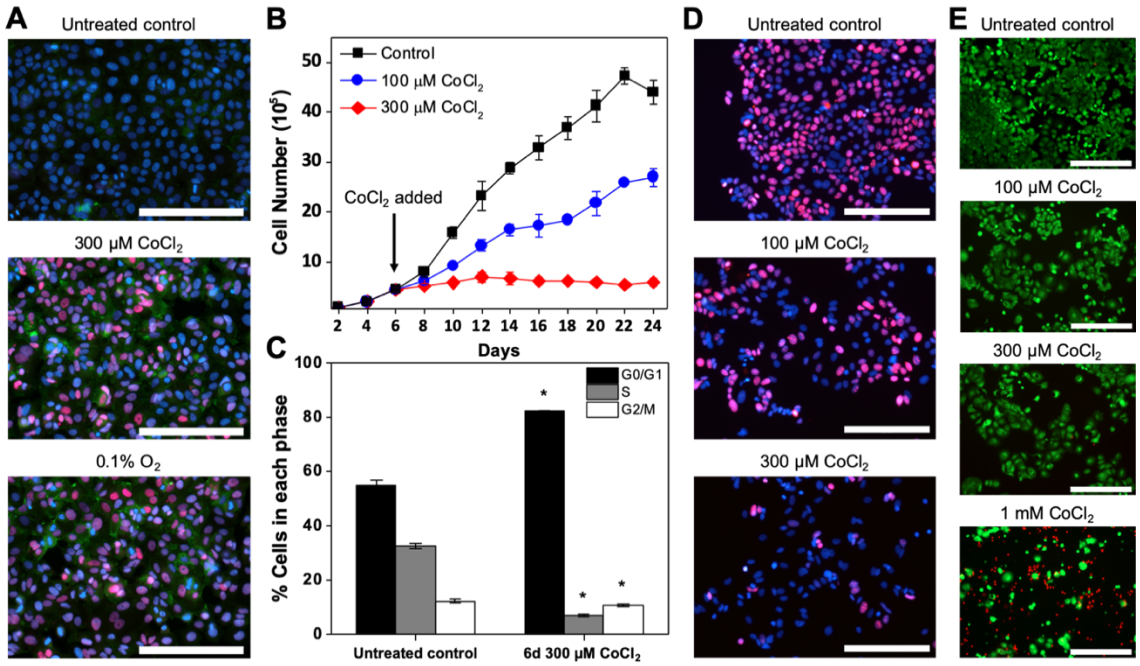

Figure 2-1. $CoCl_2$-induced hypoxia-mimicking conditions can lead to prolonged growth inhibition in MCF-7 cells. (A) Representative fluorescence images of HIF1α (red) and GLUT1 (green) expression in MCF-7 cells after 72 hours of treatment with 300 μM $CoCl_2$ or 0.1% O_2 compared to untreated control cells. Nuclei were stained with DAPI (blue). Scale bars indicate 200 μm. (B,C) Cell growth (B) and cell cycle distribution analysis using flow cytometry (C) of MCF-7 cells. Flow cytometry data were analyzed by Modfit LT software (* $P < 0.001$ compared to untreated control). (D) Representative fluorescence images of cell cycling marker Ki67 (red) expression in MCF-7 cells treated with 100 and 300 μM $CoCl_2$ for 6 days compared to untreated control cells (day 6 of culture). Nuclei were stained with DAPI. Scale bars indicate 200 μm. (E) Live/dead images of MCF-7 cells after 72 hours of treatment with varying concentrations of $CoCl_2$. Scale bars indicate 400 μm.

2.3.2. Dormant cells resume proliferation upon removal of $CoCl_2$

Unlike senescent cells, which are permanently trapped in a non-proliferative state, a hallmark of dormant cancer cells is the ability to reawaken upon removal of the environmental stresses that led them to enter dormancy, defined as reversible quiescence in this study [79,80]. Thus, we determined whether the cell growth inhibition under $CoCl_2$

treatment could be reversed. To this end, MCF-7 cells were treated with 300 μM $CoCl_2$ for 6 days (from day 4 to day 10 of cell culture) followed by recovery in the normal growth media (from day 10 to day 16, Fig. 2-2). Cell growth analysis showed that while proliferation was restrained during the 6-day $CoCl_2$ treatment period, cells resumed growth after removal of $CoCl_2$ (Fig. 2-2A), providing further evidence that growth-arrested cells under $CoCl_2$ treatment were dormant and not senescent. Reversible quiescence of MCF-7 cells under $CoCl_2$ treatment was also observed by Ki67 immunofluorescence analysis (Fig. 2-2B). The 6-day exposure to 300 μM $CoCl_2$ led to significant loss of Ki67 expression in the majority of MCF-7 cells (Fig. 2-2B, top right) as compared to control cells prior to treatment. After 12 days of $CoCl_2$ treatment without recovery, Ki67-positive cells were hardly seen, suggesting that most cells under prolonged hypoxia-mimicking conditions remained dormant (Fig. 2-2B, bottom left). When cells recovered from $CoCl_2$ treatment for 6 days, expression of Ki67 increased, indicating that cells were re-entering a proliferative state (Fig. 2-2B bottom right). Flow cytometric analysis following PI staining also confirmed reversible quiescence of MCF-7 cells under $CoCl_2$-induced hypoxia-mimicking conditions. After 6 days of recovery in normal growth media following $CoCl_2$ treatment, the percentage of cells arrested in G0/G1 decreased from 88.0 ± 1.2% at day 10 to 53.0 ± 0.4% at day 16, while the percentage of cells in S phase increased from 6.3 ± 0.1% to 30.9 ± 0.2% (Fig. 2-2C). This transient growth arrest of MCF-7 cells under $CoCl_2$ treatment indicates that MCF-7 cells were in a dormant state, as opposed to a senescent state. To further demonstrate that the cells were not senescent, we evaluated senescence-associated β-galactosidase activity. MCF-7 cells treated with $CoCl_2$ had low β-galactosidase activity similar to untreated cells, whereas MCF-7 cells treated with etoposide, a well-known inducer of cell senescence, exhibited higher β-galactosidase activity (Fig. 2-2D).

Collectively, these results confirm that MCF-7 cells under $CoCl_2$-induced hypoxia-mimicking conditions are dormant and resume proliferation when $CoCl_2$ is removed.

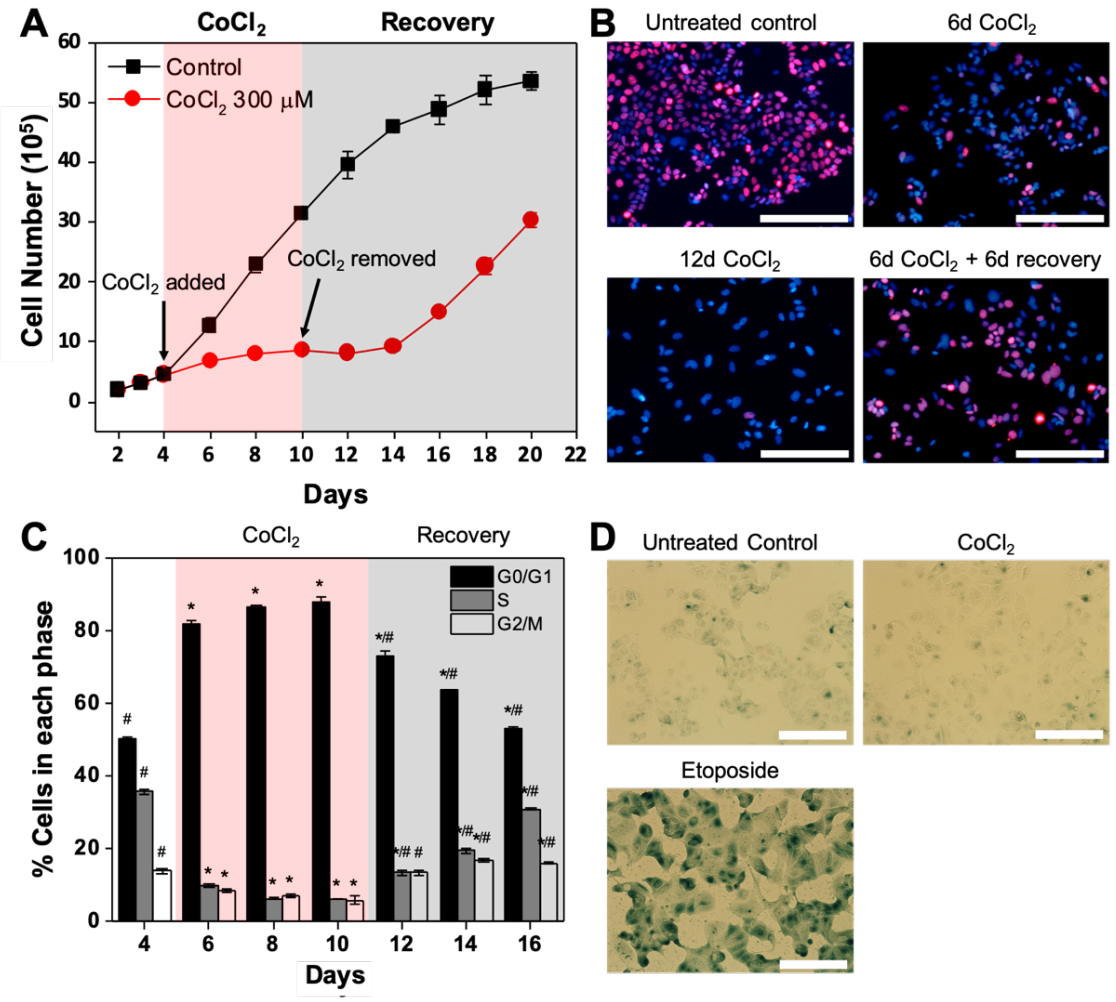

Figure 2-2. Quiescent MCF-7 cells can resume growth upon removal of $CoCl_2$. (A) Cell growth analysis of MCF-7 cells treated with 300 μM $CoCl_2$ for 6 days (from day 4 to day 10) compared to untreated control cells. Cells recovered in normal growth media after the 6-day $CoCl_2$ treatment. (B) Representative fluorescence images of cycling marker Ki67 (red) and nuclei (blue) in MCF-7 cells. Scale bars indicate 200 μm. (C) Flow cytometric analysis of PI staining intensity in MCF-7 cells treated with 300 μM $CoCl_2$ for 6 days (from day 4 to day 10), followed by recovery (from day 10 to day 16), compared to untreated control at day 4. Cell populations are reported as percentage of cells in each phase. Data were analyzed by Modfit LT software (* $P < 0.01$ compared to untreated control (day 4); $^{\#}$ $P < 0.01$ compared to 6-day $CoCl_2$ treatment (day 10)). (D) Representative bright field images of MCF-7 cells stained with β-galactosidase in each condition: untreated, 6-day 300 μM $CoCl_2$ treatment followed by 2-day recovery in normal growth media, and 6-day 12.5 μM etoposide treatment followed by 2-day recovery in normal growth media (positive control).

2.3.3. Induction of dormancy by $CoCl_2$ is similar to true hypoxia.

We subsequently compared cell responses under true hypoxic conditions and $CoCl_2$ treatment to confirm that dormancy hallmarks of MCF-7 cells under $CoCl_2$ and true hypoxia are similar. To this end, MCF-7 cells were exposed to 300 μM $CoCl_2$ or true hypoxic conditions (0.1% O_2). Cell growth analysis demonstrated similar inhibition of cell growth during the treatment period (Fig. 2-3A). During recovery, cells in both conditions resumed growth upon removal of either $CoCl_2$ or true hypoxia. The short delay observed in $CoCl_2$ treatment, but not in true hypoxia, could be attributed to the extended time required for elimination of residual $CoCl_2$ that has visibly accumulated within the cells, delaying recovery from hypoxia-mimicking conditions even after $CoCl_2$ has been removed from the culture media. Immunofluorescence analysis further supported that both conditions led to similar responses, with exposure to 300 μM $CoCl_2$ and 0.1% O_2 both leading to attenuated expression of Ki67 (Fig. 2-3B). Flow cytometric analysis of PI staining further demonstrated that both conditions led to a significant increase in the cell population arrested in G0/G1 phase, 80.0 ± 2.2% under true hypoxia and 92.5 ± 0.7% under $CoCl_2$ treatment (day 10), compared with 55.0 ± 1.8% in untreated MCF-7 cells (day 6; Fig. 2-3C). During normoxic recovery, a reduction in the arrested G0/G1 cell population was observed in both conditions, with 60.7 ± 3.2% G0/G1 phase cells in the population recovering from true hypoxia at day 12 and 64.0 ± 1.2% G0/G1 phase cells in the population recovering from $CoCl_2$ treatment at day 14 (Fig. 2-3C), indicating that cells under both conditions exhibited reversible quiescence. The increase in the G0/G1 cell population at day 14 observed in cells recovering from true hypoxia could be attributed to contact inhibition, as cells recovered and proliferated rapidly, reaching confluence in the

culture dish. Collectively, these results show that the regulation of cancer dormancy under true hypoxic conditions can be mimicked by $CoCl_2$.

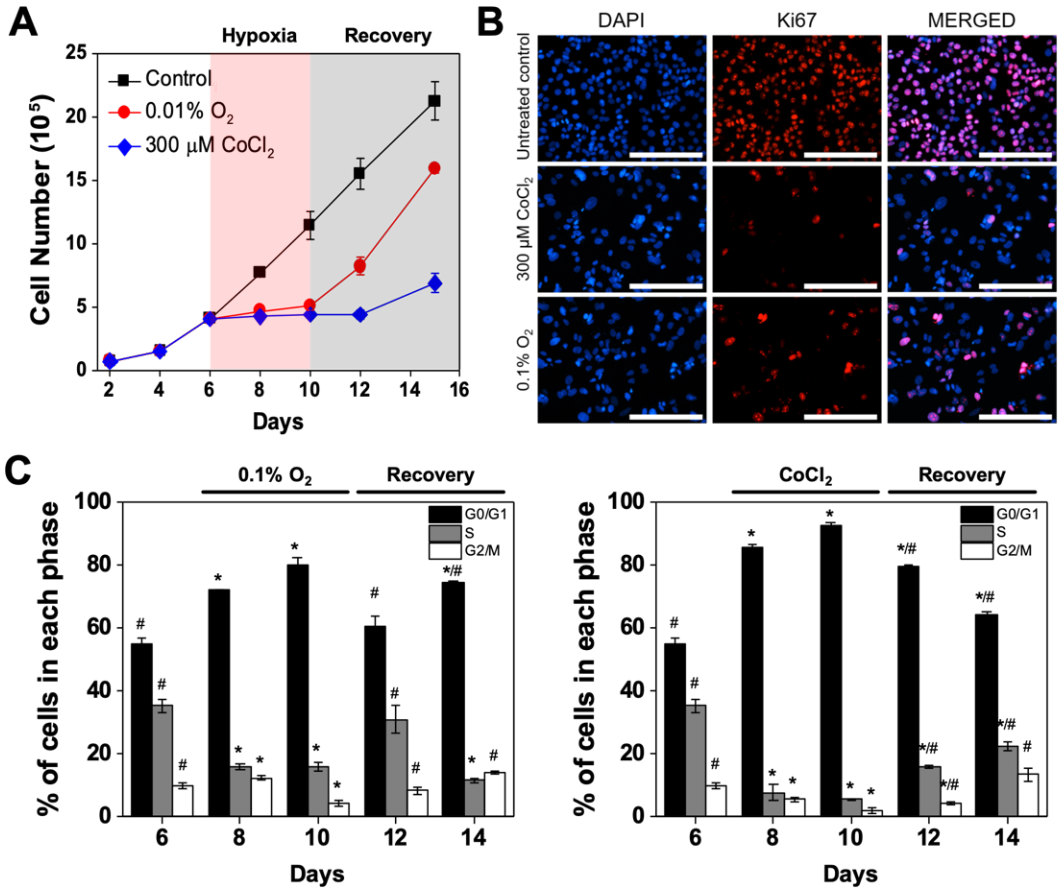

Figure 2-3. Induction of quiescence by $CoCl_2$ treatment is similar to effects of true hypoxia. (A) Cell growth analysis of MCF-7 cells treated with 300 µM $CoCl_2$ or true hypoxic conditions (0.1% O_2) for 4 days (from day 6 to day 10) compared to untreated cells. (B) Representative fluorescence images of Ki67 expression in MCF-7 cells after 6 days of exposure to 300 µM $CoCl_2$ or 0.1% O_2 compared to untreated control cells (day 6 of culture). Nuclei were stained with DAPI. Scale bars indicate 200 µm. (C) Flow cytometric analysis of PI staining in cells exposed to true hypoxic conditions (0.1% O_2, left) or 300 µM $CoCl_2$ treatment (right). Cell populations are reported as percentage of cells in each phase. Data were analyzed by Modfit LT software (* $P < 0.05$ compared to untreated control (day 6); $^{\#}$ $P < 0.05$ compared to day 10 of the respective condition)

2.3.4. Effects of $CoCl_2$ on cancer dormancy result directly from modulation of HIF1α

To verify that unknown effects of $CoCl_2$, separate from HIF1α-stabilizing effects, were not responsible for induction of cancer dormancy, we tested whether $CoCl_2$ could

induce dormancy in breast cancer cells in a HIF1α-independent manner. To this end, we knocked down HIF1α expression in MCF-7 cells using short hairpin RNA (shRNA). MCF-7 cells transduced with HIF1α-specific shRNA demonstrated significantly suppressed expression of HIF1α upon treatment with 300 μM $CoCl_2$, as compared to MCF-7 cells transduced with shRNA containing a scrambled sequence (Fig. 2-4A, B).

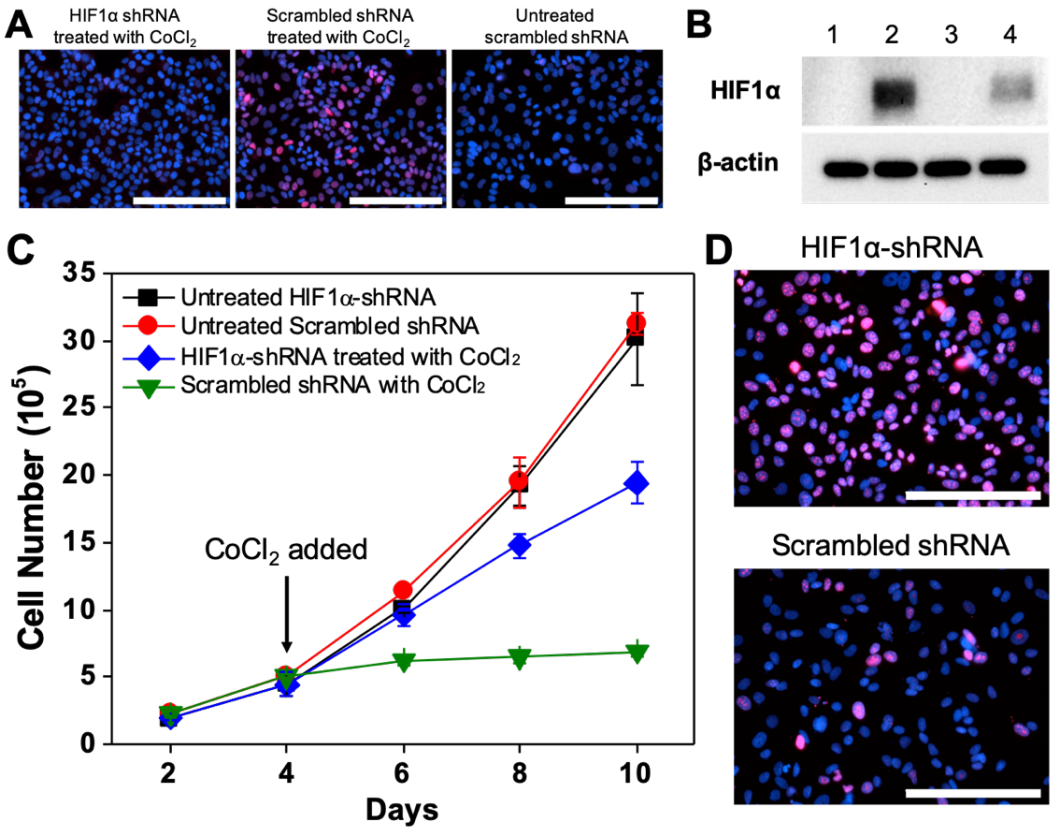

Figure 2-4. Induction of dormancy by $CoCl_2$ is dependent on HIF1α. (A) Representative fluorescence images of HIF1α expression in MCF-7 cells transduced with HIFα-specific shRNA (bottom row) and scrambled shRNA (middle row) after 72 hours of treatment with 300 μM $CoCl_2$ compared to untreated MCF-7 cells transduced with scrambled shRNA (top row). Nuclei were stained with DAPI. Scale bars indicate 200 μm. (B) Western blot analysis of HIF1α and β-actin expression in MCF-7 cells. Lanes 1-4 represent untreated control (lane 1), MCF-7 cells treated with 300 μM $CoCl_2$ for 72 hours (lane 2), HIF1α-silenced MCF-7 cells treated with 300 μM $CoCl_2$ for 72 hours (lane 3), and MCF-7 cells treated with true hypoxia for 72 hours (0.1% O_2, lane 4). (C) Cell growth analysis of HIF1α-suppressed MCF-7 cells treated with 300 μM $CoCl_2$ for 6 days (from day 4 to day 10) compared to untreated HIF1α-suppressed MCF-7 cells. Treated and untreated MCF-7 cells transduced with shRNA containing a scrambled sequence served as additional control groups. (D) Representative fluorescence images of Ki67 (red) and nuclei (blue) in HIF1α-suppressed MCF-7 cells (top) and MCF-7 cells transduced with scrambled shRNA (bottom) after 4-day treatment with 300 μM $CoCl_2$. Scale bars indicate 200 μm.

Furthermore, the growth of HIF1α-suppressed MCF-7 cells was less affected by 300 μM $CoCl_2$ treatment than MCF-7 cells transduced with scrambled shRNA, suggesting that restrained growth of MCF-7 cells under $CoCl_2$ is linked to the expression of HIF1α (Fig. 2-4C). The slight reduction in growth rate observed in HIF1α-suppressed MCF-7 at later timepoints could result from incomplete knockdown efficiency, as HIF1α expression is observed in some cells following $CoCl_2$ treatment (Fig. 2-4A). In addition, a significantly higher number of Ki67-positive cells was observed in HIF1α-suppressed MCF-7 cells after 4 days of 300 μM $CoCl_2$ treatment compared to MCF-7 cells transduced with scrambled shRNA (Fig. 2-4D). Collectively, these results demonstrate that the hypoxia-mimicking effects of $CoCl_2$ are responsible for its ability to modulate cancer dormancy.

2.3.5. $CoCl_2$ treatment induces dormancy in ovarian cancer cells

To confirm that the link between hypoxic microenvironments and cancer dormancy extends to other types of cancer, we subsequently investigated the ovarian adenocarcinoma cell line OVCAR-3 under $CoCl_2$ treatment. OVCAR-3 cells were found to have higher sensitivity to $CoCl_2$ than MCF-7 cells, showing similar hypoxic responses at 100 μM $CoCl_2$ to the MCF-7 response at 300 μM $CoCl_2$ (Fig. 2-5). OVCAR-3 cells treated with 100 μM $CoCl_2$ exhibited significant upregulation in HIF1α and GLUT1 expression compared with untreated cells, indicating that 100 μM $CoCl_2$ generated an effective hypoxia-mimicking microenvironment in OVCAR-3 cultures (Fig. 2-5A). Furthermore, growth patterns similar to MCF-7 under both $CoCl_2$ treatment and recovery were observed by cell growth analysis (Fig. 2-5B). In addition, Ki67 expression was markedly attenuated in cells showing restrained growth during $CoCl_2$ treatment (Fig. 2-5C,D), with 28.4 ± 3.3% Ki67-positive

cells in $CoCl_2$-treated populations, compared to 86.4 ± 2.8% in untreated populations. Importantly, reversible quiescence of OVCAR-3 cells was also observed by Ki67 expression, with the percentage of Ki67-positive cells increasing from 28.4 ± 3.3% after $CoCl_2$ treatment to 49.5 ± 3.7% after 6 days of recovery in normal growth media (Fig. 2-5C,D). Flow cytometric analysis of PI staining provided further evidence of reversible quiescence, with the percentage of G0/G1 phase cells increasing from 62.6 ± 1.2% in untreated cells to 78.2 ± 0.4% under $CoCl_2$ treatment and returning to 62.8 ± 0.7% after 6 days of recovery in normal growth media (Fig. 2-5E). These results show that $CoCl_2$ can also be used to induce and maintain dormancy in OVCAR-3 cells by establishing a hypoxia-mimicking microenvironment.

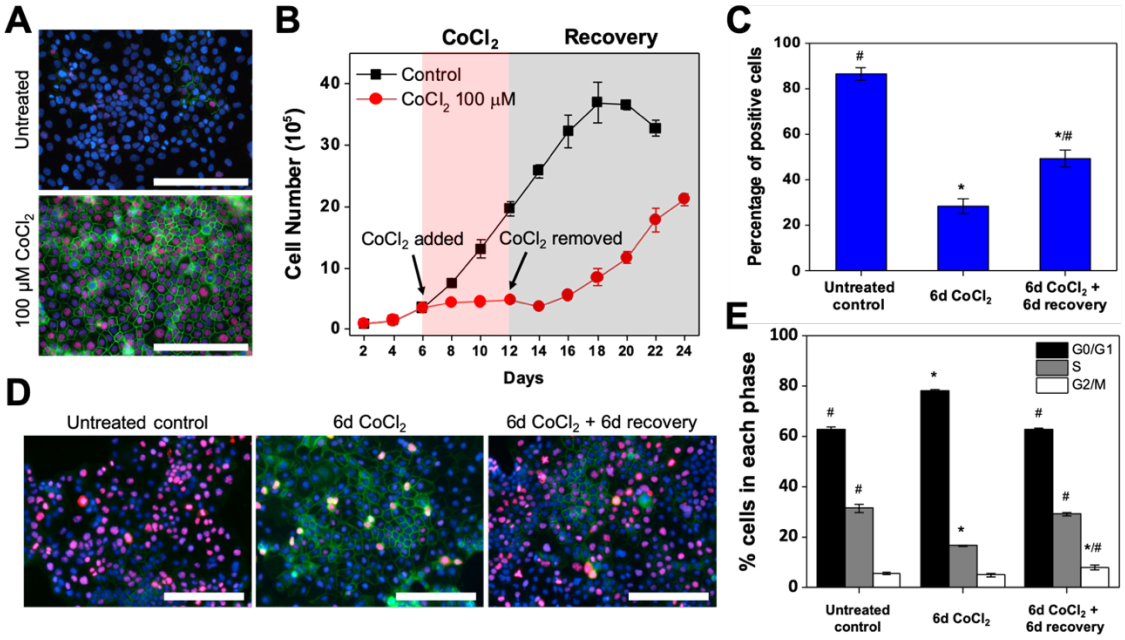

Figure 2-5. $CoCl_2$ treatment also induces dormancy in OVCAR-3 cells. (A) Representative fluorescence images of HIF1α (red) and GLUT1 (green) expression in OVCAR-3 cells after 72 h of 100 µM $CoCl_2$ treatment compared to untreated control cells. Scale bars indicate 200 µm. (B) Cell growth analysis of OVCAR-3 cells treated with 100 µM $CoCl_2$ for 6 days (from day 6 to day 12) compared to untreated cells. Cells recovered in normal growth media after the 6-day $CoCl_2$ treatment. (C) Percentages of Ki67-positive cells in untreated control, 6-day 100 µM $CoCl_2$ treatment, and 6-day 100 µM $CoCl_2$ treatment followed by 6-day recovery in normal growth media (* $P < 0.001$ compared to untreated control; $^{\#}$ $P < 0.001$ compared to 6-day $CoCl_2$ treatment). Quantification was performed with ImageJ software. (D) Representative fluorescence images of Ki67 (red), GLUT1 (green) and nuclei (blue) in OVCAR-3 cells in untreated control, 6-day 100 µM

$CoCl_2$ treatment, and 6-day 100 µM $CoCl_2$ treatment followed by 6-day recovery in normal growth media. Scale bars indicate 200 µm. (E) Cell cycle distribution of OVCAR-3 after 6-day treatment with 100 µM $CoCl_2$, or 6-day treatment with 100 µM $CoCl_2$ followed by 6-day recovery in normal growth media, compared to untreated control. Cell populations are reported as percentage of cells in each phase. Data were analyzed by Modfit LT software (* $P < 0.05$ compared to untreated control; $^{\#}$ $P < 0.05$ compared to 6-day $CoCl_2$ treatment).

2.3.6. $CoCl_2$-induced hypoxia-mimicking conditions recapitulate heterogeneous cellular response to hypoxia in breast cancer cell lines

It has been demonstrated that cellular responses to hypoxia vary depending on subtypes of cancer cells [25,81]. For example, unlike estrogen receptor (ER)-positive MCF-7 cells, hypoxic stress alone is not sufficient to induce dormancy *in vitro* in ER-negative MDA-MB-231 cells [25].

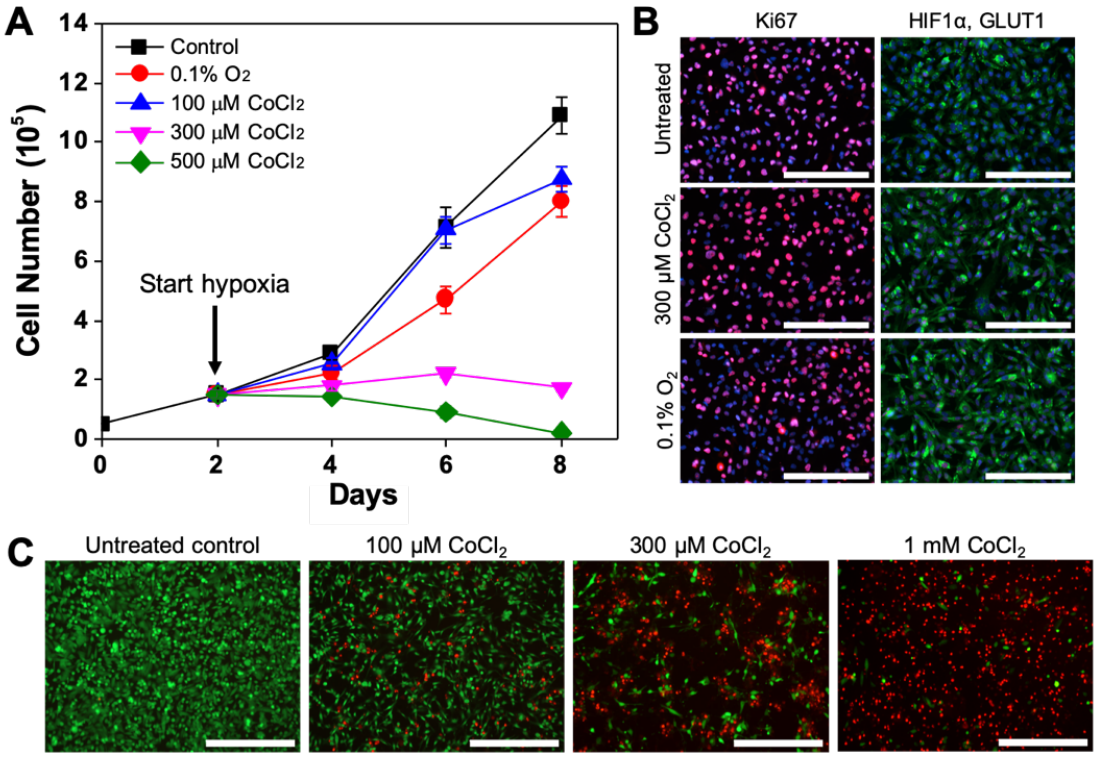

Figure 2-6. In vitro cellular responses to hypoxia in ER-negative MDA-MB-231 cells can be mimicked by $CoCl_2$. (A) Cell growth analysis of MDA-MB-231 cells treated with $CoCl_2$ (100, 300 and 500 µM) or true hypoxic conditions (0.1% O_2) for 6 days (from day 2 to day 8) compared to untreated cells. (B) Representative fluorescence images of Ki67 (red; left column), HIF1α (red; right column), GLUT1 (green; right column), and nuclei (blue) in MDA-MB-231 cells after 4 days of treatment with

300 μM $CoCl_2$ or 0.1% O_2, compared to untreated control cells (day 2 of culture). (C) Live/dead images of MDA-MB-231 cells after 72 hours of $CoCl_2$ treatment at varying concentrations. Scale bars indicate 400 μm.

Given that the *in vitro* cellular response of ER-positive MCF-7 cells to $CoCl_2$ treatment matched that of true hypoxia, we hypothesized that the same would hold for ER-negative breast cancer cells. To evaluate this hypothesis, ER-negative MDA-MB-231 cells were tested with $CoCl_2$ and true hypoxic conditions (0.1% O_2). Growth curve analyses showed that unlike MCF-7 cells, MDA-MB-231 cells did not exhibit restrained cell growth under true hypoxic conditions (0.1% O_2) (Fig. 2-6A). Although MDA-MB-231 cell growth was inhibited at higher doses of $CoCl_2$, given the lack of reduction in Ki67 expression (Fig. 2-6B) and the significant cell death observed (Fig. 2-6C), it is likely that the restrained cell growth can be primarily attributed to cell death, not induction of dormancy. Immunofluorescence analysis also showed that cellular responses of MDA-MB-231 to true hypoxia and $CoCl_2$ treatment were similar. HIF1α expression was upregulated in both true hypoxia and $CoCl_2$ treatment (Fig. 2-6B). In addition, no significant upregulation in GLUT1 was seen, and neither $CoCl_2$ treatment nor exposure to true hypoxia led to a decrease in Ki67 expression (Fig. 2-6B). These results suggest that $CoCl_2$ can recapitulate the *in vitro* cellular response to true hypoxia in heterogeneous breast cancer cell lines, further demonstrating the robustness of this platform for evaluating induction of breast cancer dormancy under hypoxia-mimicking microenvironments.

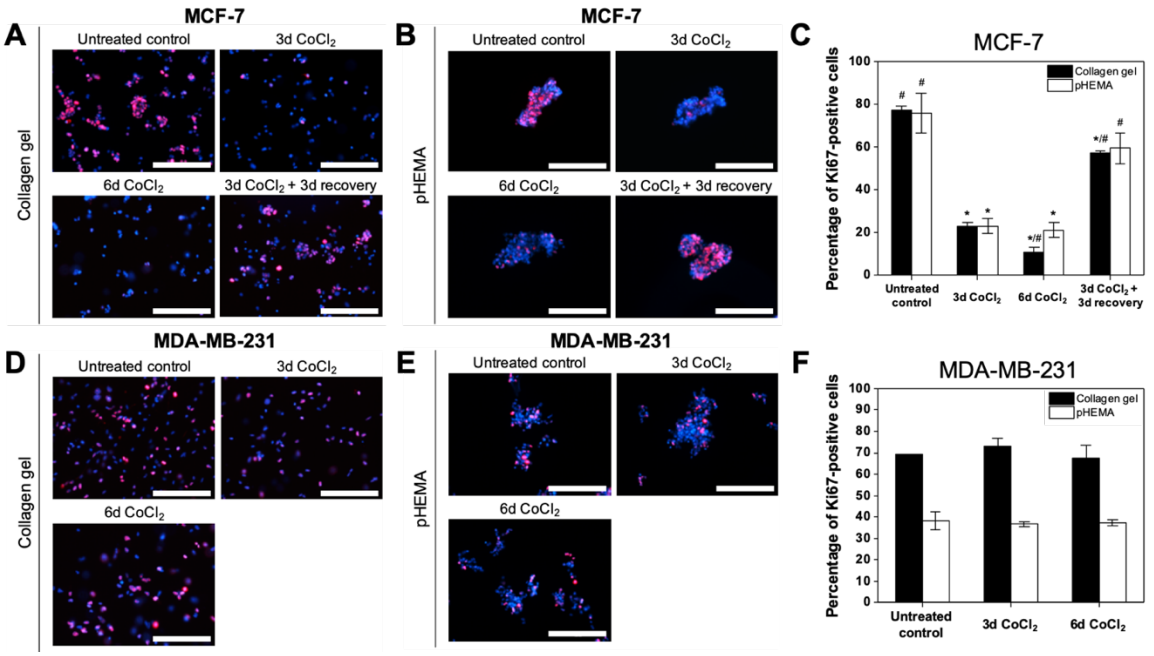

Figure 2-7. Differential hypoxic regulation of dormancy in MCF-7 and MDA-MB-231 cells can be recapitulated by $CoCl_2$ in 3D culture models. (A-C) Representative fluorescence images of cycling marker Ki67 (red) and nuclei (blue) in MCF-7 cells embedded in collagen gels (A) or grown in pHEMA-coated plates (B), and quantification of the percentage of Ki67-positive cells (C) in each condition: untreated, 3-day 300 μM $CoCl_2$ treatment, and 3-day 300 μM $CoCl_2$ treatment followed by 3-day recovery in normal growth media (* $P < 0.001$ compared to untreated control; $^{\#}$ $P < 0.005$ compared to 3-day $CoCl_2$ treatment). (D-F) Representative fluorescence images of cycling marker Ki67 (red) and nuclei (blue) in MDA-MB-231 cells embedded in collagen gels (D) or grown in pHEMA-coated plates (E), and quantification of the percentage of Ki67-positive cells (F) in each condition: untreated, 3-day 300 μM $CoCl_2$ treatment, and 6-day 300 μM $CoCl_2$ treatment. Quantification was performed with ImageJ software. Scale bars indicate 200 μm.

2.3.7. 3D cell culture models using $CoCl_2$ recapitulate cancer dormancy under hypoxia

We also demonstrated that $CoCl_2$ can be combined with 3D cell culture models to investigate cancer dormancy under 3D hypoxic microenvironments. For 3D models, cells were embedded in collagen gels or grown in non-adhesive pHEMA-coated plates. MCF-7 and MDA-MB-231 cells cultured in 3D were found to have stabilized HIF1α expression in response to $CoCl_2$, but only MCF-7 cells exhibited hallmarks of the dormant state,

consistent with our observations in in 2D culture. Ki67 expression in 3D-cultured MCF-7 cells decreased from 75.6 ± 9.3% (pHEMA) or 77.2 ± 1.9% (collagen gel) to 21.3 ± 3.6% (pHEMA) or 23.0 ± 2.0% (collagen gel) after 3-day $CoCl_2$ treatment, and recovered to 59.4 ± 7.3% (pHEMA) or 57.2 ± 1.1% (collagen gel) following 3-day recovery in $CoCl_2$-free normal growth media (Fig. 2-7A-C). Unlike MCF-7, MDA-MB-231 cells exhibited no significant change in Ki67 expression, which is also consistent with the results from 2D culture (Fig. 2-7D-F).

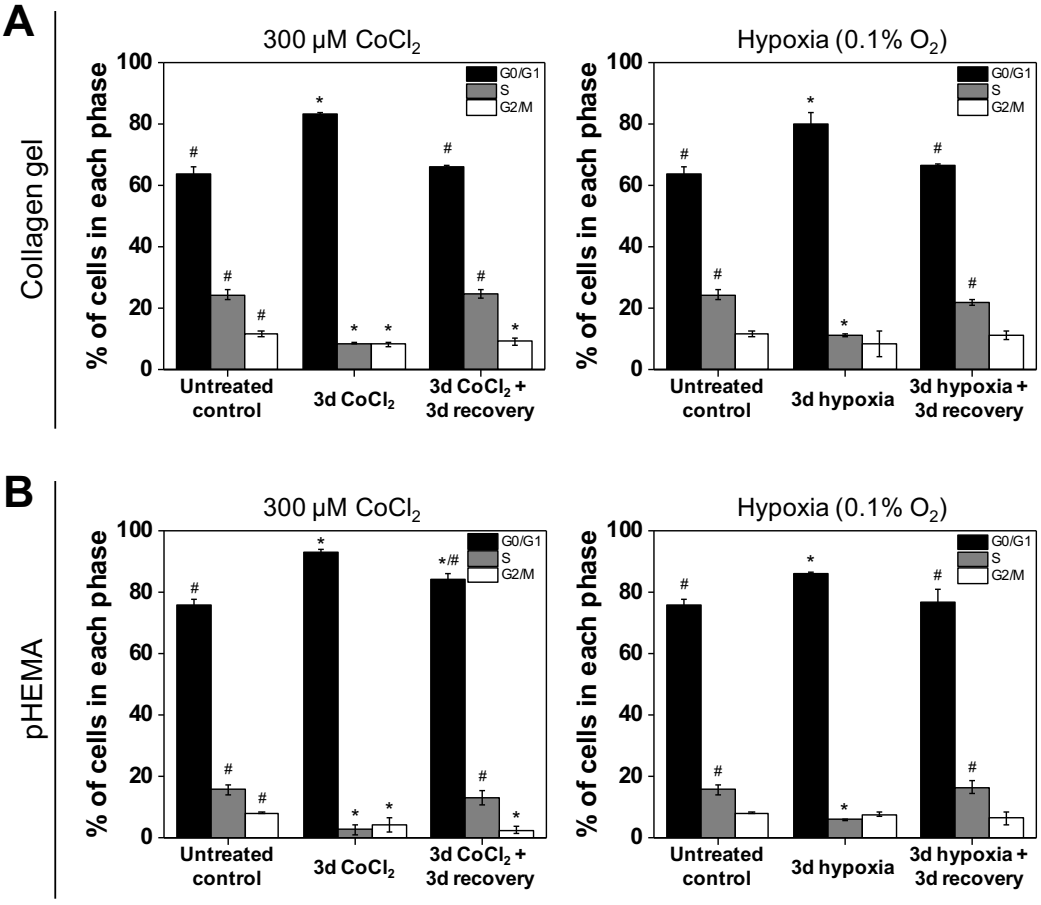

Figure 2-8. Induction of quiescence under hypoxia can be recapitulated by $CoCl_2$ in 3D cell culture models. (A,B) Flow cytometric analysis of PI staining in MCF-7 cells embedded in collagen gels (A) or grown in pHEMA-coated plates (B). Cells were exposed to 300 μM $CoCl_2$ treatment (left) or true hypoxic conditions (0.1% O_2, right). Cell populations are reported as percentage of cells in each phase. Data were analyzed by Modfit LT software (* $P < 0.05$ compared to untreated control; $^{\#}$ $P < 0.05$ compared to 3-day treatment with the respective condition).

Cell cycle analysis also demonstrated reversible quiescence of MCF-7 cells, with an increased percentage of cells arrested in G0/G1 phase under $CoCl_2$ treatment compared to untreated cells, and release from G0/G1 phase upon removal of $CoCl_2$ in both 3D culture models (Fig. 2-8). Importantly, these key features of the dormant state were also found in 3D-cultured MCF-7 cells under true hypoxic conditions (0.1% O_2), suggesting that the 3D $CoCl_2$-based platform can also recapitulate cellular responses to hypoxia (Fig. 2-9).

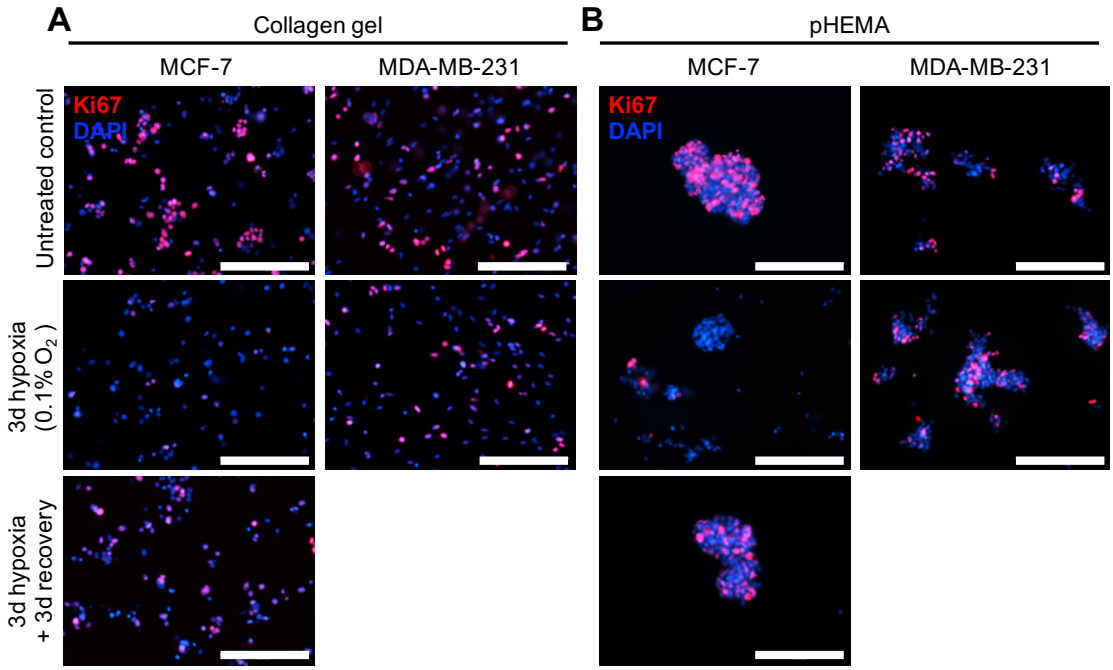

Figure 2-9. Differential Ki67 expression in response to true hypoxia is observed in MCF-7 and MDA-MB-231 cells in 3D culture systems. Representative fluorescence images of Ki67 expression in MCF-7 and MDA-MB-231 cells embedded in collagen gels (A) or grown in pHEMA-coated plates (B) in each condition: untreated, 3-day treatment with 0.1% O_2, and 3-day treatment with 0.1% O_2 followed by 3-day recovery in normal growth media (MCF-7 only). Nuclei were stained with DAPI. Scale bars indicate 200 μm.

Furthermore, MCF-7 cells cultured in 2D and 3D systems under $CoCl_2$ treatment exhibited similar key signaling features of dormant cells. Western blot analysis of p38 MAPK and ERK(1/2) activity showed that MCF-7 cells treated with $CoCl_2$ for 6 days had an increased ratio of p38 MAPK phosphorylation to ERK(1/2) phosophorylation, which has been

reported as a signaling hallmark of the dormant state [76,82], in both 2D and 3D cultures (Fig. 2-10). These results suggest that the $CoCl_2$-based platform is not limited to 2D culture but also can be combined with well-established 3D cell culture models to study cancer dormancy under hypoxic microenvironments.

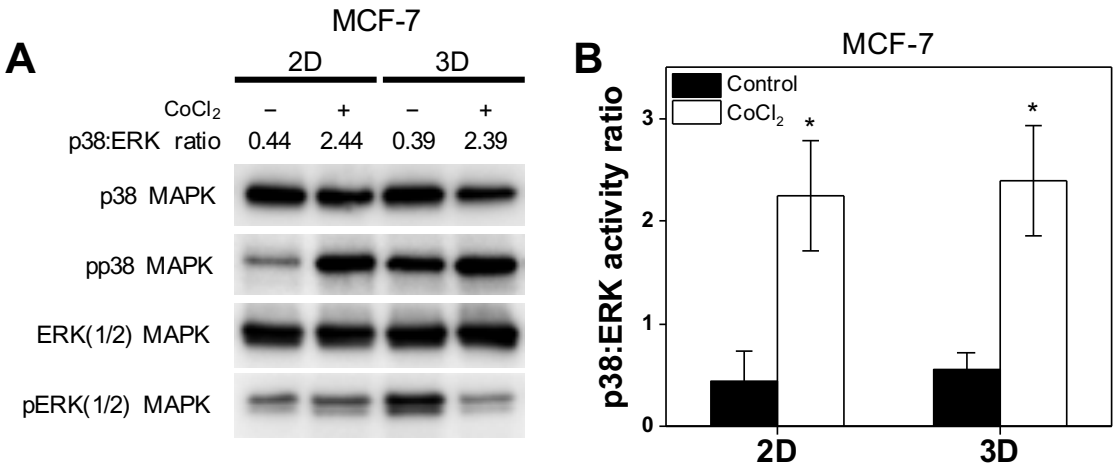

Figure 2-10. $CoCl_2$-treated MCF-7 cells exhibit an increased p38 to ERK activity ratio, a signaling hallmark of dormant state, in both 2D and 3D models. (A) Western blot analysis of p38 MAPK, phosphorylated p38 (pp38) MAPK, ERK(1/2) and phosphorylated ERK(1/2) (pERK(1/2)) in MCF-7 cells after 72 hours of $CoCl_2$ treatment compared to untreated control in 2D and 3D (pHEMA-coated plate) cultures. (B) Quantification of p38 to ERK signaling activity ratios in 2D and 3D-cultured MCF-7 cells from the western blot analysis, with results represented as mean ± SD of three independent experiments (* $P < 0.001$ compared to untreated control).

2.3.8. $CoCl_2$ treatment differentially regulates gene and protein expression in MCF-7 and MDA-MB-231 cells

To investigate possible molecular mechanisms that lead to differential responses to hypoxic microenvironments in MCF-7 and MDA-MB-231 cells, expression profiles of cell cycle-associated genes under $CoCl_2$ treatment were examined. Protein and gene expression of the CDK inhibitor p27 (*CDKN1B*) showed no upregulation in response to $CoCl_2$ treatment in MCF-7 cells, while p21 (*CDKN1A*) was significantly upregulated by $CoCl_2$. In contrast, no significant change in the expression of either p27 or p21 was observed in

MDA-MB-231 cells (Fig. 8A-C). p21 inhibits the cell cycle through inactivation of multiple CDK-cyclin complexes [33,83]: CDK2-cyclin E (*CCNE1*), CDK2-cyclin A (*CCNA2*) and CDK4-cyclin D1 (*CCND1*). Accordingly, p21 upregulation was accompanied by downregulation of *CDK2, CCNE1, CCNA2, CDK4,* and *CCND1* in MCF-7 cells treated with $CoCl_2$ (Fig. 8A). Furthermore, *MYC*, a proto-oncogene that plays an integral role in hypoxic adaptation [84], also exhibited differential expression, with significant downregulation in MCF-7 cells and upregulation in MDA-MB-231 cells upon treatment. These findings collectively suggest that $CoCl_2$ treatment in MCF-7 and MDA-MB-231 cells impacts different molecular mechanisms, giving rise to their distinct responses to $CoCl_2$ treatment.

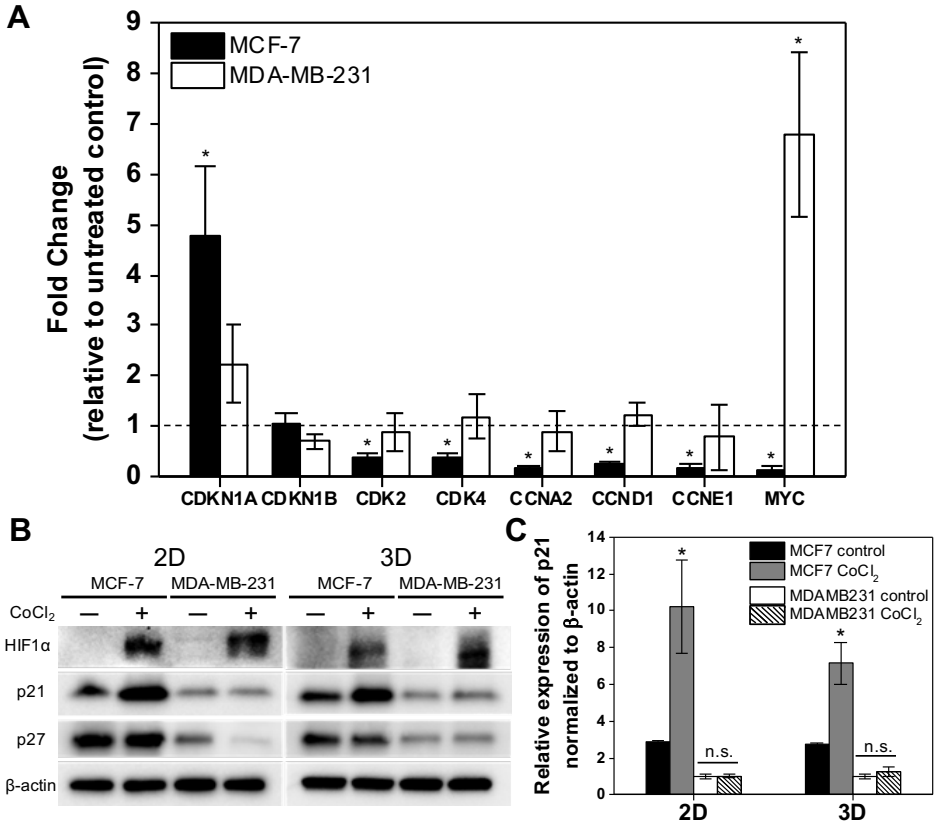

Figure 2-11. MCF-7 and MDA-MB-231 cells exhibit differential gene and protein expression profiles in response to $CoCl_2$ treatment. (A) Fold change in mRNA expression of *CDKN1A*, *CDKN1B, CDK2, CDK4, CCNA2, CCND1, CCNE1,* and *MYC* by qRT-PCR after 72 h of $CoCl_2$ treatment relative to

untreated control (* $P < 0.05$ compared to untreated control). (B) Western blot analysis of HIF1α, p21, p27 and β-actin (control) expression in MCF-7 and MDA-MB-231 cells after 72 h of $CoCl_2$ treatment in 2D and 3D (pHEMA-coated plate) cultures compared to untreated control. **c** Relative protein expression of p21 normalized to β-actin, with results represented as mean ± SD of three independent experiments (* $P < 0.05$ compared to untreated control).

2.4. Discussion

This study demonstrates that a $CoCl_2$-based platform can be used for investigation of cancer dormancy under hypoxia. Several types of models recapitulating the interactions between microenvironments and DTCs have been suggested to date, with a focus on cellular[85] and molecular [16,86] components such as stromal cells and the extracellular matrix. However, there have been few models focused on non-cellular factors such as oxidative stresses in local microenvironments [87,88], which may also play a critical role. Previous studies of breast cancer have identified that breast cancer cells under hypoxia became dormant, as evidenced by upregulation of several genes implicated in cancer dormancy [25,32]. In addition, restrained growth with reversible arrest in G0/G1 phase was observed in breast cancer cells under hypoxia, supporting hypoxic regulation of cancer dormancy [89]. Given the emerging evidence of hypoxic regulation of entrance into the dormant state, the establishment of a robust *in vitro* model of cancer dormancy under hypoxia is critical for better understanding of mechanisms through which hypoxia induces dormancy of DTCs.

Our results demonstrated that $CoCl_2$-induced hypoxia-mimicking conditions can stably trigger and maintain dormancy in MCF-7 cells in a HIF1α-dependent manner. $CoCl_2$ treatment showed similar effects to those of a conventional hypoxia chamber in restraining proliferation of MCF-7 cells, reducing expression of cell cycling marker Ki67 in conjunction with upregulation of hypoxia markers HIF1α and GLUT1 and reversible cell

cycle arrest in G0/G1 phase. Furthermore, OVCAR-3 ovarian cancer cells also exhibited these hallmarks of dormancy in $CoCl_2$-induced hypoxia-mimicking microenvironments. Unlike breast cancer, a direct link between hypoxia and ovarian cancer dormancy has not yet been fully established. However, it has been documented that several pathways including autophagy [90,91] and p38 signaling [92] that have been implicated in ovarian cancer dormancy are affected by hypoxia. Collectively, these results suggest that this $CoCl_2$-based platform can be used as a tool to study dormant cancer cells under hypoxia.

Previous studies have identified multiple effects of $CoCl_2$ beyond hypoxia-mimicking effects, such as the development of reactive oxygen species [93] and the activation of NF-κB signaling, which mediates carcinogenesis [94]. Since $CoCl_2$ treatment was unable to induce dormancy in MCF-7 cells when HIFα was downregulated in the cells, it is likely that $CoCl_2$ is inducing dormancy in a HIF1α-dependent manner. However, given the heterogeneity of cellular responses to hypoxia and $CoCl_2$ in different types of cancer, further investigation into alternative effects of $CoCl_2$ apart from mimicking hypoxia may be necessary in the future.

Unlike ER-positive MCF-7 cells, ER-negative MDA-MB-231 cells did not exhibit dormant behavior under either true hypoxia or $CoCl_2$ treatment. Previous studies have identified heterogeneity in cellular responses to hypoxia in different subtypes of breast cancer cell lines [81,89,95]. However, the underlying mechanisms that give rise to their differential ability to enter a dormant state in hypoxic microenvironments have yet to be elucidated. In our study, CDK inhibitor p21 and its associated CDKs and cyclins exhibited contrasting expression in MCF-7 and MDA-MB-231 cells under $CoCl_2$ treatment. These results are consistent with previous findings that differential regulation of p21 in MCF-7 and MDA-MB-231 cells in response to various environmental stimuli impacts cell cycle

progression [96,97], and they suggest that the distinct responses to hypoxic stress we observed in these two cell lines are in part p21-mediated. Interestingly, expression of *MYC*, which represses p21 in normoxia [84,98], exhibits the opposite trend as p21 in MCF-7 and MDA-MB-231 cells. Previous studies have found that hypoxia induces p21 activation by repressing *MYC* through a different regulatory mechanism from the classical hypoxia-inducible genes such as *GLUT1* [84,98]. Thus, MDA-MB-231 cells may overcome hypoxia-induced cell cycle arrest by overexpressing *MYC*, which in turn deactivates p21 to enable cell cycle progression. Another CDK inhibitor (p27) was not significantly upregulated in either cell line under $CoCl_2$ treatment. Given that hypoxia can induce cell cycle arrest independent of p27 or p21 [99], our findings suggest that dormancy observed in MCF-7 cells under $CoCl_2$ treatment is in part mediated by p21 upregulation but not p27. p21 can also trigger cellular senescence in a chronic state of G0 cell cycle arrest [83]. However, low activity of senescence-associated β-galactosidase in MCF-7 cells under $CoCl_2$ treatment indicated that cells were not in a senescent state. In addition, an increased ratio of p38 MAPK activity to ERK(1/2) activity, which has been associated with p21 activation in dormant tumor cells [82,100], was observed in MCF-7 cells under $CoCl_2$ treatment, providing further evidence of p21-mediated dormancy. Overall, our findings suggest that MCF-7 and MDA-MB-231 employ different molecular mechanisms that are in part regulated by p21-mediated pathways in response to hypoxic microenvironments. Although the role of p21 in hypoxic regulation of dormancy remains to be determined, these findings suggest that our platform can be used to investigate molecular mechanisms underlying hypoxic regulation of cancer dormancy.

As with other *in vitro* models, this simplified platform also reflects limited aspects of *in vivo* tumor microenvironments. It lacks geometrical complexity, cellular components

including immune cells and organ-specific stromal cells, and extracellular matrix components. However, as opposed to conventional hypoxia models that rely on a hypoxic chamber, the $CoCl_2$-based platform can be readily integrated with previously established models centered on cellular and molecular components to better mimic *in vivo* tumor microenvironments conducive to cancer dormancy. For example, we demonstrated that $CoCl_2$ can be combined with 3D cell culture models, which more closely mimic the *in vivo* tumor microenvironment than 2D monolayer cell culture [100]. Our results showed that $CoCl_2$ recapitulated differential hypoxic regulation of cancer dormancy in MCF-7 and MDA-MB-231 cells in two different 3D models, further indicating the robustness of this platform. Furthermore, this platform allows for real-time characterization of dormant cancer cells that has not been practical with hypoxic chambers due to the extremely short half-life of HIF1α ($t_{1/2}$ < 5 min) upon reoxygenation [33]. Thus, oxygen entering the chamber at each opening results in re-oxygenation that can disrupt the hypoxic response [36,101]. In addition, the ability to generate a large population of dormant cells in the $CoCl_2$ platform could enable the investigation of the heterogeneity among dormant cancer cells under hypoxia. Given that hypoxia and cancer dormancy have been associated with limiting the effectiveness of chemotherapy and increasing the risk for recurrence, resulting in poor clinical outcomes [102,103], information extracted from dormant cancer cells has the potential to identify novel therapeutic strategies for preventing recurrence. Taken together, the $CoCl_2$-based platform we have established in this report provides an enabling tool that has potential use in the investigation of undiscovered mechanisms of cancer dormancy regulation under hypoxic microenvironments.

2.5. Conclusion

There have been a limited number of studies on cancer dormancy under hypoxic microenvironments in part due to a lack of well-established platforms. In the present study, we report a facile $CoCl_2$-based *in vitro* platform mimicking hypoxic regulation of cancer dormancy as well as recapitulating differing responses to hypoxia among breast cancer cell lines. A critical advantage of this $CoCl_2$-based platform over conventional systems is the ability to stably induce and maintain dormancy *in vitro*, even in the presence of oxygen. Thus, this platform enables investigation of the poorly-understood molecular mechanisms underlying hypoxic regulation of cancer dormancy, offering a tool to develop potential therapeutic strategies to reduce tumor recurrence.

Chapter 3 – *In vivo* biomaterial platform to establish a hypoxic metastatic niche

3.1. Introduction

Hypoxia, a condition resulting from the deficiency of available oxygen within cells or tissues, has been recognized as a potent mediator of tumor metastasis, with wide-ranging regulatory roles in multiple steps of the metastatic cascade [102,104–106]. Previous reports have identified that tumor hypoxia and activation of hypoxia-inducible factor (HIF) signaling influence most elements of early and late-stage metastasis, including the epithelial-mesenchymal transition, invasion, intravasation and extravasation, metabolic adaptation, survival and growth at distant organs [107–109]. In addition, hypoxia has been found to be a master regulator of the formation of the pre-metastatic niche, facilitating metastatic progression [105,110,111]. However, most previous investigations of hypoxic regulation during metastasis have been centered on the effects of primary tumor hypoxia. Given that hypoxic effects are not just confined to the primary tumor, as DTCs can also encounter hypoxic microenvironments upon arriving at target organs, the precise mechanisms through which hypoxia in the metastatic niche affects the fate of DTCs during the late stages of metastasis need to be better characterized.

Recently, the significance of hypoxic regulation at target organs has been recognized in several studies [63,68,112,113]. For instance, hypoxic microenvironments in the liver were found to select for a subpopulation of DTCs with the ability to adapt to

metabolic stresses under hypoxia in colorectal cancer [109]. Moreover, it was found that hypoxia mediates the metabolic adaptation of metastatic breast cancer cells in the liver through the activation of HIF1 and pyruvate dehydrogenase kinase 1 (PDK1), a HIF1 target gene that mediates glycolytic reprogramming [114]. The hypoxic microenvironment in secondary target organs can also determine whether DTCs enter a dormant or proliferative state. Johnson et al. found that hypoxia regulates leukemia inhibitor factor receptor (LIFR) signaling, which can confer a dormant phenotype in breast cancer cells disseminated to bone marrow [68], a popular hypoxic metastatic niche for dormant DTCs in many types of cancer [59]. Aguirre-Ghiso et al. proposed a different view, that growth-suppressive target organ microenvironments such as hypoxia can activate stress signals in DTCs, consequently inducing dormancy of DTCs in conjunction with primary tumor hypoxia [59,63,115]. Hypoxia also plays a central role in late stages of metastasis at target organs, which require the establishment of new vasculature for growth of the metastases. Folkman et al. suggested that the failure to construct new vasculature at target organs may result in dormant metastases, a phenomenon termed angiogenic dormancy [116]. Hypoxia stimulates angiogenesis through HIF signaling, which leads to the production of vascular endothelial growth factor-A (VEGF-A), a proangiogenic factor, in hypoxic tumor and stromal cells, promoting the recruitment and proliferation of endothelial cells and pericytes for angiogenesis [117]. VEGF-A expression under hypoxia also mediates the recruitment of tumor-associated macrophages (TAMs), a key cellular component in the metastatic niche that impacts tumor progression [118]. It has been suggested that macrophages are functionally plastic cells such that they can switch between anti-tumorigenic and pro-tumorigenic functions depending on the microenvironment. TAMs were found to be recruited to hypoxic areas of growing tumors and to promote tumor angiogenesis,

suggesting that hypoxia may regulate the transition of TAM function in a metastatic niche [119,120].

Despite its emerging importance, it has been challenging to study the detailed mechanisms behind how hypoxia in the metastatic niche dictates the fate of DTCs in concert with other niche factors due to the lack of appropriate experimental models. It is difficult to locate natural metastatic niches *in vivo*, as the small number of DTCs present in the metastatic niche at early stages is typically below the detection limit of traditional imaging techniques [121–123]. In addition, it is not always feasible to access regions with specific microenvironments such as hypoxia, further impeding translational studies to identify therapeutic interventions [112]. To overcome these issues, synthetic metastatic niches have recently been established using biomaterial scaffolds to generate experimentally accessible *in vivo* metastatic sites [40,121,124–126], with niche-mimicking biomaterials offering many advantages compared to other strategies for studying *in vivo* metastatic niches [121]. In one such approach utilizing microporous poly(lactide-co-glycolide) (PLG) scaffolds to recruit metastasizing breast cancer cells, it was found that the local foreign body response to the implanted scaffolds established an inflammatory cell distribution similar to that of metastatic organs such as the lung and liver, recapitulating the unique immune microenvironment of pre-metastatic niche. These immune cells that accumulated at implanted PLG scaffolds secreted various factors that facilitated the subsequent recruitment of DTCs to the scaffold [40,127]. More importantly, cellular and molecular niche factors such as immune cells, exosomes, and soluble factors can be incorporated to further tune the synthetic metastatic niche to reflect cancer or organ-specific microenvironments [121].

Other biomaterial-based strategies such as hydrogels [128], bioactive glass [129] or gelatin nanofibrous scaffolds [130] have been employed to mimic hypoxic niches *in vivo* for tissue engineering applications. However, to our knowledge, none of these approaches have been demonstrated to facilitate recruitment of tumor cells. Thus, we aimed to develop a method for establishing an *in vivo* hypoxic metastatic niche which is implantable in a readily accessible region, such as beneath the skin, enabling future investigation of hypoxic regulation within the metastatic niche in determining the fate of DTCs. In this report, we hypothesized that incorporation of a hypoxia-mimetic agent into a metastatic niche-mimicking biomaterial scaffold could enable generation of an *in vivo* hypoxic metastatic niche. To test this hypothesis, $CoCl_2$, a hypoxia-mimetic agent, was incorporated into microporous PLG scaffolds. The hypoxia-mimicking effects of $CoCl_2$ have been validated in a number of previous studies in tissue engineering and cancer biology[131,132], which demonstrated its ability to recapitulate hypoxic regulation of downstream targets such as glucose transporters[133], erythropoietin[71] and VEGF[134]. $CoCl_2$ is known to mimic hypoxia through the stabilization of the HIF1α transcription factor, a master regulator of cellular and molecular responses to hypoxia, even in the presence of oxygen[135]. Thus, the hypoxia-mimicking effects of $CoCl_2$ are stable compared to that of oxygen-depleting or scavenging approaches.

In this study, we evaluated the ability of $CoCl_2$-containing PLG (Co-PLG) scaffolds to establish hypoxic niches *in vivo* and recruit metastasizing tumor cells. Hypoxia-mimicking effects of Co-PLG scaffolds were demonstrated through *in vitro* and *in vivo* characterization of signature hypoxic responses including angiogenesis and stabilized HIF1α expression. *In vivo* metastatic niche-mimicking effects of Co-PLG scaffolds were validated in the 4T1 mouse breast cancer metastasis model to demonstrate that the addition

of $CoCl_2$ did not negatively affect the ability of the PLG scaffold to recruit metastatic tumor cells. This engineered scaffold provides a versatile tool for detailed investigation of the hypoxic metastatic niche at target organs, which could facilitate studies of how hypoxia affects the fate of DTCs upon arrival at a distal site.

3.2. Materials and methods

Scaffold fabrication. To fabricate Co-PLG and PLG scaffolds, microspheres were fabricated using an established method[136]. 2% (w/w) and 6% (w/w) solutions of PLG (Lakeshore Biomaterials; 75:25 lactide:glycolide, inherent viscosity = 0.76 dL/g) in dichloromethane (DCM) were emulsified in 1% poly(vinyl alcohol) (PVA), followed by centrifugation and four washes in deionized water. Then, 80 mg of the PLG particles was resuspended in 5 ml of deionized water (PLG) or aqueous $CoCl_2$ solution containing 5 mg (5-Co-PLG) or 15 mg (15-Co-PLG) of $CoCl_2$ and flash-frozen in liquid nitrogen, followed by lyophilization for 48 hours. For the double emulsion (water-in-oil-in-water) method, 200 µl of aqueous $CoCl_2$ solution containing 5 mg of $CoCl_2$ was mixed with 80 mg of PLG in 3ml DCM. Then, the mixture was sonicated at 40 watts for 15 seconds on ice to form a primary emulsion. The primary emulsion was mixed with 25 ml of 5% (w/v) PVA aqueous solution and homogenized at 7000 rpm for 45 seconds to form a secondary emulsion. The homogenized solution was added to 50 ml of 1% PVA aqueous solution and stirred for 2 hours to evaporate the DCM. The resulting microspheres were frozen in liquid nitrogen and lyophilized for 48 hours. For fabrication of the inner disk, 2 mg of Co-PLG microspheres was pressed into a 3mm disk using a hand press (Pike Technologies) and dip-coated in 2% (w/w) PLG solution in DCM. For the outer microporous layer, 6% (w/w)

PLG microspheres were mixed at a 1:30 ratio with 250 - 420 μm sodium chloride particles. Next, the inner disk was placed in the center of the outer layers and the mixture was pressed at 1500 psi using a 5-mm diameter steel die (Specac). The resulting scaffolds were gas-foamed and sodium chloride particles were leached out in water for 90 min. Scaffolds were rinsed with water and sterilized in 70% (v/v) ethanol for 1 minute before surgical implantation.

Measurement of $CoCl_2$ loading efficiency. 5 mg of $CoCl_2$ ($W_{initial}$) was added to 80 mg of PLG microspheres ($W_{PLG,before\ loading}$) via either the flash freezing or double emulsion method. The actual amount of $CoCl_2$ loaded (W_{loaded}) was calculated by measuring the increased weight of PLG microspheres after $CoCl_2$ loading ($W_{PLG,after\ loading}$), as determined after the final lyophilization step. As 10% weight loss of PLG microspheres during the fabrication process was observed even without $CoCl_2$ loading, this loss was considered in the calculation of W_{loaded}. Accordingly, the $CoCl_2$ loading efficiencies for the flash freezing and double emulsion methods were calculated using the following equations (where W indicates weight):

$$W_{loaded} = W_{PLG,after\ loading} - (W_{PLG,before\ loading} \times 0.9) \quad (1)$$

$$\%\ loading = [(W_{initial} - W_{loaded}) / W_{initial}] \times 100 \quad (2)$$

Scanning Electron Microscopy (SEM). The structure of layered Co-PLG scaffolds was imaged using a cold field emission gun scanning electron microscope (Hitachi S-4700, Hitachi High-Technologies Corp.). Scaffolds were cut in half and pre-coated with a 10 nm-

thick Pd layer using an EM ACE600 sputter coater (Leica) prior to imaging. Imaging was performed at 2kV accelerating voltage.

***In vitro* $CoCl_2$ release test.** To evaluate the release of cobalt ions, Co-PLG scaffolds were immersed in 5 ml of Dulbecco's phosphate-buffered saline (PBS) at 37 °C for 14 days. The resulting PBS solutions were collected at 1, 3, 7, and 14 days, with a complete replacement with fresh PBS at each collection. The amount of released cobalt ions was measured using inductively coupled plasma optical emission spectrometry (ICP-OES). ICP-OES was conducted using a Thermo Scientific iCAP 6000 Series ICP Spectrometer, and each condition was tested in triplicate.

Cell culture. Human umbilical vein endothelial cells (HUVECs; ATCC CRL-1730) were maintained in Endothelial Growth Medium-2 (EGM-2, Lonza) containing 2% (v/v) fetal bovine serum (FBS) and growth supplements (EGM-2 bullet kit, Lonza). The MCF-7 human breast cancer line (ATCC HTB-22) and OVCAR-3 human ovarian cancer cell line (ATCC HTB-161) were cultured as previously described[132].

***In vitro* cell viability assay.** Cell viability was evaluated using a Live/Dead Viability/Cytotoxicity Kit and an alamarBlue assay (Thermo Fisher Scientific). For the Live/Dead assay, HUVECs at 40-50% confluence were incubated with Co-PLG scaffolds for 72 hours. To evaluate the effect of $CoCl_2$ released from the scaffold on cell viability, HUVECs were grown in 2-D culture dishes, and Co-PLG scaffolds were placed in the culture media above cells. Then, cells were rinsed twice with PBS and stained as per the

manufacturer's instructions. The EVOS FL Auto fluorescence microscope (Thermo Fisher Scientific) was used for imaging. For the alamarBlue assay, after 24-hour or 72-hour incubation with Co-PLG scaffolds HUVECs were incubated with 10% alamarBlue solution for 4 hours at 37 °C. 100 µl of alamarBlue solution was collected from each well after the 4-hour incubation and analyzed using a Synergy H1 spectrophotometer (BioTek).

Immunofluorescence assays. Fixation, blocking/permeabilization and staining were performed as previously described [132]. Primary and secondary antibodies used in immunofluorescence assays are summarized in Tables 3-1 and 3-2. Images were taken with an EVOS FL Auto fluorescence microscope.

Table 3-1. Primary antibodies used for immunofluorescence assays

Target antigen	Antibody species	Vendor	Clone or product number	Dilution
HIF1α	Mouse	BD Biosciences	610098; clone 54/HIF1α,	1:200
GLUT-1	Mouse	ThermoFisher	MS-10637-P1; clone SPM498	1:200

Table 3-2. Secondary antibodies used for immunofluorescence assays

Species reactivity	Host	Conjugate	Vendor	Dilution
Mouse	Goat	Alexa Fluor 647	A21240; ThermoFisher	1:1000
Mouse	Goat	Alexa Fluor 488	A11001; ThermoFisher	1:1000

Western blotting. Protein extraction and western blotting were performed as previously described [132]. For detection of HIF1α and β-actin, 25 µg and 10 µg of whole cell lysates were used, respectively. Primary and secondary antibodies used for western blots are summarized in Tables 3-3 and 3-4.

Table 3-3. Primary antibodies used for western blotting

Target antigen	Antibody species	Vendor	Clone or product number	Dilution
HIF1α	Mouse	BD Biosciences	610098; clone 54/HIF1α,	1:1000
β-actin (HRP-conjugated)	Rabbit	Cell Signaling Technology	5125S; clone 13E5	1:1000

Table 3-4. Secondary antibodies used for western blotting

Species reactivity	Host	Conjugate	Vendor	Dilution
Mouse	Goat	Polyclonal HRP	G21040; ThermoFisher	1:6000

***In vitro* tube formation assay.** Prior to cell seeding, 24-well cell culture plates were coated with growth factor-reduced Matrigel (10.1 mg/ml, BD Bioscience) and incubated at 37 °C for 1 hour. HUVECs that had been passaged at least twice after thawing (passage 2-5) were pre-stained with calcein AM and seeded on top of the Matrigel layer at a density of 10,000 cells/cm^2. Endothelial Basal Media-2 (EBM-2, Lonza) and Endothelial Growth Medium-2 (EGM-2, Lonza) were used as a negative and positive control, respectively. HUVECs were incubated with Co-PLG scaffolds or in a hypoxia chamber (maintained at 1% O_2) for 24 hours in EBM-2. To evaluate the effect of $CoCl_2$ released from the scaffolds on tube formation ability, incubation of the HUVECs with Co-PLG scaffolds was performed by suspending the scaffolds in the culture media above the HUVECs. True hypoxia (1% O_2) was achieved by controlling gas flow using a single flow meter connected to a hypoxia chamber (STEMCELL Technologies). For studies with the hypoxia chamber, to minimize effects from reoxygenation, imaging was performed immediately after HUVECs were removed from the chamber. Images were taken at the timepoint at which peak levels of

tube formation were observed (8-12 hours post-seeding) using an EVOS FL Auto fluorescence microscope. Quantification was performed with ImageJ software.

***In vivo* studies.** Animal studies were conducted in accordance with and approved by the University of Minnesota Institutional Animal Care and Use Committee (IACUC). BALB/c mice (The Jackson Laboratory) received two scaffolds in the upper dorsal subcutaneous space. The implanted scaffolds were retrieved 2 weeks post-implantation for further characterization. To evaluate tumor cell recruitment, 2×10^6 4T1 breast cancer cells in 50 μL PBS were injected into the right mammary pad of 8-week-old female BALB/c mice. Tumor-free mice were injected with 50 μL PBS as a negative control. Tumor width and length were measured weekly using digital calipers and tumor volume was calculated using the formula [137] Volume = $(\text{Width}^2 \times \text{Length})/2$. PLG and Co-PLG scaffolds were implanted into the subcutaneous region of the mice 7 days post-tumor inoculation. The implanted scaffolds were retrieved 14 days after scaffold implantation and immediately frozen in liquid nitrogen and stored at −80 °C.

Quantitative real-time PCR (qRT-PCR). Tumor metastasis to the scaffold was quantified by qRT-PCR using a previously described assay [138]. Briefly, homogenization of scaffolds was performed at 10,000 rpm on ice for 20 seconds in RLT cell lysis buffer (Qiagen) containing 1% 2-mercaptoethanol (Sigma-Aldrich). Total RNA extraction, cDNA synthesis, and qRT-PCR were performed as previously described[132]. Primers for *MT2* (Forward sequence: GCCTGCAAATGCAAACAATGC, Reverse sequence: AGCTGCACTTGTCGGAAGC, PrimerBank) and *GAPDH* (Forward sequence:

CAATGTGTCCGTCGTGGA, Reverse sequence: GATGCCTGCTTCACCACC, PrimerBank) were used. Gene expression of HUVECs in response to Co-PLG scaffolds was also assessed using the PrimePCR SYBR Green Assays (Bio-Rad) summarized in Table 3-5. Fold change in gene expression was calculated using following equations, where CT indicates the threshold cycle number:

$$\Delta CT = CT\ (\text{target gene}) - CT\ (\text{reference gene}) \quad (3)$$

$$\Delta\Delta CT = \Delta CT(\text{treated sample}) - \Delta CT(\text{control sample}) \quad (4)$$

$$\text{Fold change} = 2^{-\Delta\Delta CT} \quad (5)$$

Table 3-5. Primers used for qRT-PCR

Gene	Vendor	ID Number
VEGFA	BioRad	qHsaCED0006937
FLT1	BioRad	qHsaCID0010190
KDR	BioRad	qHsaCID0006310
ANGPT1	BioRad	qHsaCID0008671
ANGPT2	BioRad	qHsaCID0017615
ACTB	BioRad	qHsaCED0036269

Histological analysis and immunohistochemistry (IHC). Retrieved organs and scaffolds were immediately fixed in 4% paraformaldehyde for 48 hours and transferred to 70% ethanol. The fixed tissues were paraffin-embedded and sliced at 4 μm thickness with an HM 315 microtome (Microm). Hematoxylin and eosin (H&E) or terminal deoxynucleotidyl transferase dUTP nick end labeling (TUNEL) staining was performed to evaluate the biocompatibility of implanted scaffolds. Histopathological examination of H&E stained sections was performed through blinded analysis by a pathologist. For the quantification, 10 areas at 40x magnification were examined in each scaffold, and 3 or more scaffolds were evaluated per condition. To evaluate lungs and livers, 4 tissues per group were assessed. For immunohistochemistry, slides were blocked with Rodent Block

M (Biocare Medical) for 30 min at room temperature in a humidified chamber. Then, blocked slides were stained with polyclonal rabbit anti-HIF1α (1:50, GeneTex GTX30647), anti-CD31 (1:100, Thermo Fisher Scientific RB-10333-P1), or anti-GLUT1 (1:100, Abcam ab15309) primary antibodies overnight at 4 °C, followed by Rabbit-on-Rodent HRP Polymer (Biocare Medical RMR622G) for 30 min at room temperature. Chromogen detection was conducted using 3,3'-diaminobenzidine (DAB) chromogen concentrate and substrate buffer (Biolegend). The EVOS FL Auto fluorescence microscope was used to image the sections.

Statistical Analysis. GraphPad Prism was used for statistical analysis. All data are presented as mean ± standard deviation (SD). For *in vitro* studies, representative data shown are from one of three independent experiments. For *in vivo* results, n is specified in each figure legend. P values were calculated using an unpaired Student's t-test, and a P value less than 0.05 was considered statistically significant.

3.3. Results and discussion

3.3.1. Optimization of $CoCl_2$ loading into PLG scaffolds

Previous studies have shown that microporous PLG scaffolds implanted in mice can recruit disseminated metastatic tumor cells *in vivo* by recapitulating the local immune microenvironment of the pre-metastatic niche [40,127,136]. To develop a platform for generating a hypoxic metastatic niche, $CoCl_2$, a hypoxia mimetic agent, was incorporated into the PLG scaffolds. Two methods, flash freezing and double emulsion (water-in-oil-in-water), were initially compared for incorporation of $CoCl_2$ into PLG scaffolds (Fig. 3-1A).

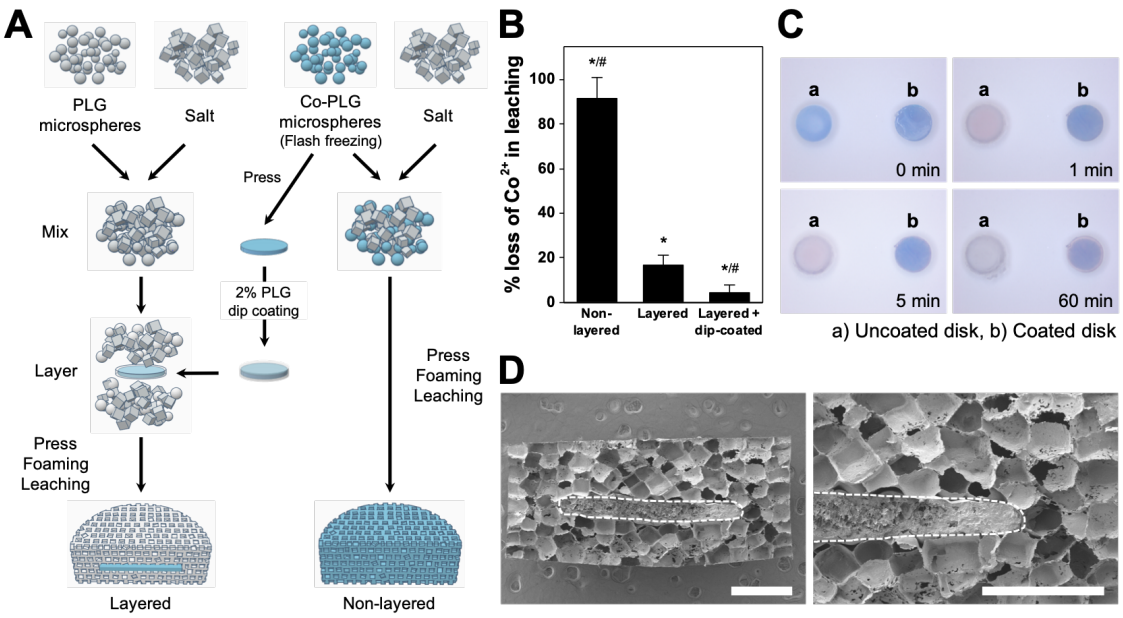

Figure 3-1. Fabrication of $CoCl_2$-containing PLG (Co-PLG) scaffolds. (A) $CoCl_2$ was incorporated into PLG microspheres using the flash freezing method, and the Co-PLG was used to fabricate layered and non-layered scaffolds. (B) The percentage of Co^{2+} loss during a 90-min leaching step as measured by ICP-OES ($^{*}P < 0.05$ compared to non-layered, $^{\#}P < 0.05$ compared to layered). (C) Evaluating the effect of dip-coating the $CoCl_2$-containing inner disk with 2% (w/w) PLG solution in DCM to introduce a protective layer that minimized the loss of $CoCl_2$ during the fabrication process. Blue color indicates that the $CoCl_2$ remains in an anhydrous state, whereas light pink color indicates that the $CoCl_2$ has become hydrated by contact with water. White color indicates that all of the $CoCl_2$ has leached out of the polymer disk. In the uncoated Co-PLG disk (a), the $CoCl_2$ within the disk is quickly hydrated, with the disk becoming white within 60 minutes of immersion in water. In contrast, the Co-PLG disk with a protective PLG coating (b) exhibits significantly reduced hydration of the $CoCl_2$ that is confined at the rim over the same time period. (D) SEM images showing a cross-sectional view of a layered Co-PLG scaffold consisting of a microporous outer PLG layer and a Co-PLG inner disk. The dashed white lines indicate the inner disk containing $CoCl_2$. Scale bars indicate 1 mm.

The loading efficiency of each method was evaluated by adding 5 mg of $CoCl_2$ to 80 mg of PLG microspheres (5-Co-PLG). It was found that 80% of the $CoCl_2$ was incorporated onto PLG microspheres by the flash freezing method, whereas less than 20% was incorporated by the double emulsion method (Table 3-6). In addition, the loading efficiency of the flash freezing method remained constant when loading higher amounts (15mg) of $CoCl_2$ onto PLG microsphere (15-Co-PLG) (Table 3-6).

Material	$CoCl_2$:PLG ratio (w:w)	% of $CoCl_2$ loaded
5-Co-PLG (DE)	1:16	19.8 ± 7.0
5-Co-PLG (FF)	1:16	81.7 ± 3.9
15-Co-PLG (FF)	3:16	79.5 ± 2.4

Table 3-6. Loading efficiency of double emulsion (DE) and flash freezing (FF) methods.

Thus, the flash freezing method was utilized to add $CoCl_2$ to PLG microspheres for the remainder of the studies. To optimize the scaffold design, layered and non-layered scaffold geometries were also tested. For layered scaffolds, Co-PLG microspheres were incorporated as a disk in between two microporous PLG layers, while for the non-layered scaffolds the porous structure was fabricated directly from the Co-PLG microspheres (Fig. 3-1A and 3-2A). As the scaffold fabrication process includes a 90-minute salt leaching step and serial washes in water, the high solubility of $CoCl_2$ in water led to significant loss of $CoCl_2$ in non-layered scaffolds during the fabrication process (Fig. 3-1B and 3-2B). In contrast, the layered scaffold was able to retain most of the loaded $CoCl_2$ during the fabrication process (Fig. 3-1B). Addition of a protective PLG coating onto the surface of the Co-PLG inner disk further reduced the loss of $CoCl_2$ during leaching in water (Fig. 3-1B, C), which is required to generate pores in the scaffold fabrication process. Most of the area within Co-PLG disks with a PLG protective coating (disk b, Fig. 3-1C) remained non-hydrated (with blue color indicative of anhydrous $CoCl_2$) after 60 minutes in water, whereas Co-PLG disks without a protective PLG coating were fully hydrated (as evidenced by pink color) within one minute (disk a, Fig. 3-1C). Without the protective coating, Co-PLG disks appeared white at the end of the 60-minute water incubation, indicating that all of the $CoCl_2$ had leached out of the disk. Thus, all further studies were performed with

layered Co-PLG scaffolds containing a PLG-coated $CoCl_2$ inner disk embedded in a microporous PLG outer layer (Fig. 3-1D).

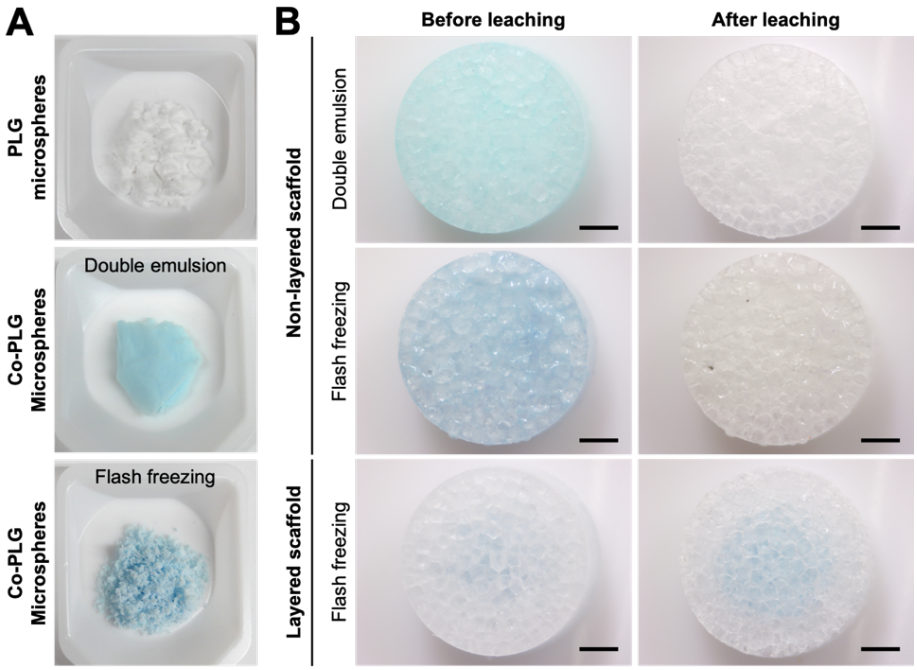

Figure 3-2. Photomicrographs of microspheres and scaffolds. (A) Images of PLG microspheres (left) and Co-PLG microspheres fabricated using double emulsion (middle) or flash freezing method (right). (B) Images of microporous scaffolds before (left column) or after (right column) 90 minutes of leaching in water for the following samples: non-layered scaffolds from the double emulsion (top row) or flash freezing (middle) method, and layered scaffolds from the flash-freezing method (bottom). Scale bars indicate 1 mm.

3.3.2. *In vitro* cobalt ion release kinetics and cytotoxicity

The release of cobalt ions (Co^{2+}) from Co-PLG scaffolds was analyzed by ICP-OES. 5-Co-PLG and 15-Co-PLG scaffolds showed sustained release of cobalt ions in PBS over 2 weeks (Fig 3-3A), with a burst release observed within first 24 hours. Importantly, the cumulative concentration of cobalt ions released from both 5-Co-PLG and 15-Co-PLG scaffolds remained within the physiologically acceptable concentration range (3-15 ppm; parts per million) [129,139]. To evaluate the toxicity of released cobalt ions, HUVECs

were incubated with Co-PLG scaffolds. No significant cell death or reduction in proliferation were observed after 72-hour incubation with 5-Co-PLG or 15-Co-PLG scaffolds (Fig. 3-3B, C). However, cumulative cobalt release eventually became toxic at a higher $CoCl_2$ loading (30 mg $CoCl_2$; 30-Co-PLG), as HUVECs incubated with 30-Co-PLG for 72 hours showed a 20% reduction in proliferation (Fig. 3-3B) and significant cell death (Fig. 3-3C). These results demonstrate that cumulative cobalt release from 5-Co-PLG and 15-Co-PLG scaffolds is within a biologically safe range.

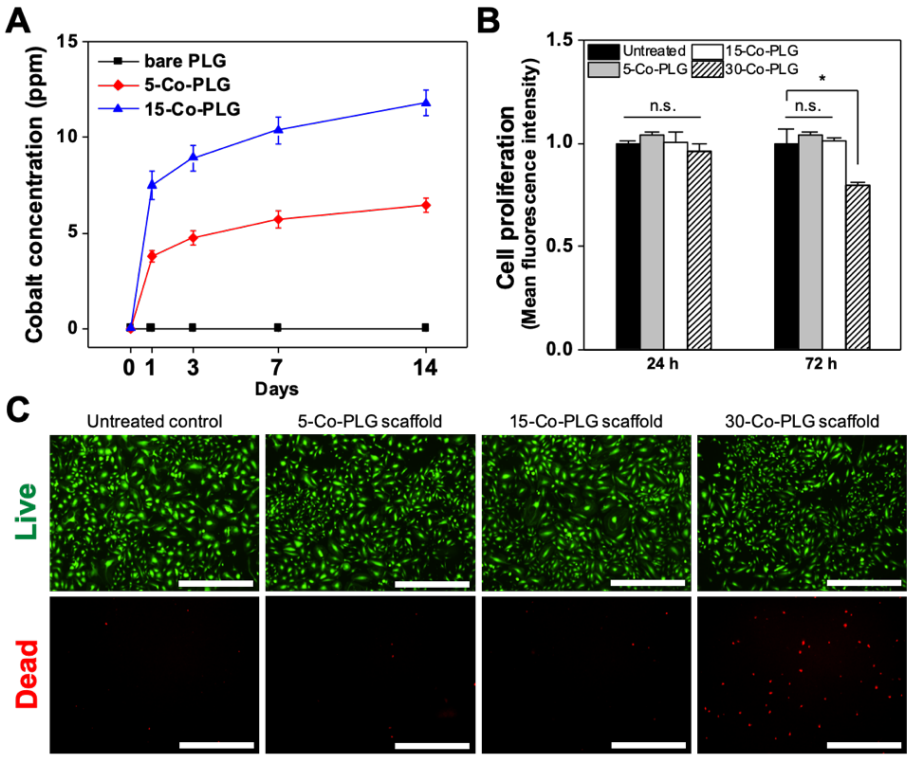

Figure 3-3. *In vitro* evaluation of release kinetics and cytotoxicity of Co-PLG scaffolds. (A) Cumulative release of Co^{2+} at day 1, 3, 7, and 14 from bare PLG, 5-Co-PLG, and 15-Co-PLG scaffolds measured using ICP-OES. (B) Proliferation of HUVECs after 72 hours of incubation with Co-PLG scaffolds with varying concentrations of $CoCl_2$ was evaluated using an alamarBlue assay. Mean fluorescence intensity was normalized to an untreated control (*$P < 0.05$ compared to untreated control). (C) Cell viability of HUVECs after 72 hours of incubation with Co-PLG scaffolds with varying concentrations of $CoCl_2$ was evaluated using a fluorescence assay in which live cells were stained with calcein AM (green) and dead cells were stained with ethidium homodimer-1 (red). Scale bars indicate 1 mm.

3.3.3. HUVECs incubated with Co-PLG scaffolds express hypoxia markers HIF1α and GLUT1

HIF signaling has been recognized as a major regulator of downstream transcriptional responses to hypoxia [140,141]. HIF is a heterodimer that consists of an oxygen-sensitive α-subunit and a constitutively expressed β-unit. Three isoforms of HIFα have been reported: HIF1α, HIF2α, and HIF3α. As HIF1α is present in all human tissues while HIF2α and HIF3α are restricted to specific tissues or cell types [142,143], HIF1α was used as an indicator of hypoxic responses in our study. In accordance with previous findings that HIF1α is stabilized and translocates to the nucleus to dimerize with HIF1β under hypoxic conditions [144], we evaluated stabilization and nuclear localization of HIF1α *in vitro* by western blotting and immunofluorescence analysis of HUVECs incubated with either Co-PLG scaffolds or 1% O_2 (positive control), as compared to untreated cells (Fig. 3-4). Western blotting of HIF1α demonstrated the stabilized HIFα expression in HUVECs incubated with 15-Co-PLG scaffolds or 1% O_2 for 24 hours compared to untreated HUVECs under normoxic conditions (Fig. 3-4A).

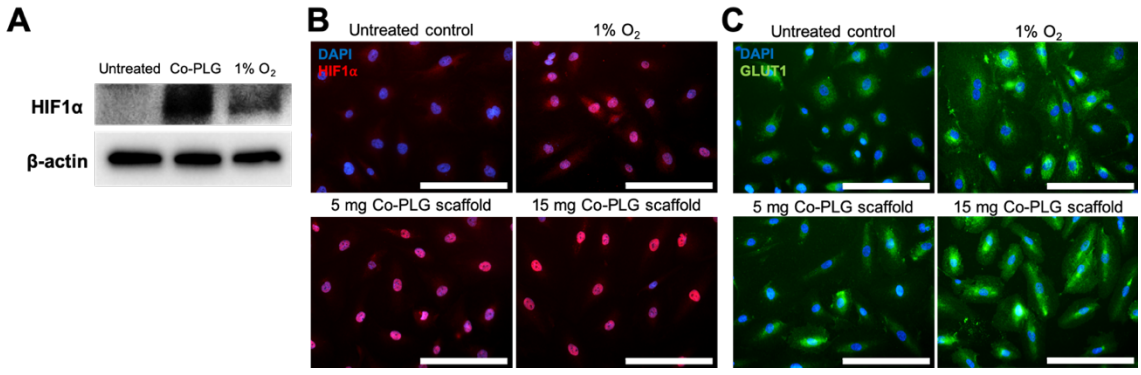

Figure 3-4. Hypoxia markers HIF1α and GLUT1 were upregulated in HUVECs cultured with Co-PLG scaffolds or 1% O_2. (A) Western blot analysis of HIF1α and β-actin (loading control) expression in HUVECs incubated with 15-Co-PLG scaffolds or 1% O_2 for 24 hours compared to untreated control. (B) Representative fluorescence images of HIF1α (red) and nuclei (blue) in HUVECs incubated with

Co-PLG scaffolds or 1% O_2 for 24 hours compared to untreated control. Scale bars indicate 200 μm. (C) Representative fluorescence images of GLUT1 (green) and nuclei (blue) in HUVECs incubated with Co-PLG scaffolds or 1% O_2 for 24 hours compared to untreated control. Scale bars indicate 200 μm.

Untreated HUVECs under normoxic conditions exhibited faint HIF1α expression spread throughout the cytoplasm (Fig. 3-4B). In contrast, HUVECs incubated with Co-PLG scaffolds or 1% O_2 for 24 hours showed strong HIF1α expression localized in the nucleus. In addition to HIF1α, the expression of glucose transporter 1 (GLUT1) was also examined as glucose transporters including GLUT1 are known to be upregulated under hypoxia to mediate metabolic adaptation of cells to hypoxic conditions [145]. HUVECs cultured with Co-PLG scaffolds or 1% O_2 also exhibited increased GLUT1 expression (Fig. 3-4C). To validate hypoxia-mimicking effects of Co-PLG scaffolds in other cellular components of metastatic niche, human cancer cells were also tested. Overall, *in vitro* hypoxia-mimicking effects, as evaluated by HIF1α and GLUT1 expression, were more pronounced in 15-Co-PLG scaffolds than in 5-Co-PLG scaffolds with no significant difference in cytotoxicity, and thus 15-Co-PLG scaffolds were used for the remaining studies.

3.3.4. Co-PLG scaffolds can recapitulate *in vitro* angiogenic responses to hypoxia

Another hallmark of the response to hypoxia is enhanced angiogenesis, which is an attempt to restore homeostasis by increasing the oxygen supply to the hypoxic microenvironment [144]. As previous findings have identified that HIF is a key transcriptional regulator of angiogenic processes under hypoxia [146,147], we hypothesized that Co-PLG scaffolds activating HIF signaling would also recapitulate

angiogenic responses under true hypoxia. To evaluate the level of angiogenesis, an *in vitro* tube formation assay was performed with HUVECs. HUVECs pre-stained with calcein AM were seeded on top of a thin layer of Matrigel. EBM-2, media without serum or growth supplements, served as negative control, while EGM-2, fully supplemented with 2% serum and pro-angiogenic growth factors, served as positive control in this assay. HUVECs cultured in EBM-2 exhibited low levels of angiogenesis, whereas HUVECs cultured in EGM-2 showed well-structured tube networks at 8-12 hours post-seeding under normoxic conditions. HUVECs cultured in EBM-2 with 15-Co-PLG scaffolds or under hypoxic conditions (1% O_2) exhibited significantly enhanced angiogenesis that peaked at 8-12 hours post seeding compared to HUVECs cultured in EBM-2 under normoxic conditions (Fig. 3-5A). In addition, both 15-Co-PLG and hypoxic conditions exhibited comparable levels of angiogenesis as the EGM-2 positive control. The average number of complete loops and mean tube length were quantified to further evaluate the level of angiogenesis in each condition. HUVECs cultured with 15-Co-PLG scaffolds and 1% O_2 had a similar number of complete loops per image, with an average of 53 ± 6 loops with Co-PLG scaffolds and 50 ± 4 loops under 1% O_2, compared to 22 ± 6 loops in HUVECs cultured with EBM-2 under normoxic conditions (Fig. 3-5B). These values were also comparable to the 55 ± 6.2 loops observed with EGM-2 (Fig. 3-5B). Moreover, HUVECs treated with 1% O_2 or Co-PLG scaffolds also exhibited similar mean tube length, 194 ± 71 μm with Co-PLG scaffolds and 199 ± 81 μm with 1% O_2, both of which were longer compared to 167 ± 83 μm with EBM-2 under normoxic conditions (Fig. 3-5B). Expression of hypoxia-inducible angiogenic genes was also investigated in HUVECs incubated with 15-Co-PLG scaffolds or 1% O_2 for 12 hours. Angiopoietin 2 (*ANGPT2*), a hypoxia-inducible gene that is known to promote vascular remodeling and angiogenic sprouting, was significantly

upregulated in HUVECs incubated with Co-PLG scaffolds or 1% O_2 for 12 hours (Fig. 3-5C). In contrast, the expression of angiopoietin 1 (*ANGPT1*) which is antagonized by *ANGPT2* [148], was significantly downregulated in both conditions. This distinct hypoxic regulation of angiopoietins has been reported in previous studies, which showed that hypoxia increased *ANGPT2* expression in a HIF-dependent manner but decreased *ANGPT1* expression due to antagonistic effects [149,150]. We also examined the expression of vascular endothelial growth factor A (*VEGFA*) and its binding receptors VEGFR1 (*FLT1*) and VEFGR2 (*KDR*), all of which are also mediated by hypoxia. *VEGFA*, known as the most potent contributor to the formation of new blood vessels and growth of pre-existing blood vessels[134,149], was also significantly upregulated in HUVECs cultured with Co-PLG scaffolds or 1% O_2 (Fig. 3-5C). While its receptor *VEGFR2* was upregulated in HUVECs cultured with Co-PLG scaffolds or 1% O_2, expression of *VEGFR1* remained unchanged in both conditions (Fig. 3-5C). This differential regulation of *VEGFA* receptors in HUVECs was also in agreement with previous findings[151]. Given that pro-angiogenic genes *ANGPT2* and *VEGFA* have previously shown concurrent upregulation during angiogenesis [149,152], the upregulation of both genes in HUVECs incubated with Co-PLG scaffolds or 1% O_2 likely led to the enhanced angiogenesis observed in these conditions. These parameters collectively suggest that Co-PLG scaffolds can recapitulate enhanced *in vitro* angiogenic responses under hypoxia.

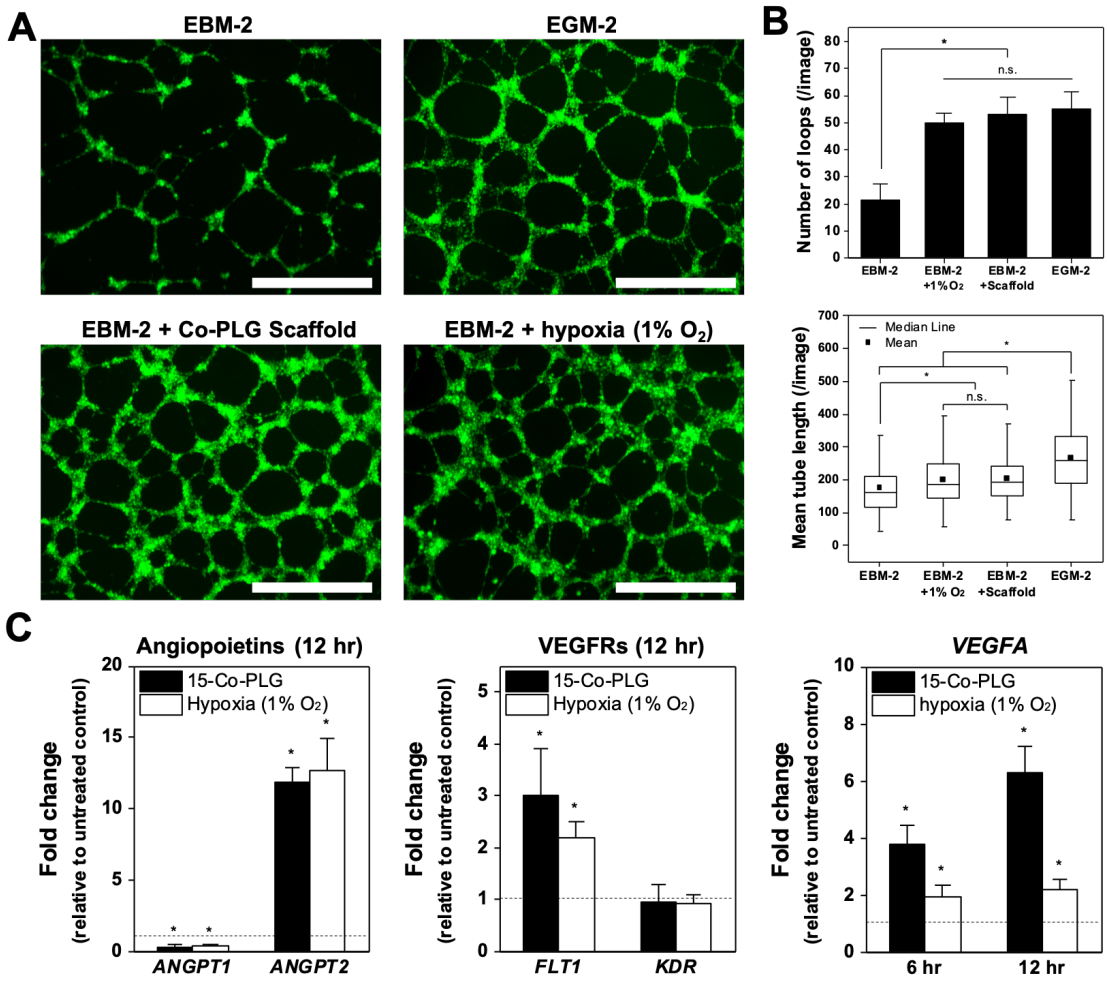

Figure 3-5. Co-PLG scaffolds recapitulate angiogenic responses to hypoxia in HUVECs. (A) Representative fluorescence images of tube networks formed by HUVECs 8 hours after seeding onto Matrigel under each condition: EBM-2 (negative control), EBM-2 with 15-Co-PLG scaffold, EBM-2 with 1% O_2, and EGM-2 (positive control). HUVECs were pre-stained with calcein AM (green) for 30 min prior to the seeding. Scale bars indicate 1 mm. (B) The average number of complete loops and tube length were quantified using ImageJ software ($^*P < 0.05$ compared to EBM-2). (C) HUVECs incubated with Co-PLG scaffolds or 1% O_2 exhibited similar angiogenic gene expression profiles. Fold change in mRNA expression of angiogenesis-related genes *VEGFA*, *FLT1*, *KDR*, *ANGPT1*, and *ANGPT2* relative to the untreated control (cultured under normoxia) was measured by qRT-PCR ($^*P < 0.05$ compared to untreated control).

3.3.5. *In vivo* biocompatibility of Co-PLG scaffolds

Prior to the evaluation of *in vivo* hypoxia-mimicking effects of Co-PLG scaffolds, we first examined *in vivo* biocompatibility of Co-PLG scaffolds, as released cobalt ions

from the scaffolds could be toxic in the body. To this end, two 15-Co-PLG scaffolds were implanted into the subcutaneous region of a BALB/c mouse and retrieved two weeks post-implantation, as this enables sufficient time for the scaffolds to integrate with host tissues, and the *in vitro* studies showed sustained $CoCl_2$ release at least for 2 weeks (Fig. 3-3A). *In vivo* biocompatibility of Co-PLG scaffolds was examined by H&E and TUNEL staining of tissue sections, using PLG scaffolds as a control (Fig. 3-6). H&E stained sections of PLG and Co-PLG scaffolds showed that both types of scaffolds were infiltrated by host cells and integrated with host tissues (Fig. 3-6A), with similar total numbers of cells infiltrating the scaffolds (Fig. 3-6B, left). Histopathological analysis revealed that cellular components within the PLG and Co-PLG scaffolds were similar, containing fibroblasts, endothelial cells, and inflammatory immune cells including multinucleated giant cells, neutrophils, lymphocytes, and macrophages. The average number of multinucleated cells was quantified, as this population is indicative of a typical foreign body response to polymeric biomaterials in the body [153], and no statistically significant difference was observed between PLG and Co-PLG scaffolds, with an average of 8.9 ± 0.4 multinucleated giant cells per imaged area in PLG scaffolds, compared with 10 ± 1.8 multinucleated giant cells per area in Co-PLG scaffolds (Fig. 3-6B, middle). Vascular density, as evaluated by the number of blood vessels per imaged area, was higher within Co-PLG scaffolds compared with PLG scaffolds (Fig. 3-6B, right). Other organs such as the liver and kidney, where toxins accumulate in the body, were also examined to investigate potential systemic effects of released $CoCl_2$ using H&E staining. H&E stained liver and kidney sections from the mice that received normal PLG and Co-PLG scaffolds showed no significant structural or morphological changes such as inflammation, fibrosis, blood vessel formation or necrotic regions (Fig. 3-6A) upon histopathological examination.

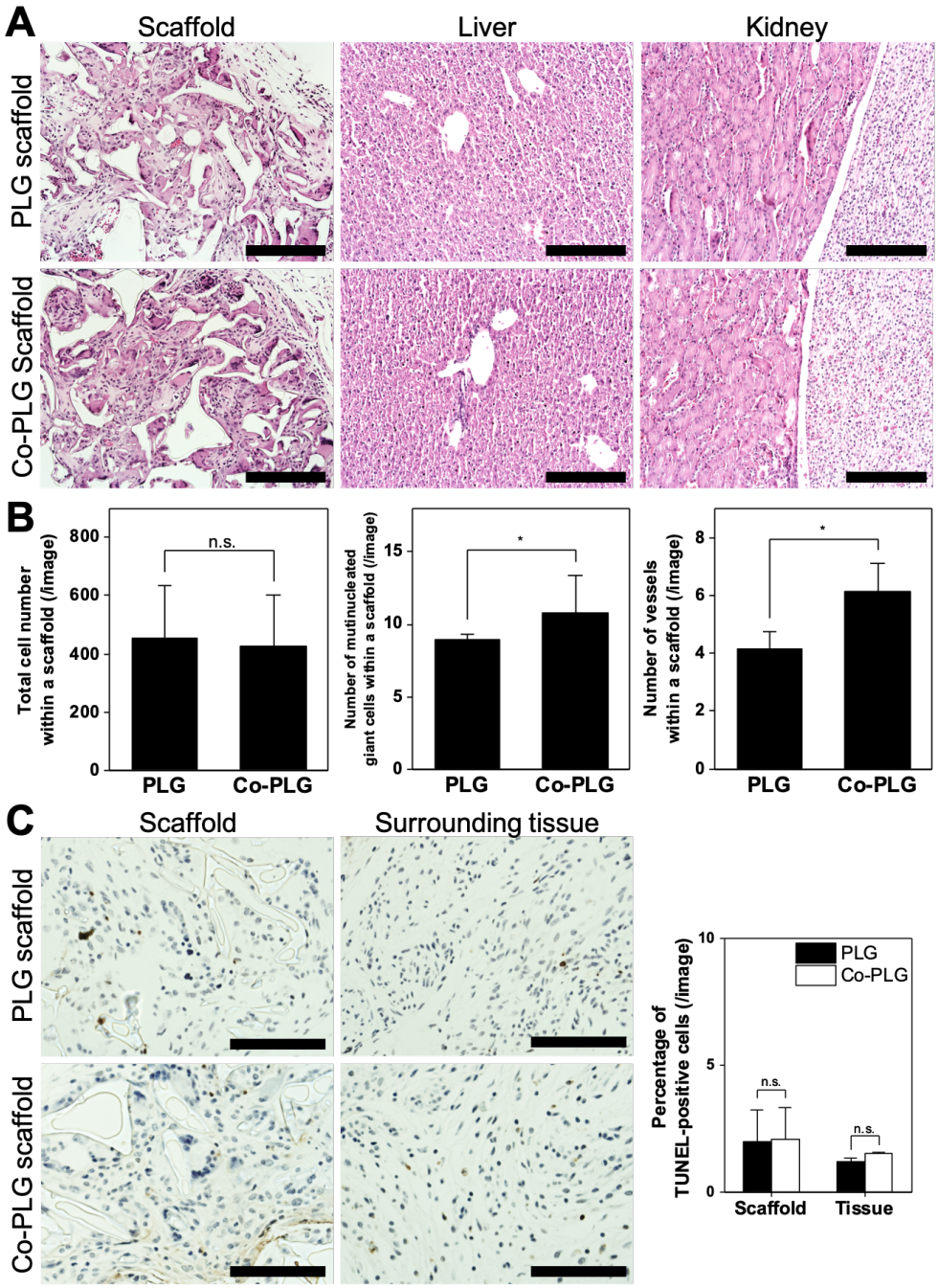

Figure 3-6. Histological analysis of Co-PLG scaffolds to evaluate *in vivo* biocompatibility. Tissue-laden scaffolds were harvested 2 weeks after implantation. (A) H&E-stained sections of scaffold, liver and kidney from the mice that received normal PLG scaffolds (top) or Co-PLG scaffolds (bottom). Scale bars indicate 200 μm. (B) Quantification of H&E stained sections of scaffolds (n ≥ 3 scaffolds per group): total cell number (left), number of multinucleated giant cells (middle), and number of blood vessels (right) per imaged area within a scaffold. ($^{*}P < 0.05$ compared to PLG scaffolds). (C) TUNEL-stained sections of scaffolds and surrounding tissue from the mice that received normal PLG or Co-PLG scaffolds (n ≥ 3 scaffolds per group). Quantification was performed with ImageJ software. Scale bars indicate 100 μm.

Thus, these results collectively suggest that released $CoCl_2$ affects the local tissue environment but does not lead to significant remodeling of distal tissues. In addition, TUNEL staining, which selectively detects apoptotic cells, showed no signs of significant apoptosis within PLG or Co-PLG scaffolds or the surrounding tissue, with less than 4% apoptotic cell populations present at all locations evaluated (Fig. 3-6C), suggesting no differences in biocompatibility between PLG and Co-PLG scaffolds.

3.3.6. Co-PLG scaffolds can establish *in vivo* hypoxic microenvironments

Biomaterial-based strategies to induce *in vivo* hypoxia have been developed to stimulate the vascularization of implanted materials for tissue engineering applications, as the lack of vascularization leads to insufficient integration with host due to the development of necrotic regions [129]. For example, an oxygen-depleting hydrogel which consumes oxygen during gel formation was shown to promote vascularization *in vivo*, as evidenced by the larger number and size of blood vessels surrounding and penetrating the hydrogel as compared to a non-hypoxic hydrogel [128]. Porous scaffolds releasing a hypoxia-mimetic agents such as $CoCl_2$ [129,131] and desferoxamine (DFO) [154,155] have been also reported. DFO-releasing gelatin nanofibrous scaffolds stimulated *in vivo* bone regeneration through enhanced angiogenesis [154]. $CoCl_2$-releasing scaffolds made of bioactive glass were not tested *in vivo* but were shown to promote *in vitro* angiogenesis [129]. In our study, we hypothesized that sustained release of $CoCl_2$ from Co-PLG scaffolds could establish an *in vivo* hypoxic microenvironment within the metastatic niche conditioned by the microporous PLG scaffold. To evaluate *in vivo* hypoxic responses within Co-PLG scaffolds, histological analysis of HIF1α, endothelial marker CD31, and

GLUT1 were conducted. Immunohistochemistry staining of HIF1α revealed that HIF1α was stabilized and localized in the nuclei of cells infiltrating the Co-PLG scaffolds, whereas most cells in normal PLG scaffolds did not exhibit positive expression and nuclear localization (Fig 3-7A). Furthermore, immunohistochemical analysis of CD31 revealed that more blood vessels had formed within Co-PLG scaffolds compared to normal PLG scaffolds by two weeks post-implantation, with an average of 69 ± 14 blood vessels per section observed in Co-PLG scaffolds compared to 27 ± 11 per section in normal PLG scaffolds (Fig. 3-7B, C). In addition, the average diameter of blood vessels within Co-PLG scaffolds was larger, with an average diameter of 24.4 ± 9.5 μm within Co-PLG scaffolds, compared to 12.7 ± 4.5 μm within PLG scaffolds (Fig. 3-7B, C). These results demonstrate that the hypoxic microenvironment within Co-PLG scaffolds promoted the formation and growth of blood vessels. Histological analysis of GLUT1 revealed that GLUT1 was also upregulated in the Co-PLG scaffolds compared to PLG scaffolds (Fig. 3-7D). These results collectively suggest that implanted Co-PLG scaffolds can establish an *in vivo* hypoxic microenvironment within the scaffold. Considering the significance of inducing *in vivo* hypoxic microenvironments in regenerative medicine as well as cancer research, Co-PLG scaffolds have the potential to be applicable to a broad range of biomedical applications.

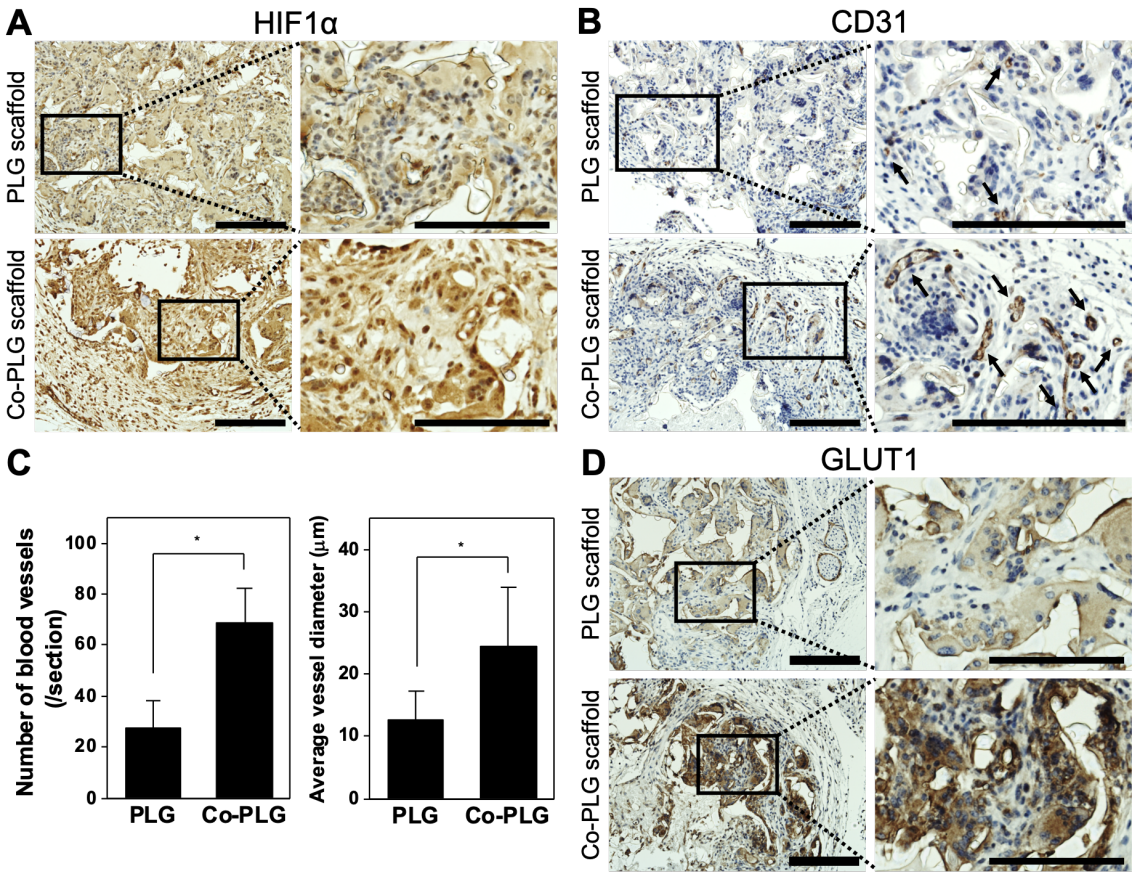

Figure 3-7. Histological analysis of HIF1α, CD31, and GLUT1 demonstrate hypoxic responses within Co-PLG scaffolds compared to normal PLG scaffolds. (A,B) Representative IHC images of HIF1α (A) or CD31 (B) expression, with zoomed-in images of boxed regions shown on the right. (C) The average number of blood vessels and vessel diameter per section were quantified with ImageJ software (n = 4 scaffolds per group; $^{*}P < 0.05$ compared to PLG scaffolds). (D) Representative IHC images of GLUT1 expression, with higher magnification images of boxed regions shown on the right. All scale bars indicate 200 μm.

3.3.7. Co-PLG scaffolds can recruit metastatic tumor cells *in vivo*.

Although an increasing number of studies have reported *in vitro* and *in vivo* hypoxia-mimicking materials for applications such as bone regeneration and wound healing, an *in vivo* platform that is able to establish a hypoxic metastatic niche has not yet been reported. As microporous PLG scaffolds have been previously used to capture metastatic tumor cells [40] and can be readily combined with other niche elements such as

soluble factors [136], we hypothesized that the engineered Co-PLG scaffold could still capture metastatic tumor cells even with the addition of $CoCl_2$. To determine whether Co-PLG scaffolds can still serve as a metastatic niche that captures disseminating tumor cells, we examined tumor cell recruitment to Co-PLG scaffolds. The number of metastatic breast cancer cells recruited to this type of polymer scaffold is low, which makes quantification of metastasis through histological analysis challenging [127,136]. Thus, we employed a previously established qRT-PCR-based assay for tumor cell quantification in the 4T1 breast cancer metastasis model [138]. The prior work found that the expression of *MT2*, which is highly expressed in 4T1 breast tumors [156], was significantly higher in scaffolds from tumor-bearing mice compared to the scaffolds from tumor-free mice, indicating that the recruitment of 4T1 cells to the scaffolds could be detected by qRT-PCR-based analysis of *MT2*[138]. Therefore, we examined *MT2* expression in Co-PLG scaffolds to evaluate tumor cell recruitment, with normal PLG scaffolds serving as a positive control (Fig. 3-8A). To generate a 4T1 primary tumor, 2 million 4T1 metastatic breast cancer cells were orthotopically injected into the right mammary pad of the mice prior to scaffold implantation, with PBS injections performed as negative control. Two 15-Co-PLG or bare PLG scaffolds were implanted into the subcutaneous region of the mice at 7 days post-tumor inoculation. The primary tumors became visible and palpable in all mice at 7-14 days post-tumor inoculation and continuously grew until removal of the implanted scaffolds. The implanted scaffolds were retrieved 14 days after implantation for qRT-PCR analysis. Our results showed that both Co-PLG and normal PLG scaffolds from the tumor-bearing mice exhibited significantly higher *MT2* expression compared to scaffolds from the tumor-free mice, indicating that both Co-PLG and PLG scaffolds recruited 4T1 metastatic breast cancer cells (Fig. 3-8B). Furthermore, *MT2* expression in Co-PLG

scaffolds was similar to that in PLG scaffolds, suggesting that the addition of $CoCl_2$ to PLG scaffolds did not negatively affect the ability of PLG scaffolds to recruit metastatic tumor cells. Given that the microenvironment within the Co-PLG scaffolds was still hypoxic at the time tumor cells were recruited into the scaffolds (day 14 post scaffold implantation, Fig. 3-7), these results suggest that Co-PLG scaffolds can serve as *in vivo* hypoxic metastatic niche.

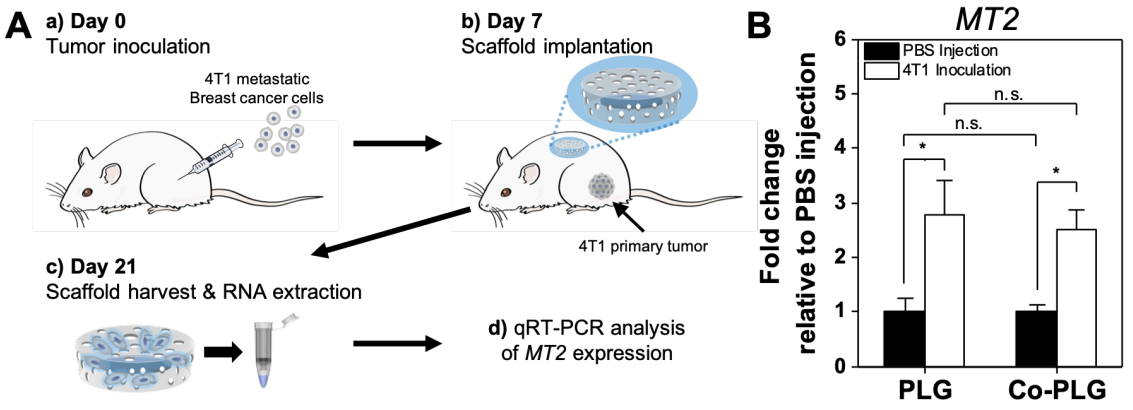

Figure 3-8. Co-PLG scaffolds can recruit 4T1 metastatic breast cancer cells. (A) Schematic of mouse metastasis model for assessment of *in vivo* tumor cell recruitment: a) Tumor inoculation at day 0, b) Scaffold implantation at day 7, c) Scaffold harvest and RNA extraction at day 21, and d) qRT-PCR analysis of *MT2* expression. (B) qRT-PCR analysis of *MT2* expression to evaluate *in vivo* tumor cell recruitment into the implanted scaffolds ($n \geq 4$ scaffolds per group). Fold change in mRNA expression of *MT2* relative to scaffolds from mice receiving PBS injection instead of tumor inoculation (negative control) by qRT-PCR ($^{*}P < 0.05$ compared to PBS control).

Subcutaneous sites were chosen in this study for their accessibility and amenability to non-invasive imaging, which can be combined with Co-PLG scaffolds in the future. While subcutaneous implantation does not recapitulate all cellular elements of the native metastatic niche, previous studies have demonstrated that subcutaneously implanted scaffolds can recapitulate the immune cell populations present in the metastatic niche [127]. Given that these scaffolds can be readily combined with other niche-specific elements such as extracellular matrix components, niche-specific cells, and soluble factors to better mimic

desired features of natural metastatic niches [40,136,157], Co-PLG scaffolds can provide a versatile, experimentally accessible platform in the subcutaneous region that enables investigation of how hypoxia in the metastatic niche regulates DTCs in concert with other niche factors.

3.4. Conclusion

As a growing body of studies have suggested, hypoxia in metastatic niches regulates cues directing the fate of DTCs that reside in the niche. Despite its emerging clinical importance, detection of hypoxic metastatic niches in target organs with current imaging techniques has been challenging due to their often inaccessible and unpredictable locations. Consequently, hypotheses related to dormancy, proliferation, and metabolic adaptation of DTCs in hypoxic niche at target organs have not been fully examined. Thus, appropriate *in vivo* experimental platforms that enable the detailed investigation of hypoxic regulation in metastatic niches are needed. In this work, PLG scaffolds that have previously been used as an *in vivo* metastatic niche were engineered to establish a hypoxic microenvironment via the addition of $CoCl_2$. We demonstrated that Co-PLG scaffolds combining the hypoxia-mimicking ability of $CoCl_2$ and tumor cell-recruiting ability of microporous PLG scaffolds can generate an experimentally accessible *in vivo* hypoxic metastatic niche in an area beneath the skin, enabling the examination of hypotheses that were untestable using previous approaches.

Chapter 4 – Sonosensitizer-functionalized graphene nanoribbon for adhesion blocking and sonodynamic ablation of ovarian cancer spheroids.

4.1. Introduction

Development of therapeutic strategies that reduce metastatic spread of cancer spheroids in peritoneal cavity has been a key issue in ovarian cancer treatment. Ovarian cancer spheroids disseminated from the primary tumor are transported throughout the peritoneal cavity by ascites fluid and eventually adhere to the peritoneal organs covered by mesothelial layer [158–160]. This unique mode of ovarian cancer metastasis allows for many metastases to develop simultaneously within the peritoneal cavity, rendering the disease untreatable with standard treatments such as debulking surgery or chemotherapy. One alternative therapeutic strategy has been used to disrupt integrin-mediated interactions with ECM proteins on mesothelial layer that mediate mesothelial adhesion of ovarian cancer spheroids [46]. For example, monoclonal antibody against integrin β1 subunits significantly blocked mesothelial adhesion of ovarian cancer spheroids *in vitro* [46,161] and *in vivo* [49]. Despite their potential in preclinical studies, none of integrin blocking approaches have demonstrated clinical benefit thus far [49–51], indicating that inhibition of a single type of integrin is not sufficient to prevent metastatic spread of ovarian cancer or that non-integrin associated pathways are also involved [46,158]. Thus, a novel therapeutic strategy to reduce the seeding of ovarian cancer spheroids throughout the peritoneal cavity is needed.

Graphene-based materials including graphene oxide (GO) and graphene nanoribbon (GNR) have shown potential in biomedical applications including cancer therapy due to their unique physical and chemical properties [56,162,163]. For example,

the presence of various functional groups (e.g. hydroxyl, epoxyl, and carboxyl groups) in their chemical structure allows for additional functionalization to ensure high solubility and stability in physiological solutions and to facilitate drug and biomolecule loading [164,165]. Furthermore, these functional groups in a polyaromatic domain of graphene-based materials can adsorb ECM proteins through hydrophobic interactions, electrostatic forces, and hydrogen bonding [166], enabling cell adhesion to graphene-based materials. Previous studies found that adhesion of mesenchymal stem cells to graphene-based materials involve surface adhesion receptors implicated in mesothelial adhesion of ovarian cancer spheroids such as integrin β1 [167,168]. While graphene-based materials have not been previously shown to associate with ovarian cancer spheroids, these previous findings suggest that graphene-based materials can be used to target integrin receptors on the ovarian cancer spheroids.

The hydrophobic polyaromatic domain of graphene-based materials can also provide exceptionally high loading capacity of aromatic drug molecules via pi-pi stacking [169,170], making these materials a versatile carrier for a wide variety of chemotherapeutic drugs [164,170,171]. Recently, graphene-based materials have also been integrated with sensitizing agents that generate cytotoxic effects upon external triggers such as light or ultrasound for tumor-specific treatment [56,172]. Graphene-based materials have widely been employed as a carrier for photosensitizers in photodynamic therapy (PDT) but low penetration depth of light limits its efficacy for deep-seated tumors [56,173,174]. As compared to conventional PDT, sonodynamic therapy (SDT) using ultrasound and a sonosensitizer has shown better therapeutic potential with high tissue-penetrating ability when combined with graphene-based materials [172,175]. For instance, graphene nanosheets loaded with a sonosensitizer significantly enhanced the efficacy of SDT [172].

Thus, we hypothesized that targeting metastatic ovarian cancer spheroids with sonosensitizer-loaded graphene-based materials could block the mesothelial adhesion of the spheroids as well as kill the spheroids via targeted delivery of sonosensitizers coupled with ultrasound irradiation.

In this work, two graphene-based materials, GO, a single or few-layered two-dimensional carbon sheet, and GNR, narrow strips of unzipped multi wall carbon nanotubes (CNTs), were tested to target ovarian cancer spheroids in ascites. Our results demonstrated that GNR functionalized with 4-arm polyethylene glycol (GNR-PEG) exhibited better cytocompatibility to mesothelial cells and adhesion blocking effects than GO-PEG. GNR-PEG was able to disrupt mesothelial adhesion of ovarian cancer spheroids, providing sustained adhesion blocking effects compared to conventional antibody blocking approaches. In addition, GNR-PEG loaded with sonosensitizer Ce6 (GNR-PEG-Ce6) was able to kill ovarian cancer spheroids via sonodynamic therapy, which was not possible in conventional approaches that only focus on blocking spheroid adhesion. Adhesion blocking and sonodynamic effects of GNR-PEG-Ce6 were also observed in the tests with ovarian cancer spheroids derived from patient ascites fluid, providing further evidence of therapeutic potential. This approach for blocking adhesion of ovarian cancer spheroids and ablating them even once they have had adhered offers a promising therapeutic strategy to reduce metastatic spread of ovarian cancer in peritoneal cavity.

4.2. Materials and methods

Synthesis of GO/GNR. GO was synthesized via the modified Hummer's method [176]. Briefly, 2 g of graphite powder (Sigma-Aldrich 282863) was dispersed in a 98% sulfuric acid solution followed by the slow addition of 7 g of potassium permanganate ($KMnO_4$;

Sigma-Aldrich 223468) to the mixture. The mixture was incubated at 35°C for 2 h in a water bath. Next, 200 mL of DI water was slowly added to the mixture in an ice bath. Then, 10 mL of hydrogen peroxide (H_2O_2; Sigma-Aldrich H1009) was added. The resulting GO solution was filtered through a paper filter and repeatedly washed in a 10% (v/v) hydrochloric acid and deionized (DI) water solution to remove the remaining manganese impurities. The prepared GO was resuspended in DI water and lyophilized for at least 48 h. GNR was also prepared as previously described [177]. To prepare GNR, 1 g of multiwall carbon nanotubes (Hanwha Chemical CM150) was dispersed in 100 mL of 98% sulfuric acid with vigorous stirring. Then, 3.5 g of $KMnO_4$ was slowly added to the dispersion and stirred at 35°C for 15 h. 100 mL of deionized water was slowly added to this solution in an ice bath. Next, 100 mL of H_2O_2 was slowly added to the mixture to terminate the oxidation of carbon nanotubes by $KMnO_4$. To remove the acidic reaction solution, GNR was centrifuged at 15,000 rpm for 1 hour at 4°C, and precipitated GNR was washed in DI water several times. The purified GNR was resuspended in DI water and lyophilized for at least 48 h.

PEGylation of GO or GNR. For PEGylation with 4-arm PEG, GO or GNR were diluted to 1 mg/mL. 5 mg/mL of amine-terminated 4-arm PEG (average Mn = 2,000; Sigma-Aldrich JKA7032) was added to the GO or GNR solution and bath-sonicated for 5 min. Then, 5 μM of 1-ethyl-3-(3-dimethylaminopropyl)carbodiimide hydrochloride (EDC; Thermo Fisher Scientific 22980) was added to the mixture and bath-sonicated for 30 min. Additional EDC was added to mixture to the final concentration of 20μM, and the mixture was stirred overnight at room temperature. To remove unbound 4-arm PEG, the resulting GO-PEG or GNR-PEG solution was centrifuged at 15,000 rpm for 1 hour, and precipitated

GO-PEG or GNR-PEG was resuspended in sterile water at a final concentration of 1 mg/mL. PEGylation was confirmed using Fourier-transform infrared spectroscopy (FTIR). FTIR was conducted using the Nicolet 6700 FTIR spectrometer (Thermo Fisher Scientific). To evaluate stability in physiological buffers, GO-PEG or GNR-PEG were suspended in cell culture media containing 10% (v/v) fetal bovine serum (FBS; Thermo Fisher Scientific 16000044) and 1% (v/v) penicillin-streptomycin (PS; Thermo Fisher Scientific 15140122). Aggregation was monitored over 24 h after a brief sonication.

Synthesis and characterization of GNR-PEG-Ce6. Ce6 (Santa Cruz Biotechnology sc-263067) was dissolved in dimethyl sulfoxide (DMSO), followed by dilution in water to achieve the desired final concentration. For Ce6 loading onto GNR-PEG, Ce6 was added to 1 mg/ml GNR-PEG in water to the final concentration of 0.01 mg/ml and stirred overnight at room temperature. Unloaded excess Ce6 in the supernatant was removed after brief centrifugation of GNR-PEG-Ce6 followed by washing in water. This step was repeated until the green color of Ce6 in the supernatant disappeared. UV-Vis spectrometry was performed using the Evolution 220 UV-Visible spectrophotometer (Thermo Fisher Scientific) to evaluate Ce6 loading.

Cell culture. SKOV-3 human ovarian cancer cells (ATCC HTB-77) were maintained in McCoy's 5A media (Thermo Fisher Scientific 16600) supplemented with 10% (v/v) FBS and 1% (v/v) PS. LP-9 human peritoneal mesothelial cells (Coriell Institute AG07085) were maintained on flasks pre-coated with gelatin (0.1 w/v%; STEMCELL Technologies 07903) in media prepared by mixing Dulbecco's Modified Eagle Media (DMEM, Sigma-

Aldrich D6429) and Media 199 (GE Healthcare Life Science SH30253.01) in a 1:1 ratio, supplemented with 15% FBS, 10 ng/ml EGF (PeproTech AF-100-15), and 0.4 μg/ml hydrocortisone (Sigma-Aldrich).

Cancer spheroid generation on a pHEMA-coated plate. To make the poly(2-hydroxyethyl methacrylate) (pHEMA, Sigma-Aldrich P3932) solution, 1.2 g of pHEMA pellets were dissolved in 38 mL of 95% ethanol in water. The solution was stirred overnight at room temperature, then sterile-filtered using a tube top filter unit (Miliporesigma SCGP00525) and stored at 4 ℃ prior to future use. Cell culture plates were coated with pHEMA (15μL/cm^2) and dried overnight at room temperature in a biosafety cabinet. For spheroid generation, 2 million SKOV-3 cells suspended in 10 mL of maintenance media were plated on a 100 mm diameter pHEMA-coated culture dish. Patient ascites spheroids were also maintained on a pHEMA-coated culture dish in McCoy's 5A media supplemented with 10% (v/v) FBS and 1% (v/v) PS. Spheroid size, represented as an average of two perpendicular diameters, was measured using ImageJ software.

Treatment with graphene-based materials or monoclonal antibodies (mAbs). SKOV-3 spheroids had been cultured on a pHEMA-coated dish in McCoy's 5A media supplemented with 10% (v/v) FBS and 1% (v/v) PS for 24h before treated with graphene-based materials or mAbs. Graphene-based materials or mAbs were directly added to the media and incubated with SKOV-3 spheroids for 48 h. For blocking surface receptors, 100 μg/mL of antibody against each receptor was used. Monoclonal antibodies used for blocking surface receptor are listed in Table 4-1.

Table 4-1. Monoclonal antibodies for blocking surface receptors

Target antigen	Antibody species	Vendor	Clone or product number
integrin β1	Mouse	Santa Cruz Biotechnology	SC-13590L; clone P5D2
CD44	Mouse	BD	550990; clone 515
E-cadherin	Rat	ThermoFisher	16-3249-82; clone DECMA-1

Spheroid adhesion tests on ECM proteins. For adhesion tests, 96-well plates with non-tissue culture treated surfaces were coated with 50 μg/mL of collagen I (Corning 354249), collagen IV (Sigma-Aldrich C5533), or fibronectin (Sigma-Aldrich F1141) in distilled water overnight at 37 ℃ prior to spheroid plating. Spheroids were resuspended in serum-free McCoy's 5A media, and 100 μL of the suspension was added to each well of a 96-well plate, providing 50-100 spheroids per well. The total number of spheroids in each well was manually counted prior to incubation. After incubation, non-adhered spheroids were washed out and the number of remaining spheroids were counted. The percentage of adhered spheroids in each well was calculated as the number of remaining spheroids divided by the total number of spheroids before incubation.

Spheroid adhesion test on LP-9 mesothelial cell layer. LP-9 mesothelial cells were cultured on gelatin-coated 6-well plates until a confluent monolayer was formed. Then, SKOV-3 spheroids cultured for 24 h on the pHEMA-coated surface were mixed with 50 μg/mL of GNR-PEG or GNR-PEG-Ce6 in 2 mL of the LP-9 cell maintenance media and 50-100 spheroids were transferred on top of the LP-9 cell monolayer. The plates were gently rotated on the orbital shaker at 50 rpm during the test. The adhesion rate was evaluated as described above for adhesion tests on the ECM proteins.

Scanning Electron Microscopy (SEM). Spheroids were prepared for SEM imaging as previously described [178]. Briefly, spheroids were fixed in 2.5% (v/v) glutaraldehyde (Sigma-Aldrich G5882) in phosphate-buffered saline (PBS) for 60 min at room temperature, followed by cross-linking in 0.5% (w/w) osmium tetroxide (OsO_4; Acros Organics AC197450010) for 30 min at room temperature. Fixed spheroids were dehydrated with a graded ethanol series from 25% to 100% anhydrous ethanol. Then, dehydrated spheroids were resuspended in hexamethyldisilazane (HMDS, Sigma-Aldrich 440191), a chemical dehydrant, and placed on a silicon wafer for drying overnight prior to imaging. Prepared spheroids were coated with 10 nm of iridium using an EM ACE600 sputter coater (Leica). For bare or PEG-conjugated GO/GNR, 10 μL of diluted GO/GNR solution (0.05 mg/mL) was dropped onto a silicon wafer and dried in a vacuum oven at 100 ℃ for 2 h. The samples were coated with 2 nm of iridium using the EM ACE600 sputter coater. Imaging was performed at 2 kV accelerating voltage using a field emission gun scanning electron microscope (SU-8230, Hitachi).

Spheroid disaggregation and spreading assay. For the spheroid disaggregation and spreading assay, 24-well plates were coated with 50 μg/mL of collagen I, IV, or fibronectin overnight at 37 °C prior to spheroid seeding. Spheroids treated with GO-PEG or GNR-PEG for 48 hours were suspended in 10% serum-supplemented McCoy's 5A media and transferred to the ECM protein-coated plates. The spheroids that had not adhered were washed out after 2 h of incubation. The adherent spheroids were imaged at 4 and 24 h after the final washing using the EVOS FL Auto fluorescence microscope (Thermo Fisher Scientific). To evaluate the average spreading distance of adhered spheroids, the four

farthest distances between the outer boundary of spreading cell layer and the boundary of non-disaggregated center of adhered spheroids at each time point were measured using ImageJ software.

Immunofluorescence assays. Immunofluorescence staining was performed as previously described[179]. Primary and secondary antibodies used for staining are listed in Tables 4-2 and 4-3. Imaging was conducted with an EVOS FL Auto fluorescence microscope.

Table 4-2. Primary antibodies used for immunofluorescence assays

Target antigen	Antibody species	Vendor	Clone or product number	Dilution
F-actin	Phalloidin	ThermoFisher	A12379; Alexa Fluor™ 488 Phalloidin	1:200
CA125	Mouse	ThermoFisher	MA5-11579; clone Ov185:1	1:200
CK7	Mouse	ThermoFisher	MA5-11986; clone OV-TL 12/30	1:200

Table 4-3. Secondary antibodies used for immunofluorescence assays

Species reactivity	Host	Conjugate	Vendor	Dilution
Mouse	Goat	Alexa Fluor 594	A21240; ThermoFisher	1:1000
Mouse	Goat	Alexa Fluor 488	A11001; ThermoFisher	1:1000

Western blot analysis. Western blots were performed as previously described[179]. For detection of integrin α5, integrin β1, CD44, E-cadherin, and talin-1, 20 μg of whole cell lysate was used. For detection of β-actin, 10 μg of whole cell lysate was used. Primary and secondary antibodies used in Western blot analysis are listed in Tables 4-4 and 4-5.

Table 4-4. Primary antibodies used for western blotting

Target antigen	Antibody species	Vendor	Clone or product number	Dilution
integrin α5	Mouse	Cell Signaling Technology	98204; clone D7B7G	1:1000

integrin β1	Mouse	Cell Signaling Technology	34971; clone D6S1W	1:1000
E-cadherin	Rabbit	Cell Signaling Technology	3195S; clone 24E10	1:200
CD44	Mouse	BD Biosciences	550990; clone 515	1:1000
Talin 1	Rabbit	Cell Signaling Technology	4021; clone C45F1	1:1000
β-actin (HRP-conjugated)	Rabbit	Cell Signaling Technology	5125S; clone 13E5	1:1000

Table 4-5. Secondary antibodies used for western blotting

Species reactivity	Host	Conjugate	Vendor	Dilution
Mouse	Goat	HRP	G21040; ThermoFisher	1:6000
Rabbit	Goat	HRP	7074S; Cell Signaling Technology	1:2000

Cell viability test. The Live/Dead cell viability assay (Thermo Fisher Scientific L3224) and alamarBlue assay (Thermo Fisher Scientific DAL10250) were performed as previously described[179] to evaluate the toxicity of graphene-based materials to the LP-9 cell monolayer.

Mesothelial clearance test. SKOV-3 spheroids were been treated with 50 μg/mL of GNR-PEG or GNR-PEG-Ce6 for 48 h before transferred on top of a confluent LP-9 cell monolayer in 6 well plates. The LP-9 cell layer was stained with CellTracker™ Green Dye (Thermo Fisher Scientific C2925) for 30 min prior to incubation with the spheroids. The SKOV-3 spheroids were labeled with CellTracker™ Red Dye (Thermo Fisher Scientific C34552) 1 h prior to seeding on top of LP-9 cells. The clearance of LP-9 cells underneath the spheroids was monitored and imaged using an EVOS FL Auto fluorescence microscope every hour.

Ultrasound irradiation of adhered spheroids. SKOV-3 spheroids mixed with 50 μg/mL of GNR-PEG or GNR-PEG-Ce6 in 2 mL of the LP-9 cell maintenance media were

transferred on top of a confluent LP-9 cell monolayer in 6 well plates. The plates were gently rotated on the orbital shaker at 50 rpm for 48 h. After 48 h of treatment, non-adhered spheroids were removed and each well was filled with 10 mL of media for ultrasound irradiation. Since SKOV-3 spheroids completely spread out in 48 h without GNR treatment, untreated spheroids adhered to the LP-9 layer at 6 h of incubation were used as the control to achieve similar levels of adhesion and disaggregation compared to the GNR-PEG-treated or GNR-PEG-Ce6-treated spheroids. Then, ultrasound irradiation was delivered using an ultrasound unit with 4 cm^2 transducer (LG MedSupply LG-US1). The transducer was immersed in the media and 0.8 W/cm^2 of ultrasound irradiation at a frequency of 1Mhz was delivered for 30 s. The Live/Dead assay was performed 30 min after ultrasound irradiation.

ROS detection in SKOV-3 spheroids and LP-9 mesothelial cells. The generation of ROS after ultrasound irradiation was evaluated using a DCFDA (2',7'–dichlorofluorescin diacetate) - Cellular ROS Assay Kit (Abcam ab113851). As in the previous adhesion test, SKOV-3 spheroids mixed with 50 μg/mL of GNR-PEG-Ce6 were placed on top of a confluent LP-9 layer in 96-well plate rotated at 50 rpm during the test. After 48 h of incubation, LP-9 layer and SKOV-3 spheroids were separated and washed once with ROS staining buffer followed by staining with 20 μM of DCFDA for 30 min (LP-9 monolayer) or 60 min (SKOV-3 spheroids) at 37 ℃. The stained samples were washed once with ROS staining buffer and the fluorescence signal was measured using a Synergy H1 spectrophotometer (BioTek). Then, 0.8 W/cm^2 of ultrasound irradiation at a frequency of 1Mhz was delivered for 30 s. After ultrasound irradiation, fluorescence signal was measured again. The percent increase of ROS generation was determined from the increase

in fluorescence signal after treatment or irradiation. Tert-butyl hydrogen peroxide (TBHP) was used as positive control in this assay.

Chemotherapy in combination with GNR-PEG-Ce6. Cisplatin (Sigma-Aldrich P4394) and paclitaxel (Sigma-Aldrich T7191) were reconstituted in DMSO to 10 % (w/v) and diluted in cell culture media. SKOV-3 spheroids were treated with GNR-PEG or GNR-PEG-Ce6 for 48 h followed by exposure to 20 μM cisplatin or paclitaxel for 5 days, after which cell viability was evaluated using the Live/Dead assay. Imaging was performed using EVOS FL Auto fluorescence microscope.

Statistical analysis. Statistical analysis was performed with GraphPad Prism, using an unpaired Student's t test to determine P values. All data are presented as mean ± standard deviation of three biological replicates from one of three representative independent experiments. Difference between groups was considered statistically significant when a P value is less than 0.05.

4.3. Results and discussion

4.3.1. PEGylation of GO and GNR to reduce aggregation in the serum-rich ascites microenvironment. Since graphene-based materials are known to have low stability and exhibit significant aggregation in physiological solutions, in part due to nonspecific binding of proteins [164], amine-terminated 4-arm PEG was conjugated to GO and GNR via amide formation to reduce aggregation in ascites, a protein-rich body fluid. FTIR spectra revealed that the signature peaks of 4-arm PEG, a C-O stretch (red region at ~1100 cm^{-1}, Fig. 4-1A) and a COO-H/O-H stretch (blue region at ~2850 cm^{-1})[164], appeared on

GO-PEG and GNR-PEG. In addition, as a consequence of amide formation, a C=O peak in amide bond (yellow region at ~1640 cm^{-1}) appeared in GO-PEG and GNR-PEG. Scanning electron microscope (SEM) images revealed no significant morphological changes in GO and GNR after PEGylation (Fig. 4-1B).

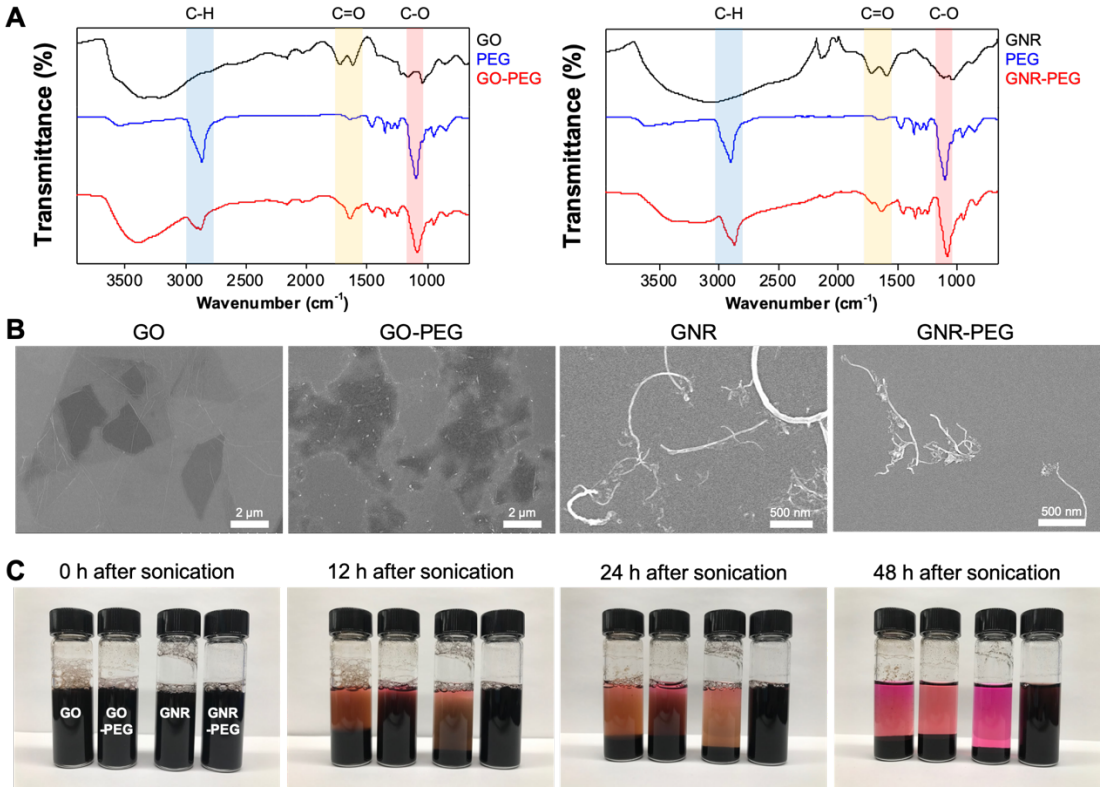

Figure 4-1. PEGylation of GO and GNR to reduce aggregation in serum-rich ascites. (A) FTIR spectra of GO-PEG (left) and GNR-PEG (right). (B) Representative SEM images of GO, GO-PEG, GNR, and GNR-PEG revealed no significant morphological changes after PEGylation (C) Aggregation test in cell culture media containing 20% (v/v) serum (FBS). Graphene-based materials (100 μg/mL) settled over time in serum-rich media due to aggregation by non-specific binding of proteins.

To evaluate aggregation after PEGylation, 100 μg/mL of GO, GNR, GO-PEG and GNR-PEG were suspended in cell culture media containing 20% (v/v) serum, to mimic serum-rich ascites fluid, and monitored over time after brief sonication. The delayed aggregation of GO-PEG and GNR-PEG compared to bare GO and GNR in serum-supplemented cell

culture media is indicative of reduced aggregation following the addition of PEG, with no significant aggregation observed in GNR-PEG at 48 h (Fig. 4-1C). Then, GO-PEG and GNR-PEG were tested with LP-9 human mesothelial cells, a major cellular component in peritoneal cavity, to evaluate their cytocompatibility. While GNR-PEG did not induce any negative effects in viability and proliferation of LP-9 cell layer, GO-PEG significantly reduced the viability, integrity, and proliferation of the mesothelial cell layer at concentrations higher than 50 μg/mL (Fig. 4-2), suggesting that GNR-PEG is more cytocompatible than GO-PEG.

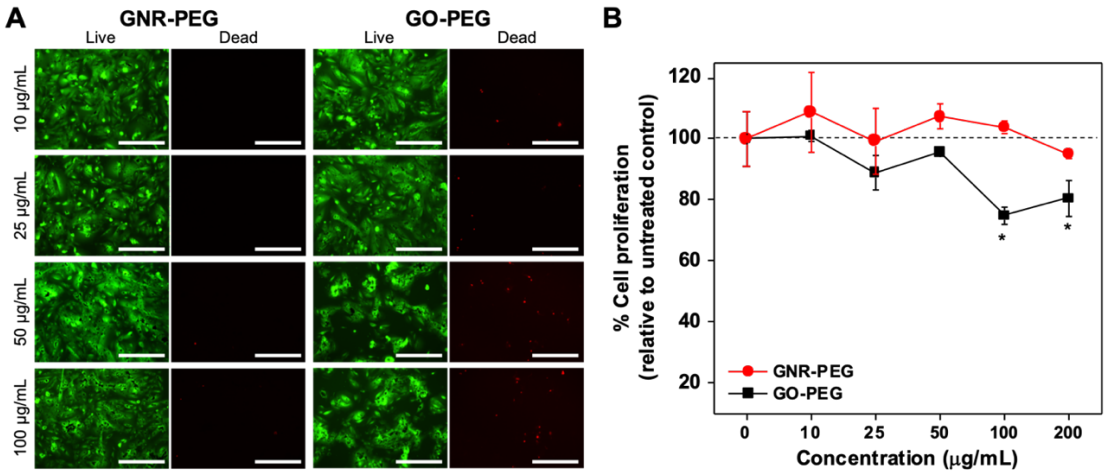

Figure 4-2. GNR-PEG was more cytocompatible to LP-9 mesothelial cells than GO-PEG which significantly deteriorated the integrity and proliferation of LP-9 mesothelial layer. (A) Representative Live/Dead staining images of LP-9 cells treated with GO-PEG or GNR-PEG for 48 h. Scale bars indicate 400 μm. (B) Proliferation of LP-9 cells after 48 h of incubation with GO-PEG or GNR-PEG (*P < 0.05).

4.3.2. GO-PEG and GNR-PEG adsorb to ovarian cancer spheroids and disrupt their adhesion to ECM proteins abundant in mesothelial layer. The SKOV-3 cell line was used to evaluate the interactions between GO-PEG or GNR-PEG and ovarian cancer cells, since this cell line was derived from the ascites fluid of an ovarian cancer patient [180]. Cancer spheroids were generated using an established method [42,181,182]; SKOV-3 cells

placed in culture on a non-adhesive poly(2-hydroxyethyl methacrylate) (pHEMA) surface spontaneously aggregated and formed spheroids. After 24 h, the spheroids ranged from 55 to 330 μm in size, which is in the clinically observed size range of cancer spheroids in the ascites of ovarian cancer patients (30-200 μm [46,161]). Thus, the spheroid formation step was performed for 24 h for all remaining studies. After formation, spheroids were incubated with GO-PEG or GNR-PEG at various concentrations (50-100 μg/mL) for 48 h.

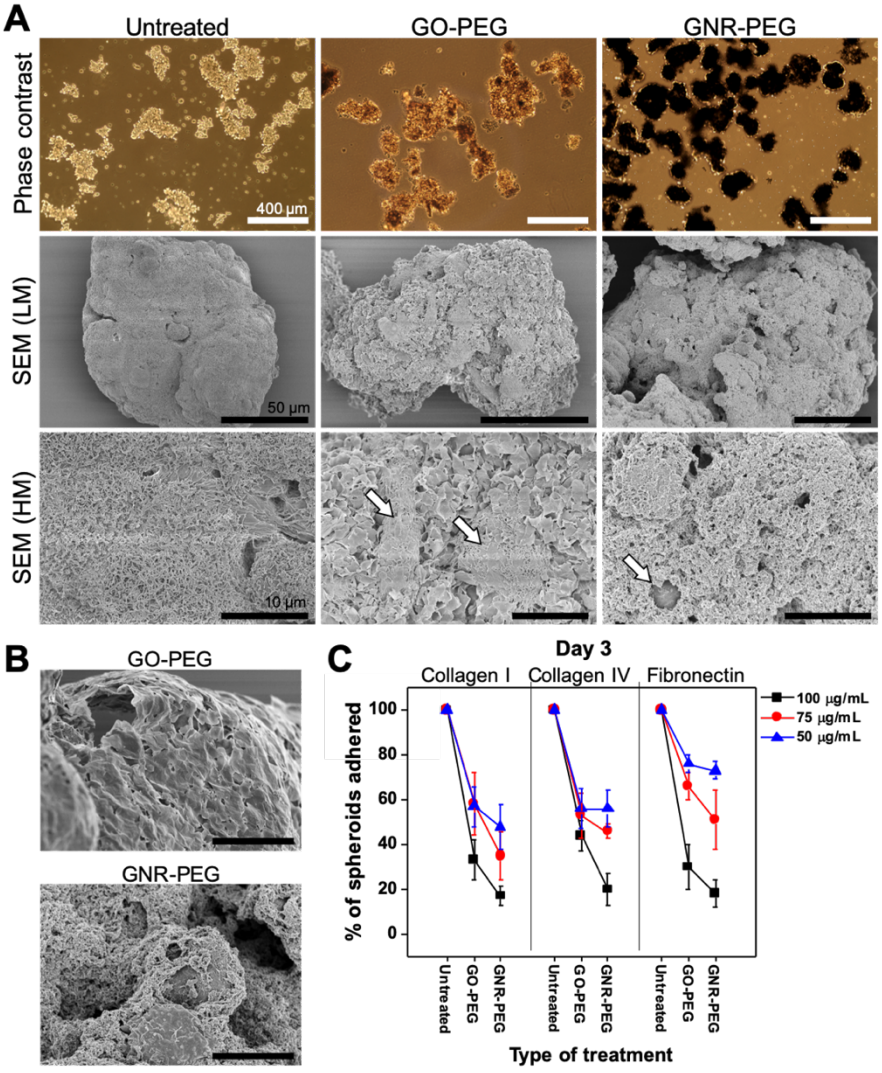

Figure 4-3. GO-PEG and GNR-PEG disrupt adhesion of SKOV-3 spheroids to ECM proteins abundant in mesothelial layer. (A) Representative phase contrast and SEM (LM; low magnification, HM; high magnification) images of SKOV-3 spheroids. Scale bars indicate 400 μm in phase

contrast images, 50 μm (LM), and 10 μm (HM) in SEM images. The white arrows in SEM(HM) images indicate the exposed cell surfaces. (B) SEM images revealed that entangled strands of GNR-PEG formed a barrier with thickness in micrometer range while the thickness of GO-PEG layer was in nanometer range. (C) Percentage of total spheroids that have adhered after 1 and 3 days of incubation on collagen I/IV and fibronectin.

Optical microscope and SEM images revealed that GO-PEG and GNR-PEG adsorbed onto SKOV-3 spheroids, forming a barrier layer covering the surface of the spheroids (Fig. 4-3A). One-dimensional strands of GNR-PEG entangled on the surface formed a dense thick layer, while two-dimensional flat GO-PEG stacked along with the surface formed a thin layer (Fig. 4-3B). These barrier layer of GO-PEG and GNR-PEG were found to disrupt spheroid adhesion to collagen I, IV, and fibronectin, the most abundant ECM proteins on mesothelial layer [158]. When, GO-PEG- or GNR-PEG-treated SKOV-3 spheroids were transferred to ECM protein-coated surfaces in serum-free media, the spheroids displayed significantly inhibited adhesion to collagen I, IV, and fibronectin over 3 days, whereas all untreated SKOV-3 spheroids adhered (Fig. 4-3C). These results suggest that the physical barrier of GO-PEG/GNR-PEG on the surface could interfere with surface receptor-ECM protein interactions. In comparison, a conventional approach using antibody blocking of surface receptors such as integrin β1 or CD44, which have been shown to inhibit spheroid adhesion to ECM proteins for short time periods (2 h) in previous studies [46,161], did not have considerable blocking effects over 3 days under these conditions (Fig. 4-4). Increasing the concentration of GO-PEG or GNR-PEG from 50 to 100 μg/mL led to a decrease in adhesion rate, suggesting that higher concentrations provide better blocking effects. Since GNR-PEG exhibited greater adhesion blocking effects and cytocompatibility than GO-PEG, GNR-PEG was used for the remaining studies.

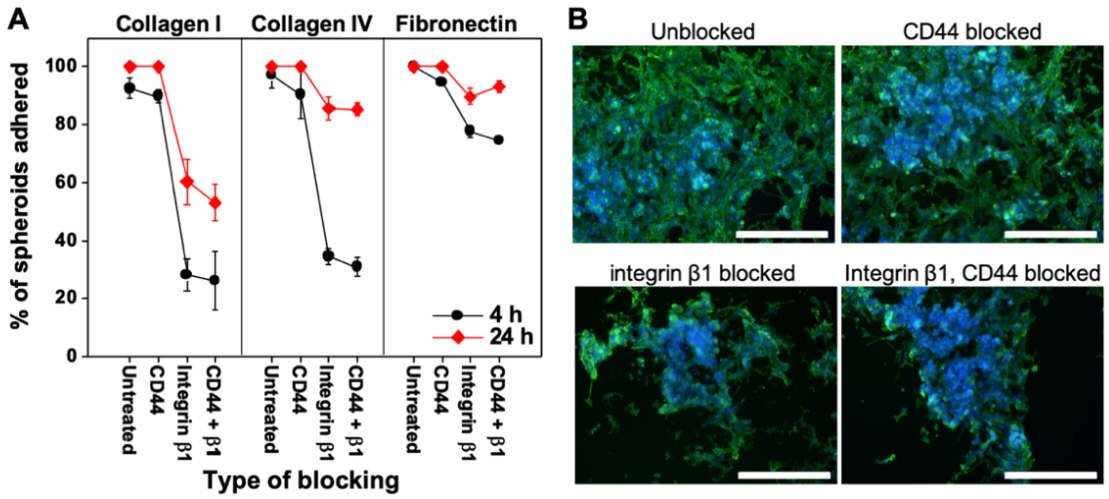

Figure 4-4. Blocking surface receptors is not sufficient to disrupt spheroid adhesion to ECM proteins. (A) Percentage of total SKOV-3 spheroids that have adhered at 1 and 3 days after incubation on collagen I/IV and fibronectin. Antibody blocking of surface receptors was performed for 48 h prior to the adhesion test. (B) Representative fluorescence images of F-actin (green) and DAPI (blue) immunostaining in spheroids adhered to fibronectin-coated surfaces.

GNR-PEG also inhibited disaggregation, the dissociation of the spheroid into single cells, and spreading of adhered SKOV3 spheroids (Fig. 4-5). Following adhesion, metastasizing ovarian cancer spheroids disaggregate and spread rapidly, with the spreading areas growing in size up to 200-fold in a week [54], in order to establish secondary tumors. While untreated SKOV-3 spheroids exhibited an average spreading distance of 58 ± 15 μm at 4 h, GNR-PEG-treated spheroids did not exhibit any visible spreading at this timepoint. Furthermore, the average spreading distance of untreated spheroids over 24 h was significantly higher compared to that of GNR-PEG-treated SKOV-3 spheroids, indicating that the barrier layer of GNR-PEG inhibits disaggregation and spreading of adhered spheroids. It was previously found that disaggregation and spreading of ovarian cancer spheroids are also mediated by interactions between surface receptors and ECM proteins, primarily integrin β1 and collagen I [54]. Thus, the barrier layer of GNR-PEG that interferes with surface receptor-ECM protein interactions in the process of spheroid

adhesion likely also inhibits disaggregation and spreading of spheroids once they have adhered.

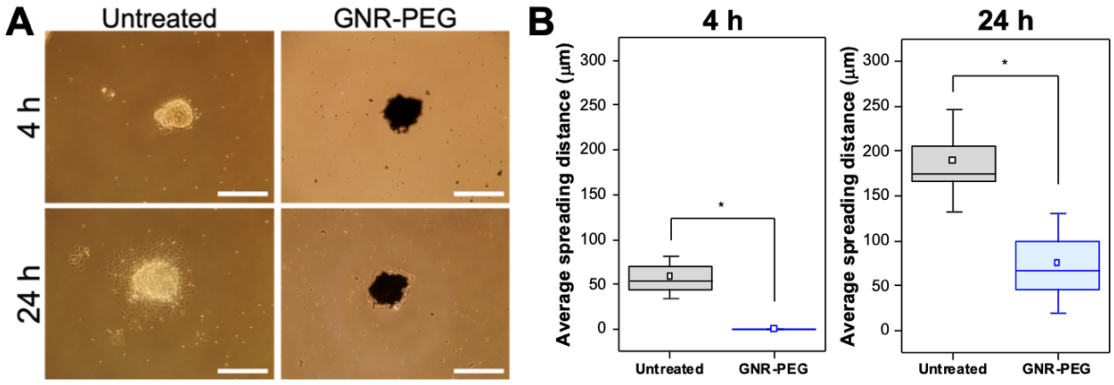

Figure 4-5. GNR-PEG disrupts disaggregation and spreading of adhered SKOV-3 spheroids. (A) Disaggregation and spreading of adhered SKOV-3 spheroids were evaluated at 4 and 24 h after adhesion. Scale bars indicate 400 μm. (B) Average spreading distance of untreated and GNR-PEG-treated SKOV-3 spheroids at 4 and 24 h after adhesion was measured using ImageJ software (*$P < 0.05$).

4.3.3. Chlorin e6 (Ce6) loaded onto GNR-PEG enhances adhesion blocking effects of GNR-PEG by downregulating surface receptor proteins. Although coating the surface of ovarian cancer spheroids with GNR-PEG significantly inhibited their adhesion to ECM proteins, some spheroids treated with GNR-PEG were still able to adhere (Fig. 4-3C). Thus, we sought to develop a strategy by which the adsorption of GNR-PEG onto tumor spheroids attached to the mesothelial layer could be used to kill the cancer cells. To this end, we loaded Ce6 onto GNR-PEG via pi-pi stacking, noncovalent bonding between aromatic rings. Ce6 is a naturally occurring sonosensitizer, and its anti-tumor activity in sonodynamic therapy has been confirmed on various tumors including leukemia, breast, and liver cancers [183–185]. In addition, Ce6 was found to have selective accumulation in the tumor and rapid clearance from normal tissues in many previous studies [186,187], which potentially reduces the risk of side effects in normal tissues in peritoneal cavity. The

loading of Ce6 was confirmed by UV-VIS spectrometry, in which characteristic absorption peaks of Ce6 at 400 nm and 660 nm appeared on the UV-VIS spectra of GNR-PEG-Ce6 (Fig. 4-6A). Since a significant amount of undissolved Ce6 was visible at concentrations higher than 0.1 mg/mL due to the low solubility of Ce6 in water, 0.1 mg/mL was chosen as the concentration for Ce6 loading in our study to minimize wasted Ce6.

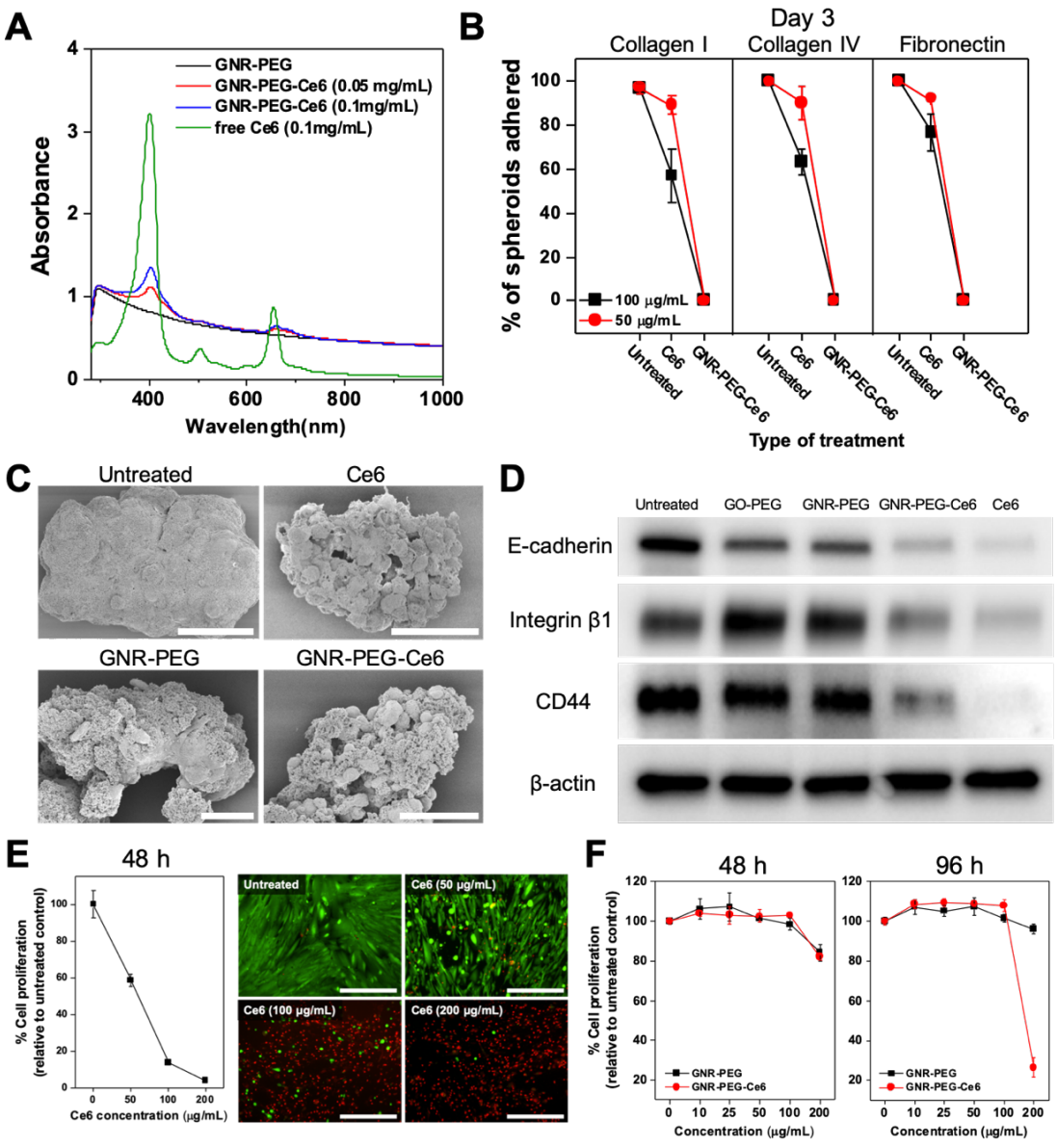

Figure 4-6. Ce6 loading onto GNR-PEG further reduces spheroid adhesion to ECM proteins by downregulating surface receptor proteins. (A) UV-VIS spectra of free Ce6, GNR-PEG, and GNR-

PEG-Ce6. (B) Percentage of total spheroids that have adhered after 3 days of incubation on collagen I/IV and fibronectin. (C) Representative SEM images of untreated, Ce6-treated, GNR-PEG-treated, and GNR-PEG-Ce6-treated SKOV-3 spheroids. Scale bars indicate 50 μm. (D) Western blot analysis of protein expression in untreated, GO-PEG-treated, GNR-PEG-treated, GNR-PEG-Ce6-treated, and Ce6-treated SKOV-3 spheroids after 48 h of treatment.

Interestingly, GNR-PEG-Ce6 exhibited greater adhesion blocking effects compared with GNR-PEG. In the *in vitro* adhesion assays, none of the SKOV-3 spheroids treated with 50 μg/mL of GNR-PEG-Ce6 were able to adhere to any of the ECM proteins by 72 h. Ce6 alone had no significant blocking effects at 50 μg/mL but it significantly disrupted spheroid adhesion to ECM proteins (Fig. 4-6B) at 100 μg/mL. In addition, Ce6 led to significant changes in spheroid morphology. SKOV-3 spheroids treated with Ce6 or GNR-PEG-Ce6 displayed a grape-like morphology with loosened cell-cell adhesion compared with tight cell-cell adhesion in the spheroids without Ce6 exposure (Fig. 4-6C). It was found that SKOV-3 spheroids treated with 100 μg/mL of Ce6 for 48 h displayed significantly downregulated expression of E-cadherin, which mediates cell-cell adhesion. Furthermore, integrin β1 and CD44 that mediate spheroid adhesion to ECM proteins also exhibited a significant decrease in Ce6-treated spheroids compared with untreated spheroids (Fig. 4-6D). Ce6 loaded onto GNR-PEG was also able to induce significantly reduced expression of these surface receptors in SKOV-3 spheroids, whereas GNR-PEG alone did not significantly decrease their expression. Thus, enhanced blocking effects of GNR-PEG-Ce6 are likely attributed to the downregulation of surface receptors that mediate spheroid adhesion. Though Ce6 alone has adhesion blocking effects at 100 μg/mL, significant cytotoxic effects on LP-9 mesothelial cells at this dose (Fig. 4-6E, F) limit its therapeutic use. In contrast, GNR-PEG-Ce6 exhibited significantly less toxicity at its effective concentrations (50-100 μg/mL, Fig. 4-6E, F) where no spheroid adhesion was

observed, as localized delivery of Ce6 to spheroids via GNR-PEG-Ce6 allows for a lower quantity of Ce6 to achieve similar effects, significantly reducing toxicity to mesothelial cells.

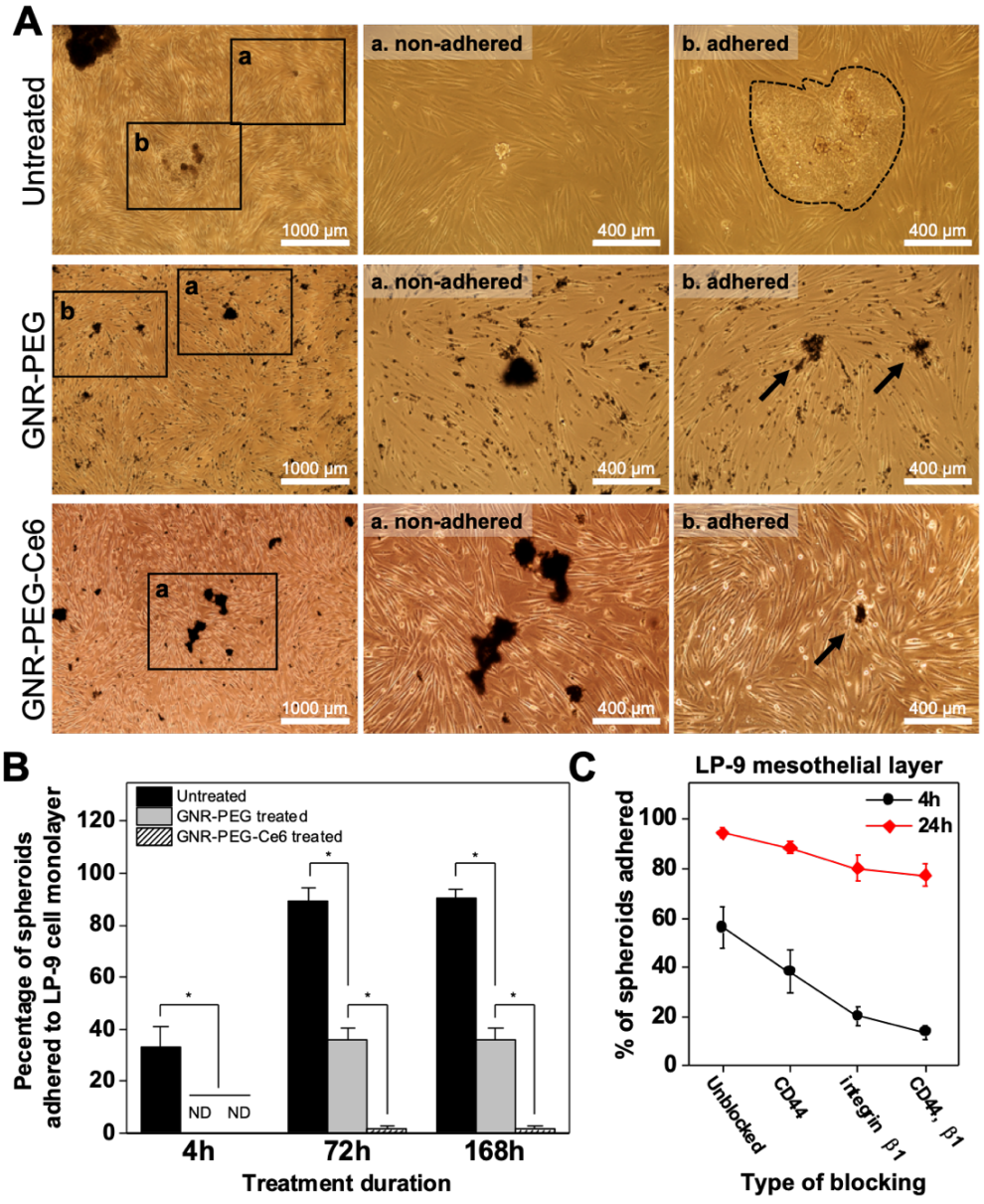

Figure 4-7. GNE-PEG-Ce6 disrupts mesothelial adhesion of SKOV-3 spheroids and subsequent mesothelial clearance. (A) Representative phase contrast images of adhered and non-adhered spheroids in each condition after 72 h of incubation. (B) Percentage of total spheroids that have adhered to the LP-9 mesothelial cell layer after 4, 72, and 168 h of incubation (*$P < 0.05$, ND indicates non-detected). (C) Percentage of total SKOV-3 spheroids that have adhered to LP-9 mesothelial cell monolayers after 4 and 24 h of incubation.

4.3.4. GNR-PEG-Ce6 inhibits spheroid adhesion to mesothelial layer and subsequent mesothelial clearance. To examine whether GNR-PEG-Ce6 could also disrupt mesothelial adhesion of ovarian cancer spheroids, GNR-PEG-Ce6 was tested in an ascites-like *in vitro* microenvironment in which SKOV-3 spheroids were suspended on top of a confluent LP-9 mesothelial cell layer. Then, 50 μg/mL of GNR-PEG-E6 was added to the SKOV-3 spheroid suspension with orbital shaking at 50 rpm to mimic the movement of ascites in the peritoneal cavity, a crucial factor in the peritoneal microenvironment affecting the efficacy of therapeutic intervention [188–190]. It was found that GNR-PEG and GNR-PEG-Ce6 preferentially adsorbed onto SKOV-3 spheroids as opposed to the LP-9 cells (Fig. 4-7A).Preferential accumulation of GNR-PEG and GNR-PEG-Ce6 on the spheroids instead of the LP-9 layer was likely attributed to the enhanced stability of the materials in serum-rich physiological buffers, which provided GNR-PEG and GNR-PEG-Ce6 more time to interact with ovarian cancer spheroids before these materials settled due to aggregation. While 33 ± 8.2% of untreated SKOV-3 spheroids adhered to LP-9 cell layer at 4 h, GNR-PEG- or GNR-PEG-Ce6-treated SKOV-3 spheroids were not able to adhere by that timepoint (Fig. 4-7B). Furthermore, over 90% of untreated SKOV-3 spheroids and 40% of GNR-PEG-treated spheroids adhered to LP-9 cell layer by 72 h, whereas less than 2% of SKOV-3 spheroids treated with GNR-PEG-Ce6 were able to adhere in 72 h. This is likely attributed to the synergistic effects from the reduced expression of surface receptors by Ce6 and the barrier layer of GNR-PEG-Ce6. In comparison to GNR-PEG-Ce6, the conventional approach of blocking integrin β1 or CD44 with antibodies did not effectively inhibit mesothelial adhesion under the same experimental conditions. More than 80% of spheroids were able to adhere to LP-9 monolayer and spread out by 24 h in all groups

regardless of blocking (Fig. 4-7C), indicating that directly blocking surface receptors does not provide the longer-term efficacy of GNR-PEG-Ce6.

GNR-PEG-Ce6 also inhibited subsequent spreading of adhered spheroids on mesothelial layer. Following adhesion on mesothelial layer, metastasizing spheroids spread by clearing mesothelial cells from their path at adhesion sites, a phenomenon termed mesothelial cell clearance, in a talin-1- and integrin α5β1-dependent manner [48,191]. This has also been observed in clinical biopsies of patient tumors attached to peritoneal organs showing the absence of mesothelial cells underneath the attached tumor [191]. In our test, LP-9 cells underneath untreated SKOV3 spheroids exhibited clearance in 2 h (Fig. 4-8), which is consistent with the previous finding that tumor spheroids began clearing mesothelial layer 30 min after spheroids attachment [192]. In contrast, LP-9 cells beneath the SKOV-3 spheroids treated with GNR-PEG or GNR-PEG-Ce6 displayed significantly delayed clearance, with the lowest level of clearance observed with GNR-PEG-Ce6. After 24 h of incubation, clearance of the LP-9 cell layer was visible in all groups except GNR-PEG-Ce6, which displayed no sign of clearance over a 24 h period.

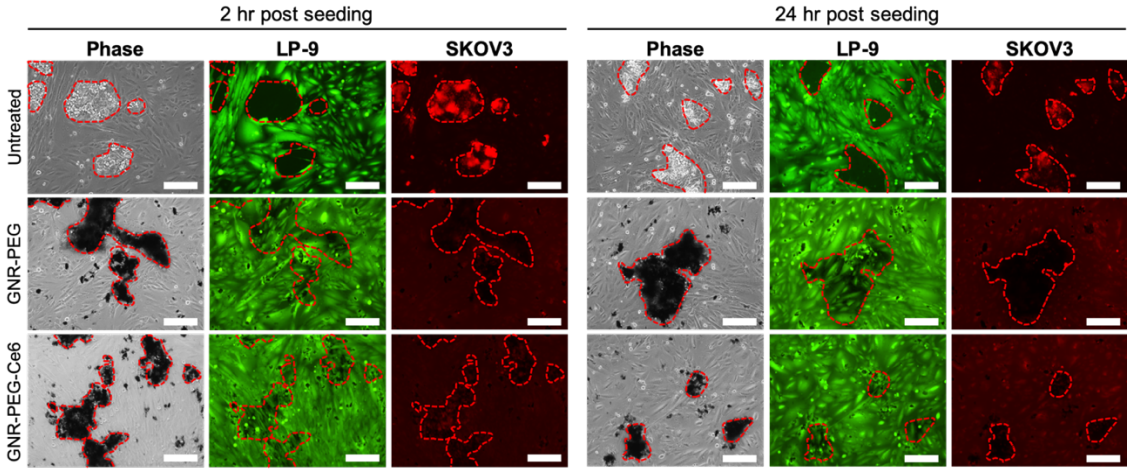

Figure 4-8. GNE-PEG-Ce6 disrupts mesothelial clearance. Representative phase contrast images of SKOV-3 spheroids breaching the underlying LP-9 monolayer and corresponding fluorescence images

of the LP-9 monolayer (green) and SKOV-3 spheroids (red). Mesothelial clearance by SKOV-3 spheroids was captured at 2 and 24 h after spheroid seeding. Scale bars indicate 200 μm.

Western blot analysis revealed that GNR-PEG-Ce6 downregulates integrin α5 as well as β1 that mediate mesothelial clearance (Fig. 4-9). Thus, the delay observed in mesothelial clearance could be in part due to the downregulation of integrin α5β1, a key player in mesothelial clearance, as blocking α5β1 integrin was found to decrease mesothelial clearance in a previous study [191].

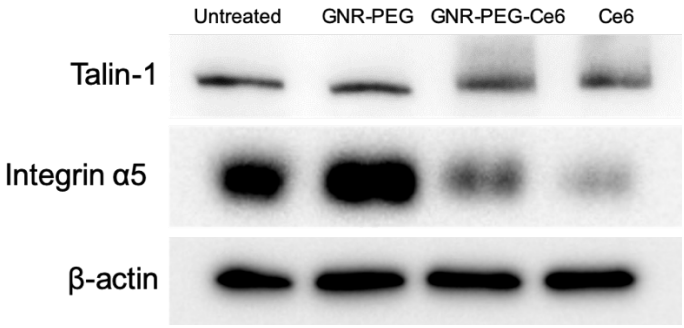

Figure 4-9. Ce6 significantly downregulates integrin α5 as well as β1 in SKOV-3 spheroids, delaying the mesothelial clearance. The expression of talin-1 was not significantly affected by Ce6. β-actin was used as loading control. The whole protein was extracted after 48 h of the treatments.

4.3.5. GNR-PEG-Ce6 can kill ovarian cancer spheroids via sonodynamic therapy and enhance the efficacy of adjuvant chemotherapy. To evaluate whether the sonodynamic therapy using GNR-PEG-Ce6 could kill adhered ovarian cancer spheroids, SKOV-3 spheroids placed on top of a confluent LP-9 cell monolayer were treated with 50 μg/mL of GNR-PEG-Ce6 for 48 h, with orbital shaking at 50 rpm. Non-adhered spheroids were removed after 48 h of treatment, and ultrasound irradiation was delivered from the top (Fig. 4-10A). Live/Dead images revealed no significant cell death prior to ultrasound irradiation in all conditions: untreated, GNR-PEG-treated, and GNR-PEG-Ce6-treated (Fig. 4-10B).

After 30 s of 0.8 W/cm^2 ultrasound irradiation at a frequency of 1 MHz, massive cell death was detected in GNR-PEG-Ce6-treated spheroids adhered to the LP-9 layer (Fig. 4-10B).

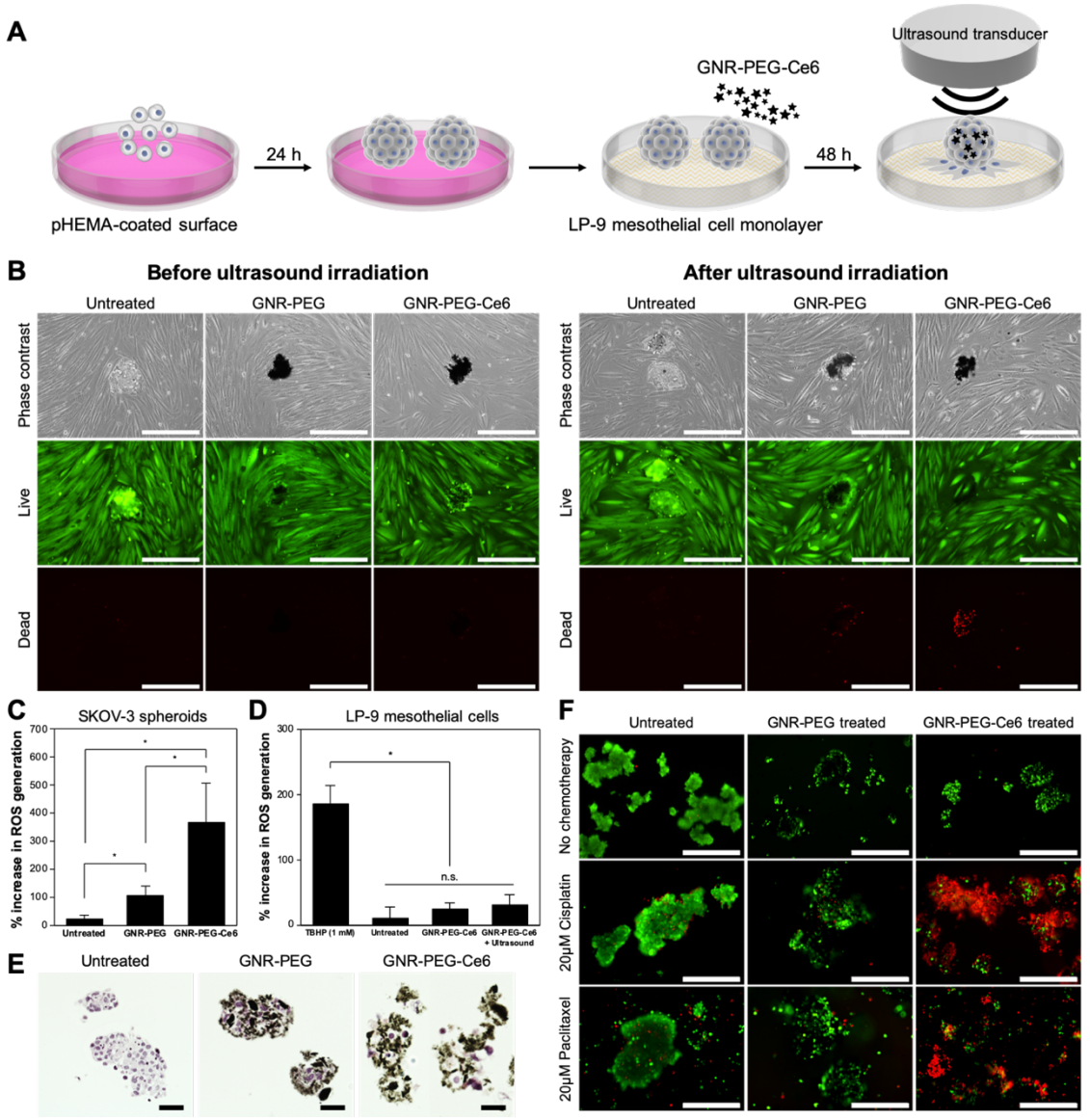

Figure 4-10. GNE-PEG-Ce6 can kill adhered ovarian cancer spheroids via sonodynamic therapy. (A) A schematic of ultrasound irradiation of adhered spheroids. (B) Representative Live/Dead staining images of untreated, GNR-PEG-treated, and GNR-PEG-Ce6-treated SKOV-3 spheroids adhered to the LP-9 mesothelial cell layer before and after ultrasound irradiation. Scale bars indicate 400 μm. (C, D) ROS generation in SKOV-3 spheroids (C) and LP-9 mesothelial cells (D) after ultrasound irradiation. (*$P < 0.05$) (E) Histological cross-sectional view of untreated, GNR-PEG-treated, GNR-PEG-Ce6-treated SKOV-3 spheroids. Scale bars indicate 50 μm. (F) Representative Live/Dead images of untreated, GNR-PEG-treated, GNR-PEG-Ce6-treated SKOV-3 spheroids after 5 days of chemotherapy with 20 μM cisplatin (middle row), 20 μM of paclitaxel (bottom row). Scale bars indicate 400 μm.

Furthermore, GNR-PEG-Ce6-treated spheroids detached from the LP-9 layer during the ultrasound irradiation, suggesting weak adhesion between the spheroids and LP-9 layer. In addition to the spheroids adhered to LP-9 layer, GNR-PEG-Ce6-treated spheroids that had not adhered to the LP-9 cells were also completely killed when ablated separately with the same level of ultrasound irradiation. Ultrasound irradiation alone triggered no significant cell death in SKOV-3 spheroids or LP-9 monolayers. Some cell death was also observed in GNR-PEG-treated spheroids after ultrasound irradiation, but it was not as significant as in the GNR-PEG-Ce6-treated spheroids, suggesting that cell death in GNR-PEG-Ce6-treated spheroids was primarily induced by the sonodynamic effect of Ce6. Cell death by sonodynamic therapy has been shown to be mediated by the generation of reactive oxygen species (ROS), which trigger apoptotic pathways within cells [187]. It was found that ROS generation upon ultrasound irradiation was significantly higher in GNR-PEG-Ce6-treated SKOV-3 spheroids compared with other groups (Fig. 4-10C). GNR-PEG also increased ROS generation upon ultrasound irradiation in SKOV-3 spheroids but not to the same level as GNR-PEG-Ce6. In addition, ROS generation in LP-9 cells was not significantly affected after ultrasound irradiation, likely due to the preferential accumulation of GNR-PEG-Ce6 on SKOV-3 spheroids over LP-9 cells (Fig. 4-10D). Furthermore, GNR-PEG-Ce6 was not confined to the surface but actually penetrated deep into the SKOV-3 spheroids, allowing the delivery of Ce6-induced sonodynamic effects throughout the spheroids (Fig. 4-10E).

GNR-PEG-Ce6 also enhanced the efficacy of adjuvant chemotherapy which can used to kill residual ovarian cancer spheroids after sonodynamic therapy. Current adjuvant chemotherapy for advanced stage ovarian cancer typically uses platinum- or taxane-based

drugs [193,194] but ovarian cancer spheroids have been found to have enhanced resistance to these drugs for many reasons, including poor drug penetration [195] and the presence of a number of cell-cell junctions in spheroids [196–198]. For example, cisplatin, a platinum-based drug widely used for ovarian cancer, has shown limited penetration, being confined to the peripheral layer of cancer spheroids (0-30 μm) in previous studies [199,200]. Consistent with these previous findings, chemotherapy alone with cisplatin or paclitaxel was not able to induce significant cell death in SKOV-3 spheroids (Fig. 4-10F). However, a significant number of cells in GNR-PEG-Ce6-treated spheroids were killed by the same chemotherapy without sonodynamic therapy (Fig. 4-10F). This is likely due to the fact that the loosened cell-cell junctions in GNR-PEG-Ce6-treated spheroids enhanced the penetration of cisplatin or paclitaxel, whereas a barrier of tight cell-cell junctions in untreated and GNR-PEG-treated spheroids did not allow those drugs to penetrate throughout. Indeed, it was previously reported that epithelial junction opener (JO-1) improved the efficacy of co-administered chemotherapeutic drugs by loosening cell-cell junctions in an ovarian cancer model [197,198]. These results suggest that GNR-PEG-Ce6 can be combined with conventional chemotherapy to kill ovarian cancer spheroids in peritoneal cavity, offering an additional therapeutic route with this material.

4.3.6. GNR-PEG-Ce6 can disrupt mesothelial adhesion of ovarian cancer spheroids in patient ascites and destroy them via sonodynamic therapy. Lastly, to demonstrate the translational potential of this material, GNR-PEG-Ce6 was tested with patient ascites spheroids. Prior to the studies, the staining of the spheroids with ovarian cancer marker cancer antigen 125 (CA125) and cytokeratin 7 (CK7) verified that they contained tumor cells (Fig. 4-11A).

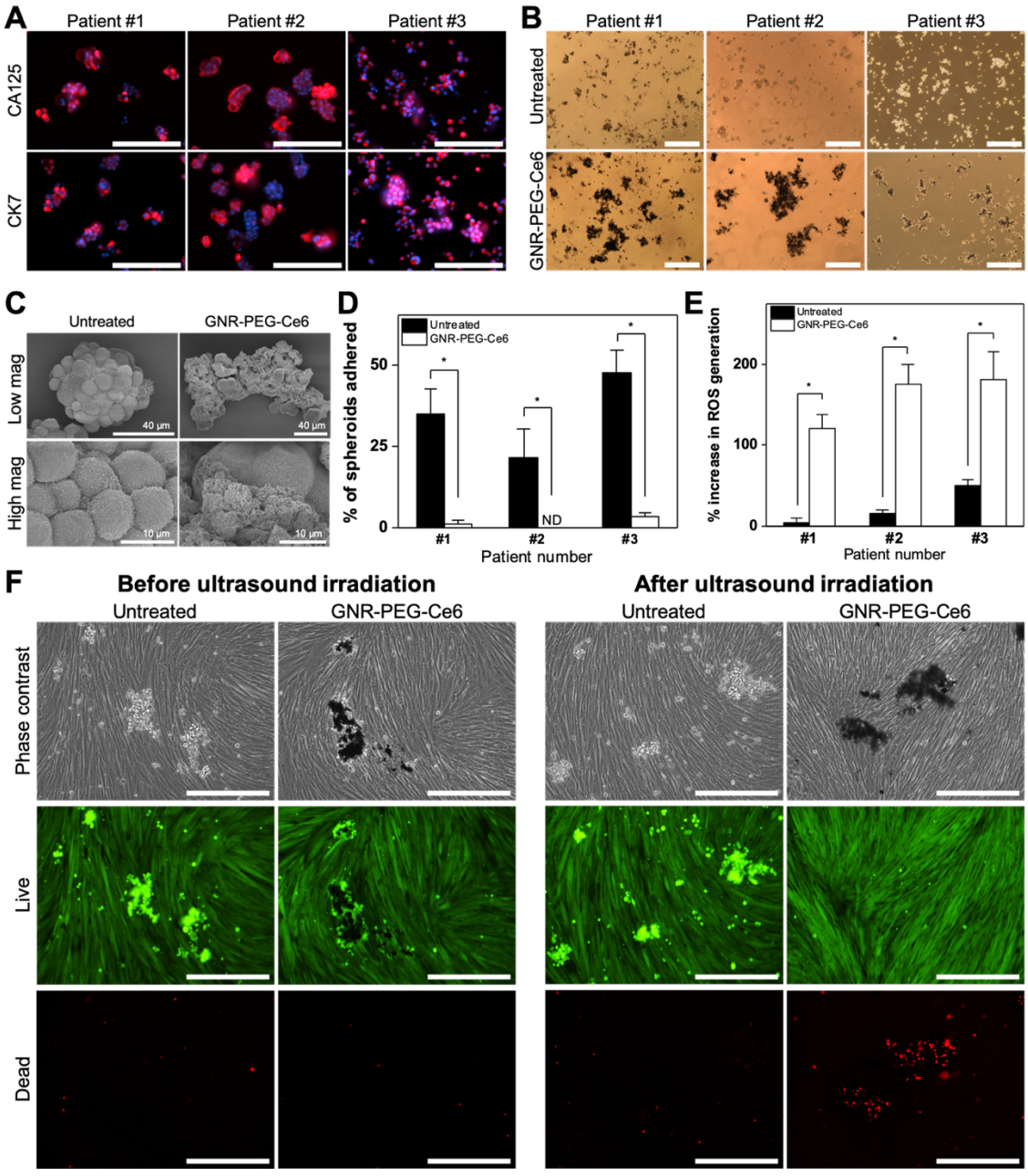

Figure 4-11. GNE-PEG-Ce6 can disrupt mesothelial adhesion of patient ascites spheroids and destroy them via sonodynamic therapy. (A) Representative immunofluorescence images of CA125 and CK7 expression in patient ascites spheroids. (B, C) Representative phase contrast (B) and SEM (C) images of untreated and GNR-PEG-Ce6-treated patient ascites spheroids. (D) Percentage of total patient ascites spheroids that have adhered to the LP-9 mesothelial cell layer after 72 h of incubation. (E) ROS generation in patient ascites spheroids after 30 s of 0.8 W/cm^2 ultrasound irradiation. (F) Representative Live/Dead staining images of untreated, and GNR-PEG-Ce6 treated patient ascites spheroids that have adhered to LP-9 mesothelial cell layer before and after ultrasound irradiation.

GNR-PEG-Ce6 was able to adsorb onto patient ascites spheroids by 48 h of treatment (Fig. 4-11B, C), forming a barrier layer on the outer surface. To evaluate adhesion, patient ascites spheroids were mixed with 50 μg/mL of GNR-PEG-Ce6 and placed on top of a confluent LP-9 cell layer. While the adhesion rate of untreated ascites spheroids after 72 h of incubation was lower compared to that of SKOV-3 spheroids, GNR-PEG-Ce6 significantly inhibited adhesion of patient ascites spheroids in all patient samples (Fig. 4-11D). When 30 s of 0.8 W/cm^2 ultrasound irradiation was applied to GNR-PEG-Ce6-treated spheroids, ROS generation significantly increased (Fig. 4-11E) and significant cell death was also observed in patient ascites spheroids adhered to LP-9 layers (Fig. 4-12F). GNR-PEG-Ce6-treated patient ascites spheroids that had not adhered to LP-9 layers could be also be destroyed by ultrasound irradiation. These results collectively demonstrate that GNR-PEG-Ce6 combined with sonodynamic therapy has therapeutic potential for advanced stage ovarian cancer patients.

4.4. CONCLUSIONS

There is an urgent need for development of alternative treatment options for ovarian cancer, which is typically diagnosed at advanced stages in which tumor spheroids are spreading throughout the abdominal cavity. In this study, we report a novel material-based therapeutic strategy using GNR functionalized with 4-arm PEG and the sonosensitizer Ce6 to reduce metastatic spread of ovarian cancer within the peritoneal space. Our results demonstrate that GNR-PEG-Ce6 can adsorb to the surface of ovarian cancer spheroids, forming a physical barrier layer which disrupts mesothelial adhesion of the spheroids. GNR-PEG-Ce6 also significantly delays disaggregation and spreading as well as

mesothelial clearance of adhered spheroids, key steps in the establishment of ovarian cancer metastases. In addition, when combined with ultrasound irradiation, GNR-PEG-Ce6 kills SKOV-3 spheroids adhered to LP-9 mesothelial cell monolayers via sonodynamic effects with minimal off-target damage, suggesting that this approach can eliminate residual tumors in peritoneal cavity. Furthermore, GNR-PEG-Ce6 can enhance the efficacy of conventional chemotherapy using cisplatin or paclitaxel in killing the ovarian cancer spheroids, offering another therapeutic route with this material. The efficacy of GNR-PEG-Ce6 was also validated with ovarian cancer spheroids derived from patient ascites, demonstrating the translational potential of GNR-PEG-Ce6 in future clinical use. Given that GNE-PEG-Ce6 offers a new therapeutic route via minimally invasive sonodynamic therapy as well as enhancing conventional chemotherapy, targeting of metastatic cancer spheroids in the peritoneal cavity using GNR-PEG-Ce6 could provide promising strategies for preventing intraperitoneal spread of ovarian cancer.

Chapter 5 – Conclusions and future directions

5.1. General conclusions

The aims of the work presented in this dissertation were (i) to establish *in vitro* and *in vivo* experimental platforms to study how hypoxia regulates tumor dormancy in breast and ovarian cancer and (ii) to develop a therapeutic strategy to target metastasizing ovarian cancer spheroids that is an alternative to chemotherapy, which cannot destroy dormant cells. The work discussed in Chapter 2 demonstrated that the hypoxia-mimetic agent $CoCl_2$ can stably induce and maintain dormancy in breast and ovarian cancer cells, as evidenced by several hallmarks of dormancy: restrained cell growth, reversible cell cycle arrest at G0/G1 phase, and reduced expression of cell cycling marker Ki67 in conjunction with stabilization of HIF1α. This was the first demonstration that $CoCl_2$ can stably recapitulate hypoxic regulation of cancer dormancy, including the heterogeneity of cellular responses to hypoxia. This platform enables detailed investigation of the induction of dormancy under hypoxia in a more robust and versatile manner compared to conventional hypoxia chambers. For example, the $CoCl_2$-based model can be readily integrated with previously established models that modulate other cellular and molecular components of the metastatic microenvironment. This versatility of the $CoCl_2$ model could widen our understanding of the potential cellular or molecular cues regulating cancer dormancy under hypoxia. In addition, this platform could aid in our understanding of why the heterogeneity in cellular responses to pro-dormancy cues provided under hypoxia arises. Given that hypoxia and cancer dormancy have been associated with increasing the risk for tumor recurrence, resulting in poor clinical outcomes, information extracted from the $CoCl_2$-based platform has the potential to identify novel therapeutic strategies for preventing recurrence.

In the work discussed in Chapter 3, a biomaterial platform that recapitulates an *in vivo* hypoxic metastatic niche was established to study hypoxic regulation of DTCs at metastatic sties. Recently, the significance of hypoxia in adaptation of DTCs to metastatic sites and subsequent dormancy or proliferation has been recognized in an increasing number of studies. However, it has been challenging to study the detailed mechanisms underlying how hypoxia at the metastatic site affects DTCs in concert with other factors due to the lack of appropriate experimental models. In addition, it is challenging to access natural hypoxic metastatic sites in the body, such as bone marrow, with current imaging techniques. To address these issues, microporous PLG scaffolds that were previously shown to recruit DTCs when implanted in mice by recapitulating the local immune microenvironment of actual metastatic sites was used in combination with $CoCl_2$. $CoCl_2$ was incorporated into the PLG scaffolds to generate a hypoxic microenvironment within the metastatic niche created by PLG scaffolds. When implanted into mice beneath the skin, Co-PLG scaffolds established hypoxic microenvironments, as evidenced by the stabilization of HIF1α and increased blood vessel formation *in vivo*. Furthermore, the recruitment of 4T1 metastatic breast cancer cells to Co-PLG scaffolds was confirmed by evaluating the gene expression of MT2, which is known to be highly expressed in 4T1 breast tumors. These results demonstrate that Co-PLG scaffolds can establish a hypoxic metastatic site in an experimentally accessible area beneath the skin, providing a novel platform to investigate hypoxic regulation of DTCs at metastatic sites.

Lastly, a therapeutic strategy using GNR functionalized with PEG and Ce6 to target dormant ovarian cancer spheroids was developed in Chapter 4. Recurrent ovarian cancer has limited therapeutic options due to the widespread metastasis driven by extensive seeding of ovarian cancer spheroids in the peritoneal cavity, which in most cases are

resistant to standard chemotherapy. Thus, there has been an urgent need for alternative treatment options for advanced stage ovarian cancer in which tumor spheroids are spreading throughout the abdominal cavity. This work demonstrates that sonosensitizer functionalized GNR (GNR-PEG-Ce6) can disrupt mesothelial adhesion of ovarian cancer spheroids as well as kill ovarian cancer spheroids via sonodynamic ablation. GNR-PEG-Ce6 formed a physical barrier on the outer surface of the spheroid and downregulated surface adhesion receptors, significantly inhibiting spheroid adhesion to the LP-9 mesothelial layer. More importantly, localized delivery of Ce6 to ovarian cancer spheroids via GNR-PEG-Ce6 enabled sonodynamic ablation of spheroids adhered on the LP-9 cell monolayer, with significantly reduced cytotoxic effects compared with free Ce6. In addition, GNR-PEG-Ce6 also enhanced the efficacy of adjuvant chemotherapy using cisplatin or paclitaxel, which typically have difficult penetrating ovarian cancer spheroids, by loosening cell-cell adhesions within the ovarian cancer spheroids. Most importantly, GNR-PEG-Ce6 exhibited the same efficacy with ovarian cancer spheroids derived from patient ascites, demonstrating the translational potential in future clinical use. Thus, this approach could provide promising strategies for preventing intraperitoneal spread of ovarian cancer.

5.2. Future directions

5.2.1. Identification of key molecular mechanisms of heterogeneity in cell responses to hypoxia using the $CoCl_2$-based *in vitro* platform combined with computational modeling

Cancer cells frequently display substantial heterogeneity, which gives rise to differential sensitivity to anti-cancer drugs, and this heterogeneity is also found in cellular

responses to hypoxia. For instance, MCF-7 breast cancer cells became dormant while MDA-MB-231 breast cancer cells remained proliferative under hypoxia or hypoxia-mimicking microenvironments in Chapter 2. Given that this heterogeneity often poses challenges in therapeutic efficacy, a better mechanistic understanding of what leads to the heterogeneity is critical to designing more effective therapies to reduce tumor recurrence.

The experimental results from qRT-PCR and western blot analysis in Chapter 2 revealed differential expression of p21 and its target CDK2-cyclin complexes in MCF-7 and MDA-MB-231 under hypoxia, suggesting that p21 could be a major driver of heterogeneity under hypoxia. However, p21 is involved in complex signaling networks, and its activity is regulated by a number of upstream and downstream factors. For instance, p21 activation under hypoxia is regulated by p53, a tumor suppressor protein that has different functional status in MCF-7 and MDA-MB-231 cells. Thus, the complex networks regulating p21 activity need to be investigated to understand what drives the heterogeneity observed in MCF-7 and MBA-MB-231 cells under hypoxia.

While experimental data extracted from the $CoCl_2$-based *in vitro* platform could provide the mechanistic information needed to model the p21 regulation under hypoxia, the challenge lies in the large number of hypotheses that needs to be experimentally tested. To reduce the experimental conditions that need to be probed, computational analysis using mathematical modeling could be used to rapidly test multiple hypotheses on underlying biochemical processes. Reducing the number of experimental conditions will result in a faster and more efficient workflow that can be used to understand cell behavior and develop better strategies to effectively target the tumor population. Combined with computational analysis, experimental data extracted from the $CoCl_2$-based *in vitro* platform can provide

the mechanistic information necessary for analyzing how the behavior of cancer cells varies depending on key molecular cues under hypoxia.

Computational simulations with a mathematical model could also be used to explain cell-to-cell heterogeneity in dormancy induction observed in MCF-7 population in Chapter 2; some MCF-7 cells became dormant but others did not under the same hypoxic stresses. Since the $CoCl_2$ platform can provide a facile, higher-throughput and well-controlled hypoxic microenvironment compared to conventional hypoxia chambers, minimizing extrinsic variability, it can be also used to draw conclusions about cell-to-cell heterogeneity due to genetic and epigenetic variability as well as intrinsic noise, specifically, stochasticity due to low molecule numbers, cell cycle position, transcription and translation variability, as well as differing initial concentrations of the components. With experimental data extracted using $CoCl_2$ platform, computational simulation could predict how these intrinsic factors affecting p21 lead to the cell-to-cell heterogeneity in dormancy induction.

5.2.2. Identification of key therapeutic targets in dormant cancer cells under hypoxia using the $CoCl_2$-based *in vitro* platform

Based on the findings in Chapter 2, therapeutic approaches that target dormant cancer cells can be designed and tested using $CoCl_2$-based *in vitro* platform. The experimental results in Chapter 2 revealed that the upregulated p21 inhibited its target CDK2-cyclin complexes in dormant MCF-7 cells and led to cell cycle arrest in G0/G1 phase, which could allow dormant cancer cells to evade chemotherapy. It was previously found that p21 promotes cell cycle inhibition in response to anti-cancer drugs, protecting

cells from apoptosis as an active cell cycle is required to sense these drug and trigger apoptosis [201]. Furthermore, attenuation of p21 expression in chemotherapy-resistant renal cell carcinoma sensitized the cells to conventional chemotherapeutic agents. These finding suggests that inhibiting p21 in dormant cancer cells could be a therapeutic strategy that sensitizes dormant cancer cells to chemotherapeutic agents.

To this end, small molecules inhibiting p21 could be used in combination with chemotherapeutic agents. Butyrolactone I, a potent inhibitor of p21 blocks p53-dependent activation of p21 and subsequent G1/G0 cell cycle arrest in cancer cells exposed to DNA damaging agents [202]. Sorafenib also significantly decreased p21 in cancer cells treated with doxorubicin. When combined with paclitaxel or doxorubicin, sorafenib enhanced cytotoxicity of treatment, suggesting that sorafenib can act as a sensitizing agent for conventional chemotherapeutics in the treatment of dormant cancer cells [203]. Promoting proteolysis of p21 could be also considered. Newly synthesized p21 upon DNA damage is protected from proteosomal degradation by FKBPL (FK506-binding protein-like) [204]. It was previously shown that inhibition of FKBPL expression by its inhibitor geldanamycin significantly disrupted p21 stabilization after DNA damage. Thus, inhibitors of FKBPL could also sensitize the dormant cancer cells to chemotherapeutic agents.

Inhibition of p21 in dormant cancer cells could be also achieved by selectively targeting factors upstream or downstream of p21 that affect a particular aspect of p21 function. For example, MYC induces overexpression of AP4 (activating enhancer binding protein 4), which in turn inhibits p21-mediated cell cycle arrest and sensitizes cells to DNA damage-induced apoptosis [201]. MYC also represses the transcription of *CDKN1A*, which encodes p21, by binding to and inhibiting the Sp1 transcription factor [205]. MYC can be

activated by various mitogenic signals including serum stimulation or EGF (epidermal growth factor) via the MAPK/ERK pathway [206]. Thus, adding mitogenic signals in combination with chemotherapeutic agents may also effectively kill dormant cancer cells under hypoxia.

The function of p21 depends on its location within a cell. Cell cycle inhibition by p21 is associated with its nuclear localization, while cytoplasmic p21 activates the cell cycle by promoting the activity of CDK4/CDK6-cyclin D complexes [201]. Cytoplasmic accumulation of p21 is mediated by AKT1 kinase, which catalyzes the phosphorylation of p21. Since AKT1 is a downstream of HER2 (human epidermal growth factor receptor 2), cytoplasmic localization of p21 is observed in HER2-overexpressing cancer cells [207]. Thus, EGF-like ligands that bind to HER2 receptors could activate AKT1 kinase and sensitize dormant cancer cells to chemotherapeutic agents.

Taken altogether, upregulated p21 expression in dormant cancer cells under hypoxia can be potentially exploited for a targeted therapy that sensitize the dormant cells to conventional chemotherapy. The $CoCl_2$-based *in vitro* model will provide a platform for testing multiple strategies that could potentially inhibit p21 activation in dormant cancer cells, enabling the development of a combination therapy that could effectively kill dormant cancer cells.

5.2.3. *In situ* intravital imaging of hypoxic regulation of DTCs at metastatic sites

The *in vivo* platform using Co-PLG scaffolds, which is implantable in a subcutaneous region, could be used to provide easy access to various functional characterization, such as direct measurement of proliferation status of DTCs arriving at

hypoxic niches in metastatic organs. To this end, intravital imaging of engineered cancer cell lines via surgical engraftment of a skinfold window chamber above the Co-PLG scaffolds could be used. Oki et al. reported a modified fluorescence cell cycle indicator (FUCCI), developed by Sakaue-Sawano et al. [208], to effectively visualize G0, G1, and S/G2/M phases of the cell cycle for *in vivo* real time monitoring of cell proliferation status including quiescence [209]. Combined with intravital imaging, this modified FUCCI can visualize cancer cell dynamics including the transition between dormancy and proliferation, invasion, and metastasis. For instance, by using FUCCI and intravital imaging, Yano et al. found that cisplatin or paclitaxel killed only proliferating cancer cells in S and G2/M phases and had little effect on quiescent cancer cells in G0/G1 phase in liver tumors [210]. In addition, some of the quiescent cells in G0/G1 that evaded chemotherapy were found to resume proliferation by reentering the S and G2/M phases. Thus, intravital imaging of FUCCI-expressing DTCs arriving in Co-PLG scaffolds can directly visualize how hypoxia affects the cell fate of DTCs arriving at metastatic niches through the real time monitoring of cell cycle dynamics. This approach could be also used to test anti-cancer drugs targeting dormant DTCs in a hypoxic niche, as apoptosis can be also directly visualized *in situ* using a fluorescent probe [211]. Direct visualization of cell cycle dynamics and apoptosis of dormant DTCs in response to cancer drugs within the hypoxic niche could help design better therapeutic strategies to effectively destroy dormant cancer cells.

Alternatively, *ex vivo* imaging of the Co-PLG scaffold with a tissue clearing technique (CLARITY) [212] could be used to investigate dormant DTCs in a hypoxic niche. The actual number of DTCs recruited in the scaffolds is low, and the number of dormant DTCs is even lower. Thus, conventional immunohistostaining and flow cytometry are not able to effectively detect rare DTCs due to the technical difficulties of probing entire tissue

volumes and potential cell loss during tissue digestion. However, CLARITY, which optically clears fixed tissues, enables microscopic detection of rare DTCs while retaining spatial resolution in the tissue microenvironment as well as minimizing cell loss. Carpenter et al. demonstrated that tissue clearing enabled optical imaging of microporous hydrogel scaffolds harvested from mice, capturing cellular signatures of the tumor microenvironment including immune cells, rare DTCs, and vascular networks [212]. Therefore, direct visualization of dormant DTCs within a hypoxic niche using Co-PLG scaffolds and CLARITY could be used to investigate microenvironmental features of dormant niches including protein enrichment, vascular networks (e.g. perivascular niche), and spatial distribution of pro-dormancy cues. Given that current experimental metastasis models are not able to capture the hypoxia-DTC interactions that are critical to the therapeutic response of tumors, this approach may provide a greater understanding of how best to target DTCs in a hypoxic niche.

5.2.4. Incorporation of tumor targeting molecules onto GNR-PEG-Ce6 for effective sonodynamic therapy *in vivo*

For successful sonodynamic therapy *in vivo*, the efficient delivery of Ce6 is critical to provide sufficient concentration at the targeted disease site. However, targeted delivery of nanoparticles including GNR in animal models and patients remains a challenging hurdle for many researchers, even if they exhibit promising outcomes *in vitro*. In fact, the peritoneal cavity where GNR-PEG-Ce6 will be applied in ovarian cancer patients contains many vital organs that have to be protected from lethal sonodynamic effects of GNR-PEG-Ce6. To avoid off-target damage of these heathy tissues and organs in the peritoneal cavity and to concentrate sonodynamic effects onto ovarian cancer spheroids, addition of

targeting modalities to GNR-PEG-Ce6 can be considered. For example, folic acid functionalization is one of the common strategies employed for cancer cell targeting [213–215]. Many types of cancer including ovarian, uterine, and colon cancers overexpress folic acid binding proteins on the cell surface [213]. Lin et al. showed that doxorubicin (DOX) loaded onto folic acid-functionalized GO enhanced cytotoxicity toward OCM-1 human choroidal melanoma cells, while folic acid-GO exhibited significantly less cytotoxicity on ARPE-19 normal human retinal pigment epithelial cells after 24 h of incubation [214]. A similar cell-specific cytotoxic response was not observed for DOX loaded on GO without folic acid [214]. Importantly, folic acid-GO exhibited equivalent DOX loading capabilities as compared with bare GO. The folic acid-GO also selectively targeted and killed liver carcinoma HepG2 cells overexpressing folate receptors while not affecting healthy liver sinusoidal endothelial cells [215].

Targeting of other cancer cell surface receptors could also be used to enhance the cancer targeting ability of GNR-PEG-Ce6. Hyaluronic acid (HA) has been shown to target ovarian, breast, colon, and renal cancer cells overexpressing transmembrane glycoprotein CD44 [216]. Miao et al. reported that DOX loaded onto GO functionalized with cholesteryl HA (cHA-GO-DOX) exhibited 40.3% more cell death compared DOX loaded onto GO without cHA functionalization in KB epidermal carcinoma cells [217]. When subcutaneously injected into the mice bearing KB epidermal tumors, significant size reduction in tumor volume was observed after 24 days for cHA-GO-DOX compared with GO-DOX without cHA functionalization. Wu et al. also reported adipic acid dihydrazide (ADH)-HA-GO loaded with DOX where adipic acid was used to introduce amino groups for tethering HA to GO [218]. When ADH-HA-GO loaded with DOX was intravenously injected into the mice with subcutaneous HeLa tumors, it exhibited greater tumor inhibition

rates in mice compared with free DOX and GO-DOX. Song et al. found that cumulative DOX release from HA-GO-DOX was faster in the slightly acidic tumor environment at pH 5.3 than pH 7.4. This pH responsive release led to a 20% better tumor inhibition rate than free DOX and GO-DOX groups in H22 hepatic tumors in mice [219]. These findings suggest that addition of targeting molecules such as folic acid or HA to GNR-PEG-Ce6 could enhance selective delivery of Ce6 to ovarian cancer spheroids.

Targeting surface receptors that are overexpressed in ovarian cancer spheroids but not in mesothelial cells or other cells in the ascites could also be considered. Zhang et al. reported that ovarian cancer cells have high level expression of ROR1, a type I orphan-receptor tyrosine kinase-like surface protein, whereas ROR1 is not found on normal adult tissue, suggesting that ROR1 could be targeted for cancer cell-specific therapy [220]. Ziebarth et al. found that CD105 and CD106 were overexpressed in epithelial ovarian cancer cells or platinum-resistant ovarian cancer cells [221,222], whereas those molecules were expressed at low level son the surface of mesothelial cells [223]. Thus, incorporation of antibodies that bind to CD105 or CD106 onto GNR-PEG-Ce6 could be used to selectively target ovarian cancer spheroids.

Reference

[1] A.W. Lambert, D.R. Pattabiraman, R.A. Weinberg, Emerging Biological Principles of Metastasis, Cell. 168 (2017) 670–691.

[2] P. Mehlen, A. Puisieux, Metastasis: A question of life or death, Nat. Rev. Cancer. 6 (2006) 449–458.

[3] C.L. Chaffer, R.A. Weinberg, A perspective on cancer cell metastasis, Science. 331 (2011) 1559–1564.

[4] J.A. Aguirre-Ghiso, Models, mechanisms and clinical evidence for cancer dormancy, Nat. Rev. Cancer. 7 (2007) 834–846.

[5] National Cancer Institute, SEER Cancer Stat Facts: Female Breast Cancer, Seer.Cancer.Gov. (2018) 1. https://seer.cancer.gov/statfacts/html/breast.html (accessed January 13, 2020).

[6] E. Lengyel, Ovarian cancer development and metastasis, Am. J. Pathol. 177 (2010) 1053–1064.

[7] S.S. Li, J. Ma, A.S.T. Wong, Chemoresistance in ovarian cancer: Exploiting cancer stem cell metabolism, J. Gynecol. Oncol. 29 (2018) 1–11.

[8] Ovarian Cancer Research Alliance, Recurrence and Treatment, (n.d.). https://ocrahope.org/patients/about-ovarian-cancer/recurrence/ (accessed January 13, 2020).

[9] National Cancer Institute, SEER Cancer Stat Facts: Ovarian Cancer, Seer.Cancer.Gov. (2018) 1. https://seer.cancer.gov/statfacts/html/ovary.html (accessed January 13, 2020).

[10] S. Pradhan, J.L. Sperduto, C.J. Farino, et al., Engineered in Vitro Models of Tumor Dormancy and Reactivation, J. Biol. Eng. 12 (2018) 1–19.

[11] M. Banys, A.D. Hartkopf, N. Krawczyk, et al., Dormancy in breast cancer, Breast Cancer Targets Ther. 4 (2012) 183–191.

[12] C.A. Klein, Framework models of tumor dormancy from patient-derived observations, Curr. Opin. Genet. Dev. 21 (2011) 42–49.

[13] E. Butturini, A.C. de Prati, D. Boriero, et al., Tumor dormancy and interplay with hypoxic tumor microenvironment, Int. J. Mol. Sci. 20 (2019).

[14] N. Linde, G. Fluegen, J.A. Aguirre-Ghiso, The Relationship Between Dormant Cancer Cells and Their Microenvironment, 1st ed., Elsevier Inc., 2016.

[15] C. Morrissey, R.L. Vessella, P.H. Lange, et al., The biology and clinical implications of prostate cancer dormancy and metastasis, J. Mol. Med. 94 (2016) 259–265.

[16] C.M. Ghajar, H. Peinado, H. Mori, et al., The perivascular niche regulates breast tumour dormancy., Nat. Cell Biol. 15 (2013) 807–17.

[17] M.A. Lawson, M.M. McDonald, N. Kovacic, et al., Osteoclasts control reactivation of dormant myeloma cells by remodelling the endosteal niche, Nat. Commun. 6 (2015) 1–15.

[18] Y. Shiozawa, E.A. Pedersen, L.R. Patel, et al., GAS6/AXL axis regulates prostate cancer invasion, proliferation, and survival in the bone marrow niche, Neoplasia. 12 (2010) 116–127.

[19] R.S. Taichman, L.R. Patel, R. Bedenis, et al., GAS6 Receptor Status Is Associated with Dormancy and Bone Metastatic Tumor Formation, PLoS One. 8 (2013) 1–10.

[20] A. Mishra, J. Wang, Y. Shiozawa, et al., Hypoxia stabilizes GAS6/Axl signaling in metastatic prostate cancer, Mol. Cancer Res. 10 (2012) 703–712.

[21] R.W. Johnson, M.E. Sowder, A.J. Giaccia, Hypoxia and Bone Metastatic Disease, Curr. Osteoporos. Rep. 15 (2017) 231–238.

[22] R.W. Johnson, E.C. Finger, M.M. Olcina, et al., Induction of LIFR confers a dormancy phenotype in breast cancer cells disseminated to the bone marrow, Nat. Cell Biol. 18 (2016) 1078–1089.

[23] E.B. Rankin, A.J. Giaccia, Hypoxic control of metastasis, Science. 352 (2016) 175–180.

[24] E.B. Rankin, J.M. Nam, A.J. Giaccia, Hypoxia: Signaling the Metastatic Cascade, Trends in Cancer. 2 (2016) 295–304.

[25] G. Fluegen, A. Avivar-Valderas, Y. Wang, et al., Phenotypic heterogeneity of disseminated tumour cells is preset by primary tumour hypoxic microenvironments, Nat. Cell Biol. 19 (2017).

[26] A.R. Sertil, Hypoxia and tumor dormancy: Can the two tango?, Tumor Dormancy, Quiescence, Senescence Aging, Cancer, Noncancer Pathol. 3 (2014) 13–24.

[27] X.F. Li, J.A. O'Donoghue, Hypoxia in microscopic tumors, Cancer Lett. 264 (2008) 172–180.

[28] K. Bartkowiak, K.E. Effenberger, S. Harder, et al., Discovery of a novel unfolded protein response phenotype of cancer stem/progenitor cells from the bone marrow of breast cancer patients, J. Proteome Res. 9 (2010) 3158–3168.

[29] G. Fluegen, A. Avivar-Valderas, Y. Wang, et al., Phenotypic heterogeneity of disseminated tumour cells is preset by primary tumour hypoxic microenvironments, Nat. Cell Biol. 19 (2017) 120–132.

[30] S.S. Rao, R.V. Kondapaneni, A.A. Narkhede, Bioengineered models to study tumor dormancy, J. Biol. Eng. 13 (2019).

[31] H. Endo, H. Okuyama, M. Ohue, et al., Dormancy of cancer cells with suppression of AKT activity contributes to survival in chronic hypoxia, PLoS One. 9 (2014) 1–12.

[32] A. Carcereri de Prati, E. Butturini, A. Rigo, et al., Metastatic Breast Cancer Cells Enter Into Dormant State and Express Cancer Stem Cells Phenotype Under Chronic Hypoxia, J. Cell. Biochem. 118 (2017) 3237–3248.

[33] L.E. Huang, Z. Arany, D.M. Livingston, et al., Activation of hypoxia-inducible transcription factor depends primarily upon redox-sensitive stabilization of its α subunit, J. Biol. Chem. 271 (1996) 32253–32259.

[34] G. Martin, R. Andriamanalijaona, S. Grässel, et al., Effect of hypoxia and reoxygenation on gene expression and response to interleukin-1 in cultured articular chondrocytes, Arthritis Rheum. 50 (2004) 3549–3560.

[35] E.J. Wollen, P. Kwinta, M. Bik-Multanowski, et al., Hypoxia-reoxygenation affects whole-genome expression in the newborn eye, Investig. Ophthalmol. Vis. Sci. 55 (2014) 1393–1401.

[36] D. Wu, P. Yotnda, Induction and testing of hypoxia in cell culture., J. Vis. Exp. (2011) e2899.

[37] A.C.R. Epstein, J.M. Gleadle, L.A. McNeill, et al., C. elegans EGL-9 and mammalian homologs define a family of dioxygenases that regulate HIF by prolyl hydroxylation, Cell. 107 (2001) 43–54.

[38] Y. Yuan, G. Hilliard, T. Ferguson, et al., Cobalt inhibits the interaction between hypoxia-inducible factor-α and von Hippel-Lindau protein by direct binding to hypoxia-inducible factor-α, J. Biol. Chem. 278 (2003) 15911–15916.

[39] Y. Talukdar, J.T. Rashkow, G. Lalwani, et al., The effects of graphene nanostructures on mesenchymal stem cells, Biomaterials. 35 (2014) 4863–4877.

[40] S.M. Azarin, J. Yi, R.M. Gower, et al., In vivo capture and label-free detection of early metastatic cells, Nat. Commun. 6 (2015) 1–9.

[41] R.M. Gower, L.D. Shea, Biomaterial Scaffolds for Controlled, Localized Gene Delivery of Regenerative Factors, Adv. Wound Care. 2 (2013) 100–106.

[42] N. Ahmed, K.L. Stenvers, Getting to know ovarian cancer ascites: Opportunities for targeted therapy-based translational research, Front. Oncol. 3 SEP (2013) 1–12.

[43] E. Lou, R.I. Vogel, S. Hoostal, et al., Tumor-Stroma Proportion as a Predictive Biomarker of Resistance to Platinum-Based Chemotherapy in Patients With Ovarian Cancer, JAMA Oncol. 5 (2019) 1222–1224.

[44] Z. Lu, R.Z. Luo, Y. Lu, et al., The tumor suppressor gene ARHI regulates autophagy and tumor dormancy in human ovarian cancer cells, J. Clin. Invest. 118 (2008) 3917–3929.

[45] R.J.M. Correa, T. Peart, Y.R. Valdes, et al., Modulation of AKT activity is associated with reversible dormancy in ascites-derived epithelial ovarian cancer spheroids, Carcinogenesis. 33 (2012) 49–58.

[46] K.M. Burleson, R.C. Casey, K.M. Skubitz, et al., Ovarian carcinoma ascites spheroids adhere to extracellular matrix components and mesothelial cell monolayers, Gynecol. Oncol. 93 (2004) 170–181.

[47] R.C. Casey, K.M. Burleson, K.M. Skubitz, et al., B1-Integrins Regulate the Formation and Adhesion of Ovarian Carcinoma Multicellular Spheroids, Am. J. Pathol. 159 (2001) 2071–2080.

[48] M.P. Iwanicki, R.A. Davidowitz, M.R. Ng, et al., Ovarian cancer spheroids use myosin-generated force to clear the mesothelium, Cancer Discov. 1 (2011) 144–157.

[49] A.K. Mitra, K. Sawada, P. Tiwari, et al., Ligand-independent activation of c-Met by fibronectin and α5 B1-integrin regulates ovarian cancer invasion and metastasis, Oncogene. 30 (2011) 1566–1576.

[50] K.M. Bell-Mcguinn, C.M. Matthews, S.N. Ho, et al., A phase II, single-arm study of the anti-α5β1 integrin antibody volociximab as monotherapy in patients with platinum-resistant advanced epithelial ovarian or primary peritoneal cancer, Gynecol. Oncol. 121 (2011) 273–279.

[51] K. Sawada, A.K. Mitra, A.R. Radjabi, et al., Loss of E-cadherin promotes ovarian cancer metastasis via α5-integrin, which is a therapeutic target, Cancer Res. 68 (2008) 2329–2339.

[52] A. Levy, C. Leynes, M. Baig, et al., The Application of Biomaterials in the Treatment of Platinum-Resistant Ovarian Cancer, ChemMedChem. 14 (2019) 1810–1827.

[53] H. Tiwari, N. Karki, M. Pal, et al., Functionalized graphene oxide as a nanocarrier for dual drug delivery applications: The synergistic effect of quercetin and gefitinib against ovarian cancer cells, Colloids Surfaces B Biointerfaces. 178 (2019) 452–459.

[54] K.M. Burleson, L.K. Hansen, A.P.N. Skubitz, Ovarian carcinoma spheroids disaggregate on type I collagen and invade live human mesothelial cell monolayers, Clin. Exp. Metastasis. 21 (2005) 685–697.

[55] Y.J. Choi, S. Gurunathan, J.H. Kim, Graphene oxide-silver nanocomposite enhances cytotoxic and apoptotic potential of salinomycin in human ovarian cancer stem cells (OvCSCs): A novel approach for cancer therapy, Int. J. Mol. Sci. 19 (2018).

[56] B. Tian, C. Wang, S. Zhang, et al., Photothermally enhanced photodynamic therapy delivered by nano-graphene oxide, ACS Nano. 5 (2011) 7000–7009.

[57] P. Huang, C. Xu, J. Lin, et al., Folic Acid-conjugated Graphene Oxide loaded with Photosensitizers for Targeting Photodynamic Therapy, Theranostics. 1 (2012) 240–

250.

[58] C. Dai, S. Zhang, Z. Liu, et al., Two-Dimensional Graphene Augments Nanosonosensitized Sonocatalytic Tumor Eradication, ACS Nano. 11 (2017) 9467–9480.

[59] J.A. Aguirre-Ghiso, Models, mechanisms and clinical evidence for cancer dormancy., Nat. Rev. Cancer. 7 (2007) 834–846.

[60] S. Meng, D. Tripathy, E.P. Frenkel, et al., Circulating Tumor Cells in Patients with Breast Cancer Dormancy Circulating, Clin. Cancer Res. 10 (2004) 8152–8162.

[61] K. Pantel, C. Alix-Panabières, Tumour microenvironment: informing on minimal residual disease in solid tumours, Nat. Rev. Clin. Oncol. 14 (2017) 325–326.

[62] A.-G.J. Sosa MS, Bragado P, Debnath J, Systems Biology of Tumor Dormancy, Adv. Exp. Med. Biol. 734 (2013) 73–89.

[63] P. Bragado, M.S. Sosa, P. Keely, et al., Microenvironments dictating tumor cell dormancy, Recent Results Cancer Res. 195 (2012) 25–39.

[64] R. Marlow, G. Honeth, S. Lombardi, et al., A novel model of dormancy for bone metastatic breast cancer cells, Cancer Res. 73 (2013) 6886–6899.

[65] B. Psaila, D. Lyden, The metastatic niche: adapting the foreign soil., Nat. Rev. Cancer. 9 (2009) 285–293.

[66] K. Bartkowiak, K.E. Effenberger, S. Harder, et al., Discovery of a novel unfolded protein response phenotype of cancer stem/progenitor cells from the bone marrow of breast cancer patients, J. Proteome Res. 9 (2010) 3158–3168.

[67] R.S. Kim, A. Avivar-Valderas, Y. Estrada, et al., Dormancy signatures and metastasis in estrogen receptor positive and negative breast cancer, PLoS One. 7 (2012) 1–8.

[68] R.W. Johnson, E.C. Finger, M.M. Olcina, et al., Induction of LIFR confers a dormancy phenotype in breast cancer cells disseminated to the bone marrow, Nat. Cell Biol. 18 (2016) 1078–1089.

[69] M.S. Al Okail, Cobalt chloride, a chemical inducer of hypoxia-inducible factor-1α in U251 human glioblastoma cell line, J. Saudi Chem. Soc. 14 (2010) 197–201.

[70] A.C.R. Epstein, J.M. Gleadle, L.A. McNeill, et al., C. elegans EGL-9 and mammalian homologs define a family of dioxygenases that regulate HIF by prolyl hydroxylation, Cell. 107 (2001) 43–54.

[71] S.P.. D. and H.. F.B. Mark A . Goldberg, Regulation of the Erythropoietin Gene : Evidence that the Oxygen Sensor is a Heme Protein, Science. 242 (1988) 1412–1415.

[72] Ebert, B. L., Firth, J.D., Ratcliffe, P.J., Hypoxia and Mitochondrial Inhibitors Regulate Expression of Glucose Transporter-1 via Distinct Cis-acting Sequences, J. Biol. Chem. 270 (1995) 29083–29089.

[73] B.L. Ebert, J.M. Gleadle, J.F. O'Rourke, et al., Isoenzyme-specific regulation of genes involved in energy metabolism by hypoxia: similarities with the regulation of erythropoietin., Biochem. J. 313 (Pt 3) (1996) 809–814.

[74] Q. Ao, W. Su, S. Guo, et al., SENP1 desensitizes hypoxic ovarian cancer cells to cisplatin by up-regulating HIF-1α., Sci. Rep. 5 (2015) 16396.

[75] W.G. An, M. Kanekal, M.C. Simon, et al., Stabilization of wild-type p53 by hypoxia-inducible factor 1α., Nature. 392 (1998) 405–408.

[76] P. Bragado, Y. Estrada, F. Parikh, et al., TGF-β2 dictates disseminated tumour cell fate in target organs through TGF-β-RIII and p38α/β signalling, Nat. Cell Biol. 15 (2013) 1351–1361.

[77] S. Bruno, Z. Darzynkiewicz, Cell cycle dependent expression and stability of the nuclear protein detected by Ki-67 antibody in HL-60 cells, Cell Prolif. 25 (1992) 31–40.

[78] T. Scholzen, J. Gerdes, The Ki-67 protein: from the known and the unknown, J. Cell. Physiol. 182 (2000) 311–322.

[79] D. Páez, M.J. Labonte, P. Bohanes, et al., Cancer dormancy: A model of early dissemination and late cancer recurrence, Clin. Cancer Res. 18 (2012) 645–653.

[80] S.-H. Wang, S.-Y. Lin, Tumor dormancy: potential therapeutic target in tumor recurrence and metastasis prevention., Exp. Hematol. Oncol. 2 (2013) 29.

[81] H. Harrison, L. Rogerson, H.J. Gregson, et al., Contrasting Hypoxic Effects on Breast Cancer Stem Cell Hierarchy Is Dependent on ER- Status, Cancer Res. 73 (2013) 1420–1433.

[82] M.S. Sosa, A. Avivar-Valderas, P. Bragado, et al., ERK1/2 and p38α/β signaling in tumor cell quiescence: Opportunities to control dormant residual disease, Clin. Cancer Res. 17 (2011) 5850–5857.

[83] T. Abbas, A. Dutta, P21 in Cancer: Intricate Networks and Multiple Activities, Nat. Rev. Cancer. 9 (2009) 400–414.

[84] L.E. Huang, Carrot and stick: HIF-α engages c-Myc in hypoxic adaptation, Cell Death Differ. 15 (2008) 672–677.

[85] K.N. Weilbaecher, T.A. Guise, L.K. McCauley, Cancer to bone: a fatal attraction, Nat. Rev. Cancer. 11 (2011) 411–425.

[86] H. Gao, G. Chakraborty, A.P. Lee-Lim, et al., The BMP Inhibitor Coco Induces Breast Cancer Cells to Undergo Reactivation at Lung Metastatic sites, Cell. 150

(2012) 764–779.

[87] R. Du, K. V. Lu, C. Petritsch, et al., HIF1α Induces the Recruitment of Bone Marrow-Derived Vascular Modulatory Cells to Regulate Tumor Angiogenesis and Invasion, Cancer Cell. 13 (2008) 206–220.

[88] L. Yu, C.A. Hales, Long-term exposure to hypoxia inhibits tumor progression of lung cancer in rats and mice, BMC Cancer. 11 (2011) 331.

[89] M. Padró, R.J. Louie, B. V. Lananna, et al., Genome-independent hypoxic repression of estrogen receptor alpha in breast cancer cells, BMC Cancer. 17 (2017) 203.

[90] H. Zhang, M. Bosch-Marce, L.A. Shimoda, et al., Mitochondrial autophagy is an HIF-1-dependent adaptive metabolic response to hypoxia, J. Biol. Chem. 283 (2008) 10892–10903.

[91] Z. Lu, R.Z. Luo, Y. Lu, et al., The tumor suppressor gene ARHI regulates autophagy and tumour dormancy in human ovarian cancer cells, Cell Prolif. 118 (2008) 3917–3929.

[92] J.A. Hickson, D. Huo, D.J. Vander Griend, et al., The p38 kinases MKK4 and MKK6 suppress metastatic colonization in human ovarian carcinoma, Cancer Res. 66 (2006) 2264–2270.

[93] K. Yamamoto, S. Inoue, A. Yamazaki, et al., Site-Specific DNA Damage Induced by Cobalt(II) Ion and Hydrogen Peroxide: Role of Singlet Oxygen, Chem. Res. Toxicol. 2 (1989) 234–239.

[94] S.X. Chen F, Ding M, Castranova V, Carcinogenic metals and NF-κB activation, Mol Cell Biochem. (2001) 159–171.

[95] H. Axelson, E. Fredlund, M. Ovenberger, et al., Hypoxia-induced dedifferentiation of tumor cells - A mechanism behind heterogeneity and aggressiveness of solid tumors, Semin. Cell Dev. Biol. 16 (2005) 554–563.

[96] J.L. Gooch, R.E. Herrera, D. Yee, The role of p21 in interferon gamma-mediated growth inhibition of human breast cancer cells, Cell Growth Differ. 11 (2000) 335–342.

[97] M. Shanmugam, N.L. Krett, E.T. Maizels, et al., A role for protein kinase C δ in the differential sensitivity of MCF-7 and MDA-MB-231 human breast cancer cells to phorbol ester-induced growth arrest and p21 WAFI / CIP1 induction, 172 (2001) 43–53.

[98] M. Koshiji, Y. Kageyama, E.A. Pete, et al., HIF-1α induces cell cycle arrest by functionally counteracting Myc, EMBO J. 23 (2004) 1949–1956.

[99] S.L. Green, R.A. Freiberg, A.J. Giaccia, p21 Cip1 and p27 Kip1 Regulate Cell Cycle Reentry after Hypoxic Stress but Are Not Necessary for Hypoxia-Induced Arrest,

21 (2001) 1196–1206.

[100] R. Edmondson, J.J. Broglie, A.F. Adcock, et al., Three-Dimensional Cell Culture Systems and Their Applications in Drug Discovery and Cell-Based Biosensors, Assay Drug Dev. Technol. 12 (2014) 207–218.

[101] R. Wang, F. Jin, H. Zhong, A novel experimental hypoxia chamber for cell culture., Am. J. Cancer Res. 4 (2014) 53–60.

[102] W.R. Wilson, M.P. Hay, Targeting hypoxia in cancer therapy, Nat. Rev. Cancer. 11 (2011) 393–410.

[103] P. Vaupel, A. Mayer, Hypoxia in cancer: Significance and impact on clinical outcome, Cancer Metastasis Rev. 26 (2007) 225–239.

[104] E.L. LaGory, A.J. Giaccia, The ever-expanding role of HIF in tumour and stromal biology, Nat. Cell Biol. 18 (2016) 356–365.

[105] J.T. Erler, K.L. Bennewith, T.R. Cox, et al., Hypoxia-Induced Lysyl Oxidase Is a Critical Mediator of Bone Marrow Cell Recruitment to Form the Premetastatic Niche, Cancer Cell. 15 (2009) 35–44.

[106] W.R. Martin Brown, J., Wilson, Exploiting tumour hypoxia in cancer treatment, Nat. Rev. Cancer. 4 (2004) 437–447.

[107] E.B. Rankin, J.-M. Nam, A.J. Giaccia, Hypoxia: Signaling the Metastatic Cascade, Trends Cancer. 2 (2016) 295–304.

[108] G. Fluegen, A. Avivar-Valderas, Y. Wang, et al., Phenotypic heterogeneity of disseminated tumour cells is preset by primary tumour hypoxic microenvironments, Nat. Cell Biol. 19 (2017) 120–132.

[109] E.B. Rankin, A.J. Giaccia, Hypoxic control of metastasis, Science. 352 (2017) 175–180.

[110] C.C.-L. Wong, D.M. Gilkes, H. Zhang, et al., Hypoxia-inducible factor 1 is a master regulator of breast cancer metastatic niche formation., Proc. Natl. Acad. Sci. U. S. A. 108 (2011) 16369–74.

[111] J.T. Erler, K.L. Bennewith, M. Nicolau, et al., Lysyl oxidase is essential for hypoxia-induced metastasis, Nature. 440 (2006) 1222–1226.

[112] R.W. Johnson, M.E. Sowder, A.J. Giaccia, Hypoxia and Bone Metastatic Disease, Curr. Osteoporos. Rep. 15 (2017) 231–238.

[113] G.Z. Qiu, M.Z. Jin, J.X. Dai, et al., Reprogramming of the Tumor in the Hypoxic Niche: The Emerging Concept and Associated Therapeutic Strategies, Trends Pharmacol. Sci. 38 (2017) 669–686.

[114] F. Dupuy, S. Tabariès, S. Andrzejewski, et al., PDK1-dependent metabolic

reprogramming dictates metastatic potential in breast cancer, Cell Metab. 22 (2015) 577–589.

[115] A.R. Nobre, D. Entenberg, Y. Wang, et al., The Different Routes to Metastasis via Hypoxia-Regulated Programs, Trends Cell Biol. 28 (2018) 941–956.

[116] L. Holmgren, M.S. O'reilly, J. Folkman, Dormancy of micrometastases: Balanced proliferation and apoptosis in the presence of angiogenesis suppression, Nat. Med. 1 (1995) 149–153.

[117] S. Rafii, D. Lyden, R. Benezra, et al., Vascular and haematopoietic stem cells: Novel targets for anti-angiogenesis therapy?, Nat. Rev. Cancer. 2 (2002) 826–835.

[118] B. Psaila, D. Lyden, The Metastatic Niche: Adapting the Foreign Soil, Nat. Rev. Cancer. 9 (2009) 285–293.

[119] J.A. Joyce, J.W. Pollard, Microenvironmental regulation of metastasis, Nat. Rev. Cancer. 9 (2009) 239–252.

[120] D.F. Quail, J.A. Joyce, Microenvironmental regulation of tumor progression and metastasis, Nat. Med. 19 (2013) 1423–1437.

[121] B.A. Aguado, G.G. Bushnell, S.S. Rao, et al., Engineering the pre-metastatic niche, Nat. Biomed. Eng. 1 (2017) 1–12.

[122] S. Koscielny, M. Tubiana, Parallel progression of tumour and metastases., Nat. Rev. Cancer. 10 (2010) 156.

[123] H. Peinado, H. Zhang, I.R. Matei, et al., Pre-metastatic niches: Organ-specific homes for metastases, Nat. Rev. Cancer. 17 (2017) 302–317.

[124] R.A. Carpenter, J.-G. Kwak, S.R. Peyton, et al., Implantable pre-metastatic niches for the study of the microenvironmental regulation of disseminated human tumour cells, Nat. Biomed. Eng. 2 (2018) 915–929.

[125] J. Lee, M. Li, J. Milwid, et al., Implantable microenvironments to attract hematopoietic stem/cancer cells, Proc. Natl. Acad. Sci. 109 (2012) 19638–19643.

[126] F. Bersani, J. Lee, M. Yu, et al., Bioengineered implantable scaffolds as a tool to study stromal-derived factors in metastatic cancer models, Cancer Res. 74 (2014) 7229–7238.

[127] S.S. Rao, G.G. Bushnell, S.M. Azarin, et al., Enhanced survival with implantable scaffolds that capture metastatic breast cancer cells in vivo, Cancer Res. 76 (2016) 5209–5218.

[128] K.M. Park, S. Gerecht, Hypoxia-inducible hydrogels, Nat. Commun. 5 (2014) 1–12.

[129] E. Quinlan, S. Partap, M.M. Azevedo, et al., Hypoxia-mimicking bioactive glass/collagen glycosaminoglycan composite scaffolds to enhance angiogenesis and

bone repair, Biomaterials. 52 (2015) 358–366.

[130] Q. Yao, Y. Liu, J. Tao, et al., Hypoxia-Mimicking Nanofibrous Scaffolds Promote Endogenous Bone Regeneration, ACS Appl. Mater. Interfaces. 8 (2016) 32450–32459.

[131] C. Wu, Y. Zhou, W. Fan, et al., Hypoxia-mimicking mesoporous bioactive glass scaffolds with controllable cobalt ion release for bone tissue engineering, Biomaterials. 33 (2012) 2076–2085.

[132] H.R. Lee, F. Leslie, S.M. Azarin, A facile in vitro platform to study cancer cell dormancy under hypoxic microenvironments using CoCl2, J. Biol. Eng. 12 (2018) 1–15.

[133] B.L. Ebert, J.M. Gleadle, J.F.O. Rourke, et al., Isoenzyme-specific regulation of genes involved in energy metabolism by hypoxia: similarities with the regulation of erythropoietin, 313 (1996) 809–814.

[134] A. Namiki, E. Brogi, M. Kearney, et al., Hypoxia induces vascular endothelial growth factor in cultured human endothelial cells., J. Biol. Chem. 270 (1995) 31189–95.

[135] Y. Yuan, G. Hilliard, T. Ferguson, et al., Cobalt inhibits the interaction between hypoxia-inducible factor-α and von Hippel-Lindau protein by direct binding to hypoxia-inducible factor-α, J. Biol. Chem. 278 (2003) 15911–15916.

[136] B.A. Aguado, J.J. Wu, S.M. Azarin, et al., Secretome identification of immune cell factors mediating metastatic cell homing, Sci. Rep. 5 (2015) 17566.

[137] A. Faustino-Rocha, P.A. Oliveira, J. Pinho-Oliveira, et al., Estimation of rat mammary tumor volume using caliper and ultrasonography measurements, Lab Anim. (NY). 42 (2013) 217–224.

[138] F. Pelaez, N. Manuchehrabadi, P. Roy, et al., Biomaterial scaffolds for non-invasive focal hyperthermia as a potential tool to ablate metastatic cancer cells, Biomaterials. 166 (2018) 27–37.

[139] M.M. Azevedo, G. Jell, M.D. O'Donnell, et al., Synthesis and characterization of hypoxia-mimicking bioactive glasses for skeletal regeneration, J. Mater. Chem. 20 (2010) 8854–8864.

[140] B. Lee, Ji-Won; Seong-Hui, J.-W.J.S.-H.K. and K.-W. Kim, Hypoxia-inducible factor (HIF-1), Exp. Mol. Med. 36 (2004) 1–12.

[141] G.L. Semenza, Hypoxia-inducible factor 1: master regulator of O2 homeostasis, Curr Opin Genet Dev. 8 (1998) 588–594.

[142] A.J. Majmundar, W.J. Wong, M.C. Simon, Hypoxia-Inducible Factors and the Response to Hypoxic Stress, Mol. Cell. 40 (2010) 294–309.

[143] B. Keith, M.C. Simon, Hypoxia-Inducible Factors, Stem Cells, and Cancer, Cell. 129 (2007) 465–472.

[144] W.R.H. Chilov D., Camenisch G., Kvietikova I., Ziegler U., Gassmann M., Induction and nuclear translocation of hypoxia-inducible factor-1 (HIF-1): heterodimerization with ARNT is not necessary for nuclear accumulation of HIF-1α, J Cell Sci. 112 (1999) 1203–1212.

[145] D. Huang, C. Li, H. Zhang, Hypoxia and cancer cell metabolism HIF-1 and Warburg Effect HIF-1 and Lipid Metabolism in Cancer Cells, Acta Biochim. Biophys. Sin. (Shanghai). 46 (2014) 214–219.

[146] C.W. Pugh, P.J. Ratcliffe, Regulation of angiogenesis by hypoxia: role of the HIF system, Nat. Med. 9 (2003) 677–648.

[147] B.L. Krock, N. Skuli, M.C. Simon, Hypoxia-Induced Angiogenesis: Good and Evil, Genes Cancer. 2 (2011) 1117–1133.

[148] H.T. Yuan, E. V. Khankin, S.A. Karumanchi, et al., Angiopoietin 2 Is a Partial Agonist/Antagonist of Tie2 Signaling in the Endothelium, Mol. Cell. Biol. 29 (2009) 2011–2022.

[149] E.L. Lund, A. Høg, M.W.B. Olsen, et al., Differential regulation of VEGF, HIF1α and angiopoietin-1, -2 and -4 by hypoxia and ionizing radiation in human glioblastoma, Int. J. Cancer. 108 (2004) 833–838.

[150] G. Krikun, F. Schatz, T. Finlay, et al., Expression of angiopoietin-2 by human endometrial endothelial cells: Regulation by hypoxia and inflammation, Biochem. Biophys. Res. Commun. 275 (2000) 159–163.

[151] H.-P. Gerber, F. Condorelli, J. Park, et al., Differential regulation of the two vascular endothelial growth factor receptor genes, J. Biol. Chem. 272 (1997) 23659–23667.

[152] P. Pichiule, J.C. Chavez, J.C. LaManna, Hypoxic Regulation of Angiopoietin-2 Expression in Endothelial Cells, J. Biol. Chem. 279 (2004) 12171–12180.

[153] S. Al-Maawi, A. Orlowska, R. Sader, et al., In vivo cellular reactions to different biomaterials—Physiological and pathological aspects and their consequences, Semin. Immunol. 29 (2017) 49–61.

[154] Q. Yao, Y. Liu, J. Tao, et al., Hypoxia-Mimicking Nanofibrous Scaffolds Promote Endogenous Bone Regeneration, J Biomed Mater Res Part A. 104 (2016) 2515–2527.

[155] P. Jia, H. Chen, H. Kang, et al., Deferoxamine released from poly(lactic-co-glycolic acid) promotes healing of osteoporotic bone defect via enhanced angiogenesis and osteogenesis, J. Biomed. Mater. Res. - Part A. 104 (2016) 2515–2527.

[156] M.B. Asparuhova, C. Secondini, C. Rüegg, et al., Mechanism of irradiation-induced mammary cancer metastasis: A role for SAP-dependent Mkl1 signaling, Mol. Oncol.

9 (2015) 1510–1527.

[157] B.A. Aguado, J.R. Caffe, D. Nanavati, et al., Extracellular matrix mediators of metastatic cell colonization characterized using scaffold mimics of the pre-metastatic niche, Acta Biomater. 33 (2016) 13–24.

[158] E. Lengyel, Ovarian cancer development and metastasis, Am. J. Pathol. 177 (2010) 1053–1064.

[159] D.S. Tan, R. Agarwal, S.B. Kaye, Mechanisms of transcoelomic metastasis in ovarian cancer, Lancet Oncol. 7 (2006) 925–934.

[160] L. Moffitt, N. Karimnia, A. Stephens, et al., Therapeutic targeting of collective invasion in Ovarian cancer, Int. J. Mol. Sci. 20 (2019) 1–17.

[161] R.C. Casey, K.M. Burleson, K.M. Skubitz, et al., β1-Integrins Regulate the Formation and Adhesion of Ovarian Carcinoma Multicellular Spheroids, Am. J. Pathol. 159 (2001) 2071–2080.

[162] S.M. Chowdhury, C. Surhland, Z. Sanchez, et al., Graphene nanoribbons as a drug delivery agent for lucanthone mediated therapy of glioblastoma multiforme, Nanomedicine Nanotechnology, Biol. Med. 11 (2015) 109–118.

[163] S.C. Patel, S. Lee, G. Lalwani, et al., Graphene-based platforms for cancer therapeutics, Ther. Deliv. 7 (2016) 101–116.

[164] Z. Liu, J.T. Robinson, X. Sun, et al., PEGylated nanographene oxide for delivery of water-insoluble cancer drugs, J. Am. Chem. Soc. 130 (2008) 10876–10877.

[165] Y.J. Lu, C.W. Lin, H.W. Yang, et al., Biodistribution of PEGylated graphene oxide nanoribbons and their application in cancer chemo-photothermal therapy, Carbon N. Y. 74 (2014) 83–95.

[166] X. Shi, H. Chang, S. Chen, et al., Regulating cellular behavior on few-layer reduced graphene oxide films with well-controlled reduction states, Adv. Funct. Mater. 22 (2012) 751–759.

[167] J. Park, B. Kim, J. Han, et al., Graphene oxide flakes as a cellular adhesive: Prevention of reactive oxygen species mediated death of implanted cells for cardiac repair, ACS Nano. 9 (2015) 4987–4999.

[168] S. Kang, J. Lee, S. Ryu, et al., Gold Nanoparticle/Graphene Oxide Hybrid Sheets Attached on Mesenchymal Stem Cells for Effective Photothermal Cancer Therapy, Chem. Mater. 29 (2017) 3461–3476.

[169] X. Yang, X. Zhang, Z. Liu, et al., High-efficiency loading and controlled release of doxorubicin hydrochloride on graphene oxide, J. Phys. Chem. C. 112 (2008) 17554–17558.

[170] Z. Liu, X. Sun, N. Nakayama-Ratchford, et al., Supramolecular chemistry on water-

Soluble carbon nanotubes for drug loading and delivery, ACS Nano. 1 (2007) 50–56.

[171] S. Mullick Chowdhury, S. Zafar, V. Tellez, et al., Graphene Nanoribbon-Based Platform for Highly Efficacious Nuclear Gene Delivery, ACS Biomater. Sci. Eng. 2 (2016) 798–808.

[172] C. Dai, S. Zhang, Z. Liu, et al., Two-Dimensional Graphene Augments Nanosonosensitized Sonocatalytic Tumor Eradication, ACS Nano. 11 (2017) 9467–9480.

[173] K. Yang, L. Hu, X. Ma, et al., Multimodal imaging guided photothermal therapy using functionalized graphene nanosheets anchored with magnetic nanoparticles, Adv. Mater. 24 (2012) 1868–1872.

[174] Y. Li, H. Dong, Y. Li, et al., Graphene-based nanovehicles for photodynamic medical therapy, Int. J. Nanomedicine. 10 (2015) 2451–2459.

[175] Y.W. Chen, T.Y. Liu, P.H. Chang, et al., A theranostic nrGO@MSN-ION nanocarrier developed to enhance the combination effect of sonodynamic therapy and ultrasound hyperthermia for treating tumor, Nanoscale. 8 (2016) 12648–12657.

[176] A.M. Dimiev, J.M. Tour, Mechanism of graphene oxide formation, ACS Nano. 8 (2014) 3060–3068.

[177] D. V. Kosynkin, A.L. Higginbotham, A. Sinitskii, et al., Longitudinal unzipping of carbon nanotubes to form graphene nanoribbons, Nature. 458 (2009) 872–876.

[178] E.R. Fischer, B.T. Hansen, V. Nair, et al., Scanning electron microscopy, Curr Protoc Microbiol. 25 (2012) 2B.2.1-2B.2.47.

[179] H.R. Lee, F. Pelaez, A.M. Silbaugh, et al., Biomaterial Platform To Establish a Hypoxic Metastatic Niche in Vivo, ACS Appl. Bio Mater. 2 (2019) 1549–1560.

[180] J. Fogh, G. Trempe, New Human Tumor Cell Lines, in: Hum. Tumor Cells Vitr., 1975.

[181] E.A. White, H.A. Kenny, E. Lengyel, Three-dimensional modeling of ovarian cancer, Adv. Drug Deliv. Rev. 79 (2014) 184–192.

[182] K. Lawrenson, B. Grun, S.A. Gayther, Heterotypic three-dimensional in vitro modeling of stromal-epithelial interactions during ovarian cancer initiation and progression, J. Vis. Exp. (2012) 1–8.

[183] H. Shi, Q. Liu, X. Qin, et al., Pharmacokinetic study of a novel sonosensitizer chlorin-e6 and its sonodynamic anti-cancer activity in hepatoma-22 tumor-bearing mice, Biopharm. Drug Dispos. 32 (2011) 319–332.

[184] Y. Li, P. Wang, X. Wang, et al., Involvement of mitochondrial and reactive oxygen species in the sonodynamic toxicity of chlorin e6 in human leukemia K562 cells,

Ultrasound Med. Biol. 40 (2014) 990–1000.

[185] Q. Li, X. Wang, P. Wang, et al., Efficacy of chlorin e6-mediated sono-photodynamic therapy on 4T1 cells, Cancer Biother. Radiopharm. 29 (2014) 42–52.

[186] H. Wang, X. Wang, P. Wang, et al., Ultrasound enhances the efficacy of chlorin E6-mediated photodynamic therapy in MDA-MB-231 Cells, Ultrasound Med. Biol. 39 (2013) 1713–1724.

[187] G.Y. Wan, Y. Liu, B.W. Chen, et al., Recent advances of sonodynamic therapy in cancer treatment, Cancer Biol. Med. 13 (2016) 325–338.

[188] T. Masiello, A. Dhall, L. Hemachandra, et al., A Dynamic Culture Method to Produce Ovarian Cancer Spheroids under Physiologically-Relevant Shear Stress, Cells. 7 (2018) 277.

[189] I. Rizvi, U.A. Gurkan, S. Tasoglu, et al., Flow induces epithelial-mesenchymal transition, cellular heterogeneity and biomarker modulation in 3D ovarian cancer nodules, Proc. Natl. Acad. Sci. U. S. A. 110 (2013).

[190] L. Avraham-Chakim, D. Elad, U. Zaretsky, et al., Fluid-Flow Induced Wall Shear Stress and Epithelial Ovarian Cancer Peritoneal Spreading, PLoS One. 8 (2013) 0–8.

[191] H.A. Kenny, K.M. Nieman, A.K. Mitra, et al., The first line of intra-abdominal metastatic attack: Breaching the mesothelial cell layer, Cancer Discov. 1 (2011) 100–102.

[192] M.P. Iwanicki, R.A. Davidowitz, M.R. Ng, et al., Ovarian cancer spheroids use myosin-generated force to clear the mesothelium, Cancer Discov. 1 (2011) 144–157.

[193] W. Mcguire Iii, M. Markman, Primary ovarian cancer chemotherapy: current standards of care, Br. J. Cancer. 89 (2003) 3–8.

[194] K. Shield, M.L. Ackland, N. Ahmed, et al., Multicellular spheroids in ovarian cancer metastases: Biology and pathology, Gynecol. Oncol. 113 (2009) 143–148.

[195] G. Mehta, A.Y. Hsiao, M. Ingram, et al., Opportunities and challenges for use of tumor spheroids as models to test drug delivery and efficacy, J. Control. Release. 164 (2012) 192–204.

[196] S.K. Green, G. Francia, C. Isidoro, et al., Antiadhesive antibodies targeting E-cadherin sensitize multicellular tumor spheroids to chemotherapy in vitro, Mol. Cancer Ther. 3 (2004) 149–159.

[197] E. Sokolova, O. Kutova, A. Grishina, et al., Penetration efficiency of antitumor agents in ovarian cancer spheroids: The case of recombinant targeted toxin DARPin-LoPE and the chemotherapy drug, doxorubicin, Pharmaceutics. 11 (2019).

[198] I. Beyer, H. Cao, J. Persson, et al., Coadministration of epithelial junction opener

JO-1 improves the efficacy and safety of chemotherapeutic drugs, Clin. Cancer Res. 18 (2012) 3340–3351.

[199] I.F. Tannock, C.M. Lee, J.K. Tunggal, et al., Limited penetration of anticancer drugs through tumor tissue: A potential cause of resistance of solid tumors to chemotherapy, Clin. Cancer Res. 8 (2002) 878–884.

[200] W. Fayad, S. Brnjic, D. Berglind, et al., Restriction of cisplatin induction of acute apoptosis to a subpopulation of cells in a three-dimensional carcinoma culture model, Int. J. Cancer. 125 (2009) 2450–2455.

[201] T. Abbas, A. Dutta, P21 in cancer: Intricate networks and multiple activities, Nat. Rev. Cancer. 9 (2009) 400–414.

[202] R. Liu, H.I. Wettersten, S.-H. Park, et al., Small-molecule inhibitors of p21 as novel therapeutics for chemotherapy-resistant kidney cancer, Futur. Med Chem. 5 (2013) 991–994.

[203] H. Inoue, S.H. Hwang, A.T. Wecksler, et al., Sorafenib attenuates p21 in kidney cancer cells and augments cell death in combination with DNA-damaging chemotherapy, Cancer Biol. Ther. 12 (2011) 827–836.

[204] T. Jascur, H. Brickner, I. Salles-Passador, et al., Regulation of p21WAF1/CIP1 stability by WISp39, a Hsp90 binding TPR protein, Mol. Cell. 17 (2005) 237–249.

[205] A.L. Gartel, K. Shchors, Mechanisms of c-myc-mediated transcriptional repression of growth arrest genes, Exp. Cell Res. 283 (2003) 17–21.

[206] J. Campisi, H.E. Gray, A.B. Pardee, et al., Cell-cycle control of c-myc but not c-ras expression is lost following chemical transformation, Cell. 36 (1984) 241–247.

[207] B.P. Zhou, Y. Liao, W. Xia, et al., Cytoplasmic localization of p21 CIP1/WAF1 by Akt-induced phosphorylation in HER-2/neu-overexpressing cells, Nat. Cell Biol. 3 (2001) 245–252.

[208] A. Sakaue-Sawano, H. Kurokawa, T. Morimura, et al., Visualizing Spatiotemporal Dynamics of Multicellular Cell-Cycle Progression, Cell. 132 (2008) 487–498.

[209] T. Oki, K. Nishimura, J. Kitaura, et al., A novel cell-cycle-indicator, mVenus-p27K 2 , identifies quiescent cells and visualizes G0–G1 transition, Sci. Rep. (2014) 4012.

[210] S. Yano, Y. Zhang, S. Miwa, et al., Spatial-temporal FUCCI imaging of each cell in a tumor demonstrates locational dependence of cell cycle dynamics and chemoresponsiveness, Cell Cycle. 13 (2014) 2110–2119.

[211] A. Xiao, A.E. Gibbons, K.E. Luker, et al., Fluorescence Lifetime Imaging of Apoptosis, Tomography. 1 (2015) 115–124.

[212] R.A. Carpenter, J.G. Kwak, S.R. Peyton, et al., Implantable pre-metastatic niches for the study of the microenvironmental regulation of disseminated human tumour

cells, Nat. Biomed. Eng. 2 (2018) 915–929.

[213] J.F. Ross, P.K. Chaudhuri, M. Ratnam, Differential regulation of folate receptor isoforms in normal and malignant tissues in vivo and in established cell lines. Physiologic and clinical implications, Cancer. 73 (1994) 2432–2443.

[214] Q. Lin, X. Huang, J. Tang, et al., Environmentally friendly, one-pot synthesis of folic acid-decorated graphene oxide-based drug delivery system, J. Nanoparticle Res. 15 (2013).

[215] X. Zhao, P. Liu, Biocompatible graphene oxide as a folate receptor-targeting drug delivery system for the controlled release of anti-cancer drugs, RSC Adv. 4 (2014) 24232–24239.

[216] A.K. Yadav, P. Mishra, G.P. Agrawal, An insight on hyaluronic acid in drug targeting and drug delivery, J. Drug Target. 16 (2008) 91–107.

[217] W. Miao, G. Shim, C.M. Kang, et al., Cholesteryl hyaluronic acid-coated, reduced graphene oxide nanosheets for anti-cancer drug delivery, Biomaterials. 34 (2013) 9638–9647.

[218] H. Wu, H. Shi, Y. Wang, et al., Hyaluronic acid conjugated graphene oxide for targeted drug delivery, Carbon N. Y. 69 (2014) 379–389.

[219] E. Song, W. Han, C. Li, et al., Hyaluronic acid-decorated graphene oxide nanohybrids as nanocarriers for targeted and pH-responsive anticancer drug delivery, ACS Appl. Mater. Interfaces. 6 (2014) 11882–11890.

[220] S. Zhang, B. Cui, H. Lai, et al., Ovarian cancer stem cells express ROR1, which can be targeted for anti -cancer-stem-cell therapy, Proc. Natl. Acad. Sci. U. S. A. 111 (2014) 17266–17271.

[221] A.J. Ziebarth, S. Nowsheen, A.D. Steg, et al., Endoglin (CD105) contributes to platinum resistance and is a target for tumor-specific therapy in epithelial ovarian cancer, Clin. Cancer Res. 19 (2013) 170–182.

[222] J. Zhang, B. Yuan, H. Zhang, et al., Human epithelial ovarian cancer cells expressing CD105, CD44 and CD106 surface markers exhibit increased invasive capacity and drug resistance, Oncol. Lett. 17 (2019) 5351–5360.

[223] J.A. Ross, I. Ansell, J.T. Hjelle, et al., Phenotypic mapping of human mesothelial cells., Adv. Perit. Dial. 14 (1998) 25–30.